



SUDAAR 552

STANFORD UNIVERSITY

Guidance and Control Laboratory

**THEORETICAL AND EXPERIMENTAL
INVESTIGATIONS OF SENSOR LOCATION
FOR OPTIMAL AEROELASTIC
SYSTEM STATE ESTIMATION**

DAA/AMES

by

Gang Liu

Guidance and Control Laboratory
Department of Aeronautics and Astronautics
STANFORD UNIVERSITY
Stanford, California 94305

This research was supported by
NASA Dryden Flight Research Center
Edwards, California 93523
NASA Grant NSG 4002

September 1985

(NASA-CR-177115) THEORETICAL AND
EXPERIMENTAL INVESTIGATIONS OF SENSOR
LOCATION FOR OPTIMAL AEROELASTIC SYSTEM
STATE ESTIMATION Final Report (Stanford
Univ.) 182 p

N86-29272

Unclas
CSCL 20K G3/39 43246

**THEORETICAL AND EXPERIMENTAL INVESTIGATIONS
OF SENSOR LOCATION FOR
OPTIMAL AEROELASTIC SYSTEM STATE ESTIMATION**

by
Gang Liu

**Guidance and Control Laboratory
Department of Aeronautics and Astronautics
STANFORD UNIVERSITY
Stanford, California 94305**

This research was supported by

**NASA Dryden Flight Research Center
Edwards, California 93523
NASA Grant NSG 4002**

September 1985

ABSTRACT

One of the major concerns in the design of an active control system is obtaining the information needed for effective feedback. This involves the combination of sensing and estimation. A sensor location index is defined as the weighted sum of the mean square estimation errors in which the sensor locations can be regarded as estimator design parameters. The design goal is to choose these locations to minimize the sensor location index. The gradient of the sensor location index with respect to each individual sensor location is formulated and a program using this gradient for systematic optimal sensor location search is developed. The choice of the number of sensors is a tradeoff between the estimation quality based upon the same performance index and the total costs of installing and maintaining extra sensors.

An experimental study for choosing the sensor location is conducted on an aeroelastic system. It is the physical realization of a two degree of freedom typical section wing. It consists of a NACA 0015 typical section wing with six accelerometers installed inside along the wing chord as the estimator measuring instruments, an existing wind tunnel section, and some other accompanying experimental devices. The system modeling which includes the unsteady aerodynamics model developed by Stephen Rock has been improved. The center of percussion of the rigid two degree of freedom typical section wing has been verified as a sensor location for which the system is unobservable. Experimental results verify the trend of the theoretical predictions of the sensor location index for different sensor locations at various wind speeds.

PRECEDING PAGE BLANK NOT FILMED

ACKNOWLEDGEMENTS

I wish to express my gratitude to my advisor, Professor Daniel B. DeBra, for his valuable guidance and support throughout the course of this research. I also wish to thank Professors Arthur E. Bryson, Jr. and J. David Powell for their review of this dissertation. My appreciation is extended to them for their time, attention and constructive comments.

I would like to thank the NASA Dryden Flight Research Center for their research support under Grant NSG 4002.

My deepest gratitude should go to my parents for giving me all the opportunities in life and the encouragement to seek higher education. Their unselfish love and support made it possible for me to attain this goal. However, it is such a regret that my father, who died of cirrhosis in January 1982, could not see the completion of my work. He had always been preoccupied with the hope of seeing the finished dissertation while on his sickbed. Whatever this work could accomplish should be attributed to my parents.

TABLE OF CONTENTS

Content	Page
ABSTRACT	iii
ACKNOWLEDGEMENTS	iv
TABLE OF CONTENTS	v
LIST OF FIGURES	ix
LIST OF TABLES	xii
LIST OF SYMBOLS	xiii
English Symbols	xiii
Greek Symbols	xvi
Mathematics Operators and Functions	xvi
Subscripts	xvii
Superscripts	xviii
Abbreviations	xviii
Special Symbols	xix
Computer Programs	xix
Chapter I. INTRODUCTION	1
A. BACKGROUND	1
B. THESIS OUTLINE	5
C. SUMMARY OF CONTRIBUTIONS	7
Chapter II. PROBLEM FORMULATION	9
A. INTRODUCTION	9
B. OBSERVABILITY OF DYNAMICAL SYSTEMS	11

C. KALMAN FILTER GAIN	16
1. Continuous System	18
2. Discrete System	23
D. EXPERIMENTAL SYSTEM OBSERVABILITY ANALYSIS	29
1. Differential Equation Investigation	29
2. Observability Matrix	34
3. Transfer Function and Modal Form	37
E. CRITERIA FOR CHOOSING THE BEST SENSOR	
LOCATION	38
1. Degree of Observability (DO)	40
2. Sensor Location Index (SLI)	42
3. Gradient Search Procedure	44
4. Comparison between the SLI and DO When $Q_w = 0$	47
5. Relative Merits of the SLI versus DO	51
F. DOUBLE SENSORS CASES	52
Chapter III. EXPERIMENTAL APPARATUS	54
A. INTRODUCTION	54
B. WIND TUNNEL	55
C. AIRFOIL	57
D. SUSPENSION SYSTEMS	61
1. Plunge Suspension	61
2. Pitch Suspension	64
E. ACTUATORS	66
1. Plunge Actuator	66
2. Pitch Actuator	66
F. SENSORS	70
1. Plunge Sensor	70
2. Pitch Sensor	70
3. Linear Acceleration Sensors	70
4. Airspeed Sensor	71

G. COMPUTER SYSTEMS	71
H. SYSTEM PARAMETERS	72
I. APPARATUS PERFORMANCE	75
1. Unbalanced Force Problem	75
2. Differential Modes Problem	75
Chapter IV. EXPERIMENTAL METHODS AND RESULTS	81
A. INTRODUCTION	81
B. MEASUREMENT OF SYSTEM PARAMETERS	81
C. ACCURACY OF SYSTEM MODELING	84
D. PARAMETER IDENTIFICATION	95
E. ESTIMATOR DESIGN	99
1. Choice of Q_w and R_v Matrices	99
2. Sensor Location Evaluation	100
F. DISCUSSION OF THE RESULTS	102
Chapter V. SUMMARY AND RECOMMENDATIONS	108
A. SUMMARY	108
B. RECOMMENDATIONS FOR FUTURE RESEARCH	110
Appendix A. MATHEMATICAL MODELING	111
A. EXTENDED HAMILTON PRINCIPLE	111
B. EQUATIONS OF MOTION	114
1. Two DOF Model	114
2. Three DOF Model	117
C. UNSTEADY AERODYNAMICS MODELING	119
1. Blockage Corrections	119
2. Lift Interference Effect	120
Appendix B. ACTUATOR AND SENSOR CALIBRATIONS	136
A. ACTUATORS	136
1. Static Response	136
2. Dynamic Response	138

B. SENSORS	141
1. Static Response	141
2. Dynamic Response	141
Appendix C. MEASUREMENT OF SYSTEM PARAMETERS . .	144
Appendix D. TABLE OF GRADIENTS	155
References	157

LIST OF FIGURES

Figure No.	Page
Fig. II-1	Uniform, Free-Free Beam Undergoing A Transverse Vibration 12
Fig. II-2	First Four Modes of the Transverse Vibration 15
Fig. II-3	Acceleration Measurement 30
Fig. II-4	Determinant Δ vs Different Single Sensor Locations \bar{x}_s . 31
Fig. II-5	Example 32
Fig. II-6a	Performance Index $\text{tr}(WP)$ vs Different Single Sensor Locations \bar{x}_s at Zero Wind Speed 36
Fig. II-6b	Determinant $\det(O_{ob}^T O_{ob})$ vs Different Single Sensor Locations \bar{x}_s at Zero Wind Speed 36
Fig. II-7	Pole-Zero Loci For Different Single Sensor Locations at Various Wind Speeds 39
Fig. II-8	Gradient Search Procedure for the Optimal Sensor Location 45
Fig. II-9	Sensor Location Index J_{SL} vs Different Single Sensor Locations \bar{x}_s 46
Fig. II-10	Sensor Location Index J_{SL} vs Different Single Sensor Locations \bar{x}_s for $Q_w = 0$, $V = 0$, $T_e = 1$ sec 48
Fig. II-11	Performance Index $\text{tr}(S/W)$ vs Different Single Sensor Locations \bar{x}_s for $T_e = 1$ sec 49
Fig. II-12	Performance Index $\det(S)$ vs Different Single Sensor Locations \bar{x}_s for $T_e = 1$ sec 50
Fig. II-13	Single Sensor and Double Sensors Cases 53
Fig. III-1	Typical Section Wing 55
Fig. III-2	Experimental Apparatus 56
Fig. III-3	Plan View of the Stanford Subsonic Wind Tunnel 57
Fig. III-4	Templates for the NACA 0015 Wing Profile 58

Fig. III-5	NACA 0015 Model Wing Section Dimensions and the Six Accelerometer Locations	60
Fig. III-6	Arrangement of Plunge Suspension Springs and the Possible Degree of Freedom of Motions	62
Fig. III-7	Folded Cantilever Spring	62
Fig. III-8	Exploded View of Pitch Suspension System	65
Fig. III-9	Linear Motor and LVDT with its Suspension	67
Fig. III-10	Torque Motor and Four-Bar Linkage	68
Fig. III-11	Operations of Four-Bar Linkage	69
Fig. III-12	MNC-series Module Function Diagram	72
Fig. III-13	Magnitude of Transfer Function of h/F	76
Fig. III-14	Magnitude of Transfer Function of α/F	76
Fig. III-15	Magnitude of Transfer Function of α/T	77
Fig. III-16	Magnitude of Transfer Function of h/T	77
Fig. III-17	Unbalanced Reaction Force in Plunge Direction due to the Applied Torque	78
Fig. III-18	Differential Plunge Motion and Pitch Motions	79
Fig. IV-1	Nyquist Plot of $G(\frac{s+z}{s+p})$ in $\frac{s}{p}$ Plane	86
Fig. IV-2	Typical Output of the Genrad 2515 Structural Analyzer	88
Fig. IV-3	Open Loop Root Locus with Various Wind Speeds	89
Fig. IV-4	Setup for the Real Time Comparison	90
Fig. IV-5a	Actual and Simulated Plunge Responses to A Linear Doublet Input at Wind Speed $U = 0$ m/sec	91
Fig. IV-5b	Overlapped Plot	91
Fig. IV-6a	Actual and Simulated Pitch Responses to A Linear Doublet Input at Wind Speed $U = 0$ m/sec	92
Fig. IV-6b	Overlapped Plot	92
Fig. IV-7a	Actual and Simulated Accelerometer #3 Responses to A Linear Doublet Input at Wind Speed $U = 0$ m/sec	93
Fig. IV-7b	Overlapped Plot	93

Fig. IV-8a	Actual and Simulated Pitch Responses to A Linear Doublet Input at Wind Speed $U = 27.17$ m/sec	94
Fig. IV-8b	Overlapped Plot	94
Fig. IV-9	Setup for the Sensor Location Evaluation	101
Fig. IV-10	Sensor Location Index vs Different Single Sensor Locations	103
Fig. IV-11	Estimation error vs Different Single Sensor Locations .	104
Fig. IV-12	Sensor Location Index vs Different Double Sensor Locations	105
Fig. IV-13	Sensor Location Index vs Different Single Sensor Locations	106
Fig. IV-14	Estimator Pole Locus vs Various Q_w/R_v Ratios . . .	107
Fig. A-1	Two Degree of Freedom Modeling: Plunge and Pitch . .	115
Fig. A-2	Three Degree of Freedom Modeling: Plunge, Pitch and Twist	118
Fig. A-3	Blockage Effects	119
Fig. A-4	Timman's Coordinate Systems	121
Fig. B-1	Experimental Configuration for Static Calibration of Actuators	137
Fig. B-2	Frequency Response of h/F	139
Fig. B-3	Frequency Response of α/T	140
Fig. B-4	LVDT Calibration Curve	142
Fig. B-5	Resolver Calibration Curve	143
Fig. C-1	Plan View of Wing Exaggerating Dimensional Imperfections	144
Fig. C-2	Linear Spring Constant Calibration Curve	148
Fig. C-3	Angular Spring Constant Calibration Curve	149
Fig. C-4	Calibration of \bar{x}_a	152

LIST OF TABLES

Table No.		Page
Table II-1	Numerical Values of $\frac{\partial J_{ob}}{\partial \bar{x}_s}$, J_{ob} vs \bar{x}_s	46
Table III-1	Definition of Parameters	73
Table IV-1	Definition of Functions	82
Table IV-2	Old and New Values	86
Table A-1	Definition of Coefficients, a_i	126
Table A-2	a_i at Various H/b	130
Table A-3	Dependence of Timman's $a_3(k, \lambda)$ on k and H/b . .	131
Table A-4	Definition of Coefficients, d_i and f_i	132
Table A-5	Definition of Coefficients, g_i	133
Table A-6	Derivative of Parameters	134

LIST OF SYMBOLS

English Symbols

a	distance in semichord the EA lies after the MC
a_i	parameters defined in Table A-1
$a(k)$	system parameter vector (Eq. 4.5)
A_0, A_1, A_i	amplitude constants (Eq. 2.9)
b	semichord (Eq. 2.11)
c	wing chord
C	damping coefficient (Eq. 2.50)
d	distance between the sensor and EA (Eq. 2.52)
d_i	parameters defined in Table A-4
$D(k)$	gradient vector (Eq. 4.4)
$e_{i\max}$	maximum errors that can be tolerated in the x_i directions
$e(k), e(t)$	n_s estimation error vector (Eqs. 2.15, 2.40)
EI	bending stiffness of the beam (Eq. 2.1)
f_i	parameters defined in Table A-4
F, F_d	$n_s \times n_s$ state distribution matrix (Eqs. 2.13, 2.30)
F_i	resultant externally applied force vectors (Eq. A-2)
F_v	input voltage to the linear motor (Eq. 2.11)
g_i	parameters defined in Table A-5
G	transfer function gain (Eq. A-44)
G, G_d	$n_s \times n_c$ control distribution matrix (Eqs. 2.13, 2.30)
h	plunge displacement (Eq. 2.11)
H	semiheight of the wind tunnel section
H, H_z	$n_{ob} \times n_s$ observation distribution matrix (Eqs. 2.13, 2.27)
$H_{z,d}$	$n_{ob} \times n_s$ derivative observation distribution matrix (Eq. 2.27)
I_{α}, I_{α_T}	total apparent moment of inertia about the EA (Eq. C-4)
$I_{\alpha 1}, I_{\alpha 2}$	defined in (Eqs. C-3, C-5)
I_{ij}	$n_{ob} \times n_s$ matrix with 1 in the ij -th position and 0 elsewhere
I_o	moment of inertia about the point O
J	weighted mean square estimation error performance index
$J(t)$	$n_s \times n_s$ information matrix (Eq. 2.65)
J_{SL}	sensor location index (Eq. 2.72)
J_u, J_u'	$n_{ob} \times n_s$ control feed through distribution matrix
k	$\omega b/U$, reduced frequency (Eq. A-43)
k'	$\sqrt{1 - k^2}$, (Eq. A-39)

k^*	$\tanh \pi b/2H$, (Eq. A-39)
K	moment of inertia ratio defined in (Eq. C-10)
K	complete elliptic integral of the first kind of k^*
K'	complete elliptic integral of the first kind of k'
$K(k), K(t)$	$n_s \times n_{ob}$ Kalman filter gain matrix (Eqs. 2.14, 2.39)
K_α, K_h	pitch and plunge spring rates (Eq. 2.11)
K_A	current amplification gain
K_c	spar coupling spring rate (Eq. A-30)
K_F, K_T	linear motor force and torque motor moment constants
K_s	spring rate (Eq. 3.1)
K_2	mass ratio (Eq. C-9)
l	length of the four bar linkage (Eq. 2.11)
l'	length of the wing spar
L	total length of the beam (Eq. 2.1)
$L(t)$	unsteady aerodynamic lift force (Eq. A-26)
m	mass
M	Mach number, U/c , where c is sound speed
$M(k)$	$n_s \times n_s$ estimation error covariance matrix before measurement
$\dot{M}(k)$	approximate second order derivative defined in (Eq. 4.4)
$M_\alpha(t)$	unsteady aerodynamic moment about the EA (Eq. A-27)
M_{Al}	mass of the Al spar
M_1	total apparent mass of the suspension system (Eq. C-2)
M_2	total apparent mass of the wing section
M_T	total apparent mass (Eq. 2.11)
n	normal direction (Eq. A-40)
n_s	no. of states (Eq. 2.13)
n_c	no. of controls (Eq. 2.13)
n_g	no. of process disturbances (Eq. 2.13)
n_{ob}	no. of observations (Eq. 2.13)
O_{ob}	observability matrix (Eq. 2.61)
p	pole location (Eq. A.44)
p_i	linear momentum (Eq. A-3)
$p(x, t)$	unsteady aerodynamic pressure distribution (Eq. A-42)
$P(k), P(t)$	$n_s \times n_s$ estimation error covariance matrix (Eqs. 2.40, 2.16)
$q_i(t)$	modal amplitudes (Eq. 2.3)
Q_{nc}, Q_c	generalized (non)conservative force vector (Eq. A-14)
$Q_T(s, \lambda)$	modified Theodorsen function by Timman (Eq. A-44)
Q_w, Q_d	power spectral density of $w(t)$ (Eqs. 2.13, 2.38)
r_α^2	radius of gyration about the EA squared (Eq. C-7)
r_i	position vectors (Eq. A-1)
r_o^2	radius of gyration about point O squared
R_i	resultant force vectors (Eq. A-1)

R_v, R_v', R_d	power spectral density of $v(t)$	(Eqs. 2.27, 2.34)
R_x	reaction force vector in the x -direction	
S_a	dynamic coupling coefficient	(Eq. C-14)
$S(k)$	sensitivity function	(Eqs. 4.6, 4.7)
t, τ, T	time	
T	$n_s \times n_s$ transformation matrix	(Eq. 2.63)
$T(\dot{r})$	kinetic energy	(Eq. A-12)
$T(s, \lambda)$	modified Küssner's T function	(Eq. A-45)
T_a	torque motor moment about the EA	(Eq. A-24)
T_c	control time period	
T_e	estimation time period	
T_s	sampling time period	(Eq. 2.38)
T_V	input voltage to the torque motor	(Eq. 2.11)
u	velocity component in the x -direction	
$u(k), u(t)$	n_c control vector	(Eqs. 2.13, 2.30)
U	airspeed	
\bar{U}	U/b	
$v(k), v(t)$	n_{ob} white observation noise vector	(Eqs. 2.13, 2.30)
$\bar{v}(t)$	defined in (Eq. A-40)	
V, V'	cross spectral density between $w(t)$ and $v(t)$ or $v'(t)$	
$V_d'(k)$	defined in (Eq. 2.36)	
$V_d(k+1)$	defined in (Eq. 2.37)	
V_E	transformed n_s -dimensional ellipsoid volume	(Eq. 2.69)
V_{input}	input voltage	
$V(r)$	potential energy	(Eq. A-13)
V_S	maximum spherical volume contained in the V_E	(Eq. 2.69)
$w(k), w(t)$	n_g white process disturbance vector	(Eqs. 2.13, 2.30)
W	symmetric positive-definite weighting matrix	
$W(s)$	Laplace transform of $w(t)$	(Eq. 2.62)
x	horizontal coordinate	(Eq. 2.1)
$x(k), x(t)$	n_s state vector	(Eqs. 2.13, 2.30)
x_a	the distance of the CM lies after the EA	(Eq. C-8)
x_s	distance between the sensor and MC	(Eq. 2.55)
y	vertical coordinate	
$\bar{y}(t)$	unsteady aerodynamic state	(Eq. A-48)
$y(x, t)$	transverse displacement at station x and time t	(Eq. 2.1)
z	zero location	(Eq. A.44)
z	$x + iy$	
z	linear acceleration measurement	(Eq. 2.52)
$z(k), z(t)$	n_{ob} observation vector	(Eqs. 2.13, 2.30)
Z	$X + iY$	
$Z(s)$	Laplace transform of $z(t)$	(Eq. 2.62)

Greek Symbols

α	pitch displacement (Eq. 2.11)
α_1, α_2	defined in (Eq. A-28)
β_i	defined in (Eq. 2.8)
Γ	$n_s \times n_g$ process disturbance distribution matrix (Eq. 2.13)
$\delta(t - \tau)$	delta function (Eq. 2.13)
Δ	determinant (Eq. 2.54)
Δ	difference between upper and lower surfaces (Eq. A-19)
ϵ_{sb}	solid blockage correction coefficient (Eq. A-37)
ϵ_{wb}	wake blockage correction coefficient (Eq. A-37)
ζ	$\epsilon + i\eta$ (Eq. A-39)
ζ_α, ζ_h	pitch and plunge damping ratios (Eq. 2.11)
λ	$\pi b/2H$ (Eq. A-44)
Λ	$n_s \times n_s$ Lagrangian multiplier matrix (Eq. 2.73)
Λ	$n_s \times n_s$ modal state distribution matrix (Eq. 2.63)
$\nu(k)$	innovation sequence (Eq. 4.2)
ν_i, ν_{\max}	eigenvalues (Eq. 2.69)
$\xi(t)$	n_s modal state vector (Eq. 2.63)
ρ	air density (Eq. C-13)
σ	mass density per unit length of the beam (Eq. 2.1)
$\phi_i(x)$	mode shapes (Eq. 2.3)
Φ	disturbance velocity potential
Φ_1	noncirculatory disturbance velocity potential (Eq. A-40)
Φ_2	circulatory disturbance velocity potential (Eq. A-41)
$\Phi(t_{k+1}, t_k)$	state transition matrix from time t_k to t_{k+1} (Eq. 2.38)
ω, ω_i	frequency and i -th modal frequency (Eqs. A-40, 2.8)
ω_α, ω_h	coupled pitch and plunge modal frequencies (Eq. 2.11)

Mathematical Operators and Functions

cn	Jacobian elliptic function
cos	cosine function
cosh	hyperbolic cosine function
det	determinant of a square matrix
$E \{ \dots \}$	expected value operator
i	$\sqrt{-1}$

\min_K	minimum value over all possible K
$N[\bar{x}, P]$	normal distribution with mean \bar{x} and covariance matrix P
s	Laplace variable
\sin	sine function
\sinh	hyperbolic sine function
tr	trace of a square matrix
δ	first variation operator
∂	partial derivative operator

Subscripts

a	sensitivity w.r.t. a parameter vector a
c	conservative, or control
d	discrete, or derivative
e	estimation
F	linear motor
g	disturbance
h	plunge mode
i	i th component
k	at time instant t_k
\max	maximum value
\min	minimum value
nc	nonconservative
new	new value
ob	observability, or observation
old	old value
s	sampling, or sensor, or state
ss	steady state value
T	Timman, or total, or torque motor
uc	uncorrected
v	voltage input
z	measurement
α	pitch mode
o	initial value
$+$	upper surface
$-$	lower surface

Superscripts

\cdot	differentiation w.r.t. time
\wedge	estimate
T	matrix transpose
-1	matrix inverse
\bar{x}	mean value, or a value nondimensionalized by semichord
0	optimal value

Abbreviations

A/D	analog to digital
CM	center of mass, or mass center
CP	center of percussion
D/A	digital to analog
DO	degree of observability
DOF	degree of freedom
EA	elastic axis
EMF	electromagnetic force
FFT	fast Fourier transform
LQ	linear quadratic
LQG	linear quadratic Gaussian
LVDT	linear variable differential transformer
MC	midchord
NACA	national advisory committee for aeronautics
NASA	national aeronautics and space administration
PSD	power spectral density
rms	root mean square
SLI	sensor location index
w.r.t	with respect to
2-D	two dimensional

Special Symbols

+ $1-\sigma$ error bar on experimental data plots

Computer Programs

DISC discrete optimal control system design program
LOPTSYS modified continuous optimal control system design program
OPTSYS continuous optimal control system design program

Chapter I

INTRODUCTION

A. BACKGROUND

Large structures have been considered for future space missions, such as communications, collection of solar energies, etc. Because of the inherent size and the necessarily low weight to area ratio, the influence of structural flexibility is becoming more significant. This is also true for the future energy efficient air transports which in addition need increased performance, comfort, and service time. To meet the requirement of larger configurations and more ambitious specifications on control system performance, e.g. controlling both the geometric shape and the orientation of the configuration (attitude control) [Refs. 1-2], as well as vibration suppression [Refs. 3-6], one is led to the use of modern multivariable control theory and the associated concepts of controllability and observability. However, the concepts of controllability and observability in modern control theory can only provide binary information, i.e. either a system is controllable (observable) or uncontrollable (unobservable) [7]. The more useful design questions which are naturally asked still remain unsolved:

- a) What types of actuators and sensors should be used?
- b) How to identify the minimum required number of them, and how does the increased number affect the overall performance?
- c) Where should they be placed?

Among all, placement exhibits a fundamental and largest degree of freedom

available to the designer even though it is usually not a very straightforward question to answer.

There are already several papers discussing these problems and some guidelines have been suggested [Refs. 8-14].

Juang and Rodriguez [8] start from the general linear quadratic (LQ) formulations and establish two criteria relating the actuator and sensor placement to the minimums of the optimal cost function and state estimation error. This is a simple approach but it doesn't take into account the time constraint of the control or estimation.

Likins, et al. [9] define a measure of controllability based on the minimum initial distance from the origin in a state space from which the system can be brought to the origin in time T_c , what they call "recovery region". This is a difficult problem itself which can only be solved approximately.

Hughes and Skelton [10] develop the modal controllability (observability) by measuring the controllability (observability) norm based on a linear matrix-second-order system formulation.

Kammer and Sesak [11] interpret the increasing insensitivity to parameter variations (robustness) versus actuator number analytically, it is analogous to that caused by the α -shifted performance index. This result adds to the designer's ability one more degree of freedom, especially in dealing with distributed systems. It also confirms that the performance tends to increase with increasing system complexity, i.e. with more actuators and sensors.

After reviewing Juang's and Likins' works and finding objections, Vander Velde and Carignan define the degree of controllability (observability) as a linear measure of the weighted "volume" of the hyperellipsoid in the transformed equicontrol (equimeasure) space [Refs. 12-14]. This definition will

be reviewed in Chapter II.

It is evident that they all try to find a standardized criterion that measures directly the degree of controllability (observability) for different actuator (sensor) locations. Most important, it must be a quantitative measure that can be easily computed and have a direct physical interpretation so that the control system designer can rank the desirability of various candidate actuator (sensor) distributions in a meaningful way.

In this research, our major concern is to find a guideline in this respect for sensing and state estimation. So we will hereafter restrict ourselves to the sensor part in the above questions. While the duality between estimator and controller design is well known and established [Refs. 15-16], this research goal can thus easily be extended to the controller part.

First, a so called sensor location index (J_{SL}) will be proposed. It is defined as a weighted sum of the mean square estimation errors, i.e. $J_{SL} = \text{tr}(WP)$, where W is a symmetric positive-definite weighting matrix. It happens to be similar to Juang's idea, except for the weighted sum formulation. The choice of W is similar to Vander Velde's choice of the transformation to an equimeasure space, specifically, it is the inverse square of his transformation matrix.

Using existing software support, it is easy to compute the J_{SL} in a steady state manner. Since our goal is to look for the optimal sensor location directly, an optimization technique using the gradient search scheme is applied for this purpose. The program is designed to report the figure of merit for different sensor locations and increasing sensor number, thus offers the designer a handy reference to make his judgements.

An experimental study to evaluate the sensor number and their locations is conducted on an aeroelastic system. It is the physical realization of a two degree

of freedom (DOF) typical section wing [Refs. 17-18]. It consists of a NACA 0015 typical section wing with six accelerometers installed inside along the wing chord as the estimator measuring instruments. The evaluation process is done through the Kalman filtering technique for state estimation and sensor location index computation. However, effective implementations of Kalman filtering depend heavily upon the accuracy of the unsteady aerodynamics theory in predicting the loads associated with the general motions of the airlifting surfaces. Fortunately, this unsteady aerodynamics theory has already been investigated thoroughly.

A complete solution for the unsteady aerodynamic loads of the typical section wing, including a trailing-edge flap, undergoing a simple harmonic motion was first presented by Theodorsen [19] in 1935 for the conditions of incompressible, inviscid, two-dimensional airflows.

In 1951, Timman [20] solved the same problem except under the constraint of a two-dimensional wind tunnel.

In 1977, Edwards [Refs. 21-22] extended Theodorsen's results to include arbitrary airfoil motions by recognizing a derivation of the generalized Theodorsen function in the work of Von Karman and Sears [Refs. 23-24].

In 1978, Rock [25] combined Timman's results with the work of Edwards' to develop an aeroelastic model for a 2 DOF typical section wing undergoing arbitrary motions in a small subsonic wind tunnel. He also verified this analytic model by experimental investigations.

Afterwards, in 1981, Stoltz [26] extended Rock's work by adding a trailing-edge flap to the typical section wing. Using this as a control surface, he was able to design an active aeroelastic control law capable of stabilizing the experimental wing-flap system up to a dynamic pressure equal to twice the open

loop flutter value.

In our experimental studies, Rock's unsteady aerodynamics modeling is used for our new airfoil model and it is presented in Appendix A.

B. THESIS OUTLINE

In Chapter II, a continuous free-free beam example is first given to explain the physical meaning of system observability. Then the optimal estimator design problem is reformulated for correlated process disturbance and measurement noise. The derivation is based on minimizing a weighted sum of the mean square estimation errors as the performance index [15]. It turns out that it is not trivial especially for the discrete case. The OPTSYS program [27] is modified to the LOPTSYS to accept a more general input form including a rate measurement. It solves for the continuous steady state estimator gain with correlated process disturbance and measurement noise. A similar work is done independently by Walker [64] and it is included in the COPT program. For the discrete case, a FORTRAN program is developed to carry out the estimator gain iteration until it approaches the steady state value. This program is validated by comparing the results of some examples with uncorrelated disturbance and noise run on the program DISC [28].

The experimental system has an unobservable sensor location for the accelerometer. It is verified to be the center of percussion (CP) [29]. This same physical behavior is used independently by Chiang in his mini-manipulator design [30]. Several different investigations of the experimental system observability by examining the observability matrix, the transfer function pole-zero loci and the modal disturbance and measurement distribution matrices are performed and some conclusions are given.

Finally, a gradient search scheme is developed to find the optimal sensor location based on the sensor location index which is similar to the performance index for the estimator design. This is a general scheme which is capable of solving multisensor problems. A computer program is developed to do the search and a result for a single sensor case is given. The sensor location index (SLI) is then compared with the degree of observability (DO) suggested by Vander Velde. A double sensor example is given to conclude this chapter.

Chapter III describes our experimental apparatus. There is not too much difference from that used by Rock [25] or Stoltz [26], except a new and thicker wing model is built to accommodate those accelerometers used as measuring instruments. A digital computer is used in this study for data collection and analysis. Some software is developed to facilitate the laboratory operation.

Chapter IV describes the experimental methods and results. The approximation to Timman's modified Theodorsen function suggested by Rock is reexamined. With the external sensors used and the doublet excitation he had found it impossible to verify experimentally this part of the model. However, it is a well-posed parameter identification problem [Refs. 31-32]. An on-line parameter identification scheme through Kalman filtering proposed by Mishne [33] is modified and used for this purpose. Simulations are carried out and found to be successful. But actual tests fail because of the existence of the process disturbance and the measurement noise.

A more accurate 5th order system model which includes those experimentally measured damping terms in the F matrix and takes into account the unbalanced force due to the applied torque in the G matrix. The dynamic coupling [Refs. 34-35] between the plunge and pitch modes through the actual wing section mass center offset from the elastic axis is used in the F matrix rather than using the distance between the entire plunge suspension system mass

center and the elastic axis. The accuracy of the system model is checked by examining the theoretical and the experimental root locus versus varying wind speeds. The worst case for stable behaviors is about 1% error in the pitch mode frequency. This same accuracy is also observed by comparing the computer simulated system responses to the linear motor doublet input with those of the actual system responses.

The quality of estimation varies with the location and number of sensors. It can be indicated by the sensor location index we proposed. The difficulty in evaluating it as a function of the sensor location is presented in the estimator design section along with the approaches we use to get around it. The experimental test results are given and they prove the trends predicted by the theory.

Chapter V gives a summary and recommendations for the future research.

Appendix A includes the derivation of the system modeling and the unsteady aerodynamics model derived by Rock. Instrument calibrations and system parameter measurements are detailed in Appendices B and C.

C. SUMMARY OF CONTRIBUTIONS

- 1) The computer program OPTSYS is modified to the LOPTSYS to accept a more general input form including a rate measurement. The correlation between system disturbance and measurement noise is taken into account.
- 2) An iterative scheme for calculating the discrete Kalman filter gain is derived to deal with the correlation between system disturbance and measurement noise for discrete systems.
- 3) Experimental system observability is examined from several different approaches and some conclusions are given. System unobservable

sensor location is verified analytically to be the center of percussion of the two DOF typical section wing at zero wind speed.

- 4) A tractable sensor location index is defined so that the optimization technique can be applied. A first order gradient search algorithm is developed and implemented. It is a general scheme which can be used for solving multisensor cases. The program doing the optimal sensor location search can report the figure of merit of the sensor location index for different sensor locations and increasing sensor number.
- 5) An experimental apparatus is set up for feasibility studies. It includes a new and thicker airfoil with six accelerometers installed inside along the wing chord as measuring instruments.
- 6) An on-line parameter identification through Kalman filtering is modified and used for aerodynamic parameter identification.

Chapter II

PROBLEM FORMULATION

A. INTRODUCTION

State variable feedback control requires all the system states to be measured. However, the more frequent situation is that only certain linear combinations of the state can be obtained.

By using a linear model of the system and the statistical models which characterize the system disturbance and measurement noise, Kalman developed a filter with which to reconstruct the missing states from any set of noisy measurements [Refs. 36-37].

Although a Kalman filter describes how to process the measurement data to achieve the optimal system state reconstruction, it doesn't [38, p. 3]:

- 1) solve the problem of designing in the presence of parameter uncertainties,
- 2) provide a method for dealing with computational errors,
- 3) solve the problem of establishing an optimal measurement schedule.

The first problem is due to the presumption of a perfect mathematical model which requires the system be known exactly in order to formulate the optimal Kalman filter. Since this is often unrealistic and may lead to filter divergence, many authors have derived results to overcome this problem [Refs. 39-42]. The second difficulty is caused by the quantization limitation inherent in the computer implementation, especially in dealing with ill-conditioned problems.

Alternate recursive relationships have been developed, such as discrete square root filtering [Refs. 43-44], to cope with this difficulty. The third question is because there are various choices of the sensor type, number and location.

The sensor type is usually limited by its utility, cost, availability, reliability, and other factors [45]; the sensor number is a tradeoff between the estimation quality and the cost of installing and maintaining, the weight as well as power consumption for extra sensors. All of them are highly cost dependent. However, a good choice of sensor location may increase the overall performance without a change in cost. Of course, the sensor location may still be constrained by its size and ease of access.

While the sensor type is usually determined in the early design stages, the sensor placement is a degree of design freedom frequently not fully exercised, especially in large distributed systems. A standardized criterion could be very helpful to a designer in choosing the sensor number and their locations optimally. Some authors have already suggested approaches [Refs. 8-11], and the most intuitive result is given by Vander Velde [Refs. 12-14]. In this chapter, a new approach based on the steady state solution of the optimal estimation problem is presented to study the sensor location problem. The final goal is to develop a process that can be used to look for the best sensor location directly and report its figure of merit for increasing sensor number to help the designer's judgement in making his decisions.

A experimental study for choosing the sensor number and their locations is conducted on a simple two DOF aeroelastic system. A detailed description of this experimental apparatus is given in Chapter III. Basically, it is a physical realization of an ideal two DOF typical section wing [Refs. 17-18]. The modeling of the unsteady aerodynamics of this system was already developed and experimentally verified by Rock in 1978 [25]. So there is obviously an

advantage in using a similar system to save some time and effort. Besides, this is a simple physical system which is still capable of describing such complex aeroelastic phenomena as divergence and bending-torsion flutter thus making it a realistic application area of our research objective. Also, many experimental studies have used this typical section wing, it facilitates the comparison of new and old experimental results [25, p. 2].

In this chapter, an example is first given to illustrate the effects of sensor types and locations upon the system observability. Secondly, the Kalman filter gains for both the continuous and discrete cases will be reformulated under the condition of correlated process disturbance and measurement noise in order to minimize the performance index chosen to be the weighted sum of the mean square estimation errors. Thirdly, a study of the observability of our experimental system is investigated through several different approaches. The purpose is to find a direct connection that can be used to help determine the sensor location and number. Then a gradient search scheme is developed to achieve this goal. A comparison between Vander Velde's criterion and ours is conducted assuming there is no process disturbance and using finite estimation time. Finally, a double sensor example is given to conclude this chapter.

B. OBSERVABILITY OF DYNAMICAL SYSTEMS

To many readers, the concept of observability of dynamical systems may seem to be a weak abstract idea rather than one with strong physical feeling. A real example showing its physical meaning should be useful for further investigations.

Let us consider a uniform, free-free beam undergoing a transverse vibration as shown in Fig. II-1 without taking into account the effect of gravity. Neglecting the shear distortion and rotary inertia, the equation of motion of the beam is governed by the Bernoulli-Euler model [46, p. 135]:

$$\frac{\partial^4 y(x,t)}{\partial x^4} + \frac{\sigma}{EI} \frac{\partial^2 y(x,t)}{\partial t^2} = 0, \quad (2.1)$$

where $y(x,t)$ is the transverse displacement at station x and time t , and EI , σ , and L are the beam bending stiffness, mass density per unit length, and beam total length respectively.

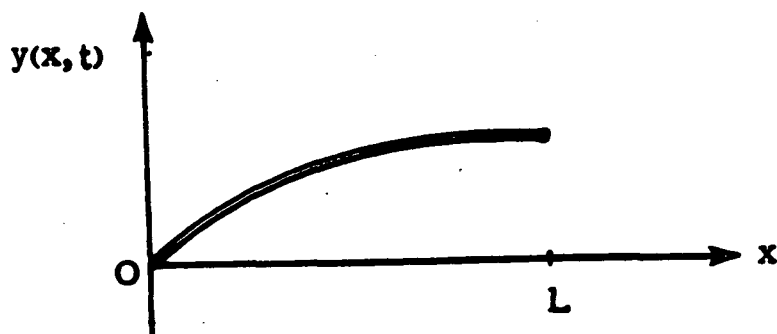


Fig. II-1 Uniform, Free-Free Beam Undergoing A Transverse Vibration

The natural boundary conditions are [46, pp. 163-166]

$$\frac{\partial^2 y}{\partial x^2}(0,t) = \frac{\partial^2 y}{\partial x^2}(L,t) = 0, \quad (2.2a)$$

$$\frac{\partial^3 y}{\partial x^3}(0,t) = \frac{\partial^3 y}{\partial x^3}(L,t) = 0. \quad (2.2b)$$

Since the meaning of observability is understood most clearly in the modal coordinate system, the displacement is thus expressed as

$$y(x,t) \equiv \sum_{i=0}^{\infty} \phi_i(x) q_i(t), \quad (2.3)$$

where $\phi_i(x)$ are the mode shapes and $q_i(t)$ are the modal amplitudes [1, p. 36].

This separation of variables leads to a solution by substituting Eq. (2.3) into Eq. (2.1), and we obtain

$$\frac{d^4 \phi_i}{dx^4} q_i + \frac{\sigma}{EI} \phi_i \frac{d^2 q_i}{dt^2} = 0, \quad (2.4)$$

and

$$\frac{EI}{\sigma} \frac{1}{\phi_i} \frac{d^4 \phi_i}{dx^4} = - \frac{1}{q_i} \frac{d^2 q_i}{dt^2} = \omega_i^2. \quad (2.5)$$

So the differential equations to be satisfied become

$$\frac{d^4 \phi_i}{dx^4} - \beta_i^4 \phi_i = 0, \quad (2.6)$$

and

$$\frac{d^2 q_i}{dt^2} + \omega_i^2 q_i = 0, \quad (2.7)$$

where

$$\beta_i^4 = \omega_i^2 \frac{\sigma}{EI}. \quad (2.8)$$

After enforcing the boundary conditions, Eq. (2.2), we obtain

$$\phi_0(x) = A_0, \quad \beta_0 = 0, \quad (2.9a)$$

$$\phi_1(x) = A_1(x - \frac{L}{2}), \quad \beta_1 = 0, \quad (2.9b)$$

and

$$\begin{aligned} \phi_i(x) = A_i [& (\cos\beta_i L - \cosh\beta_i L)(\sin\beta_i x + \sinh\beta_i x) \\ & - (\sin\beta_i L - \sinh\beta_i L)(\cos\beta_i x + \cosh\beta_i x)], \end{aligned} \quad (2.9c)$$

where β_i satisfies

$$\cos\beta_i L \cosh\beta_i L = 1, \quad i = 2, 3, \dots \quad (2.10)$$

The first four modes are plotted in Fig. II-2. The two rigid body modes correspond to the rigid body translation and rotation respectively. Since there is no node in the rigid body translation mode, a displacement sensor can always observe this mode. However, if we place a displacement sensor at those nodes of the other modes, i.e. at points B, D, E, G, I, the corresponding mode will not be observed at those particular sensor locations. This can also be seen from the exact pole-zero cancellations in their transfer functions (see discussions in Section D-3). If an orientation sensor is used and placed at those locations where the mode shapes have zero slopes, i.e. at points C, F, and H,

the corresponding mode will be missing from its measurements, that is, the orientation sensor can not detect the mode at a point of zero slope [47, p. 9]. This should provide a clearer picture of the dependence of observability on sensor types and locations.

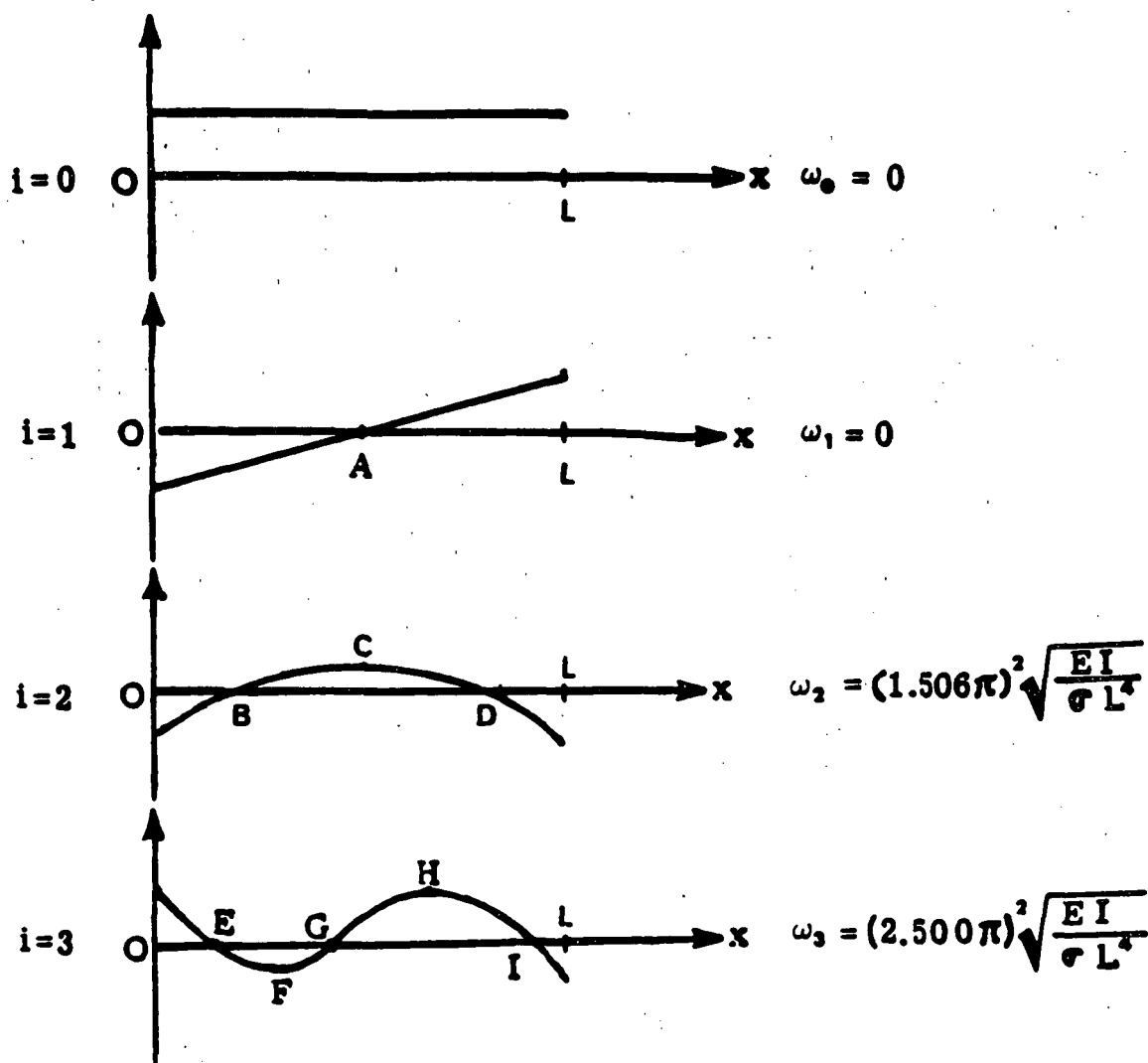


Fig. II-2 First Four Modes of the Transverse Vibration

C. KALMAN FILTER GAIN

The system equations of motion of our experimental apparatus are derived in Appendix A, see Fig. A-1. They are presented here for ease of reference.

- Equations of Motion without considering Aerodynamics:

$$\begin{bmatrix} \dot{\bar{h}} \\ \ddot{\bar{h}} \\ \dot{\alpha} \\ \ddot{\alpha} \end{bmatrix} = \begin{bmatrix} 0 & 1 & 0 & 0 \\ -\frac{\omega_h^2}{K} & -\frac{2\zeta_h \omega_h}{K} & \frac{K_2 \bar{\alpha} \omega_\alpha^2}{K} & \frac{2\zeta_\alpha \omega_\alpha K_2 \bar{\alpha}}{K} \\ 0 & 0 & 0 & 1 \\ \frac{\bar{\alpha} \omega_h^2}{\bar{\alpha}^2 K} & \frac{2\zeta_h \omega_h \bar{\alpha}}{\bar{\alpha}^2 K} & -\frac{\omega_\alpha^2}{K} & -\frac{2\zeta_\alpha \omega_\alpha}{K} \end{bmatrix} \begin{bmatrix} \bar{h} \\ \dot{\bar{h}} \\ \alpha \\ \dot{\alpha} \end{bmatrix} \\
 + \begin{bmatrix} 0 & 0 \\ \frac{K_F}{M_T K b} & -\left(\frac{1}{M_T \bar{l} b} + \frac{K_2 \bar{\alpha} b}{I_{\alpha r}}\right) \frac{K_T}{K b} \\ 0 & 0 \\ -\frac{K_F \bar{\alpha}}{M_T \bar{\alpha}^2 K b} & \left(\frac{1}{I_\alpha} + \frac{\bar{\alpha}}{M_T \bar{l} \bar{\alpha}^2 b^2}\right) \frac{K_T}{K} \end{bmatrix} \begin{bmatrix} F_V \\ T_V \end{bmatrix}$$

(2.11)

• Equations of Motion considering Aerodynamics:

$$\begin{bmatrix} \dot{\bar{h}} \\ \ddot{\bar{h}} \\ \dot{\alpha} \\ \ddot{\alpha} \\ \dot{\bar{y}} \end{bmatrix} = \begin{bmatrix} 0 & 1 & 0 & 0 & 0 \\ -g_1 & -g_2 & -g_3 & -g_4 & -g_5 \\ 0 & 0 & 0 & 1 & 0 \\ -g_6 & -g_7 & -g_8 & -g_9 & -g_{10} \\ 0 & -g_{11} & -g_{12} & -g_{13} & -g_{14} \end{bmatrix} \begin{bmatrix} \bar{h} \\ \dot{\bar{h}} \\ \alpha \\ \dot{\alpha} \\ \bar{y} \end{bmatrix} + \begin{bmatrix} 0 & 0 \\ +g_{19} & +g_{20} \\ 0 & 0 \\ +g_{21} & +g_{22} \\ 0 & 0 \end{bmatrix} \begin{bmatrix} F_V \\ T_V \end{bmatrix}$$

(2.12)

where

\bar{h} , $\dot{\bar{h}}$, $\ddot{\bar{h}}$ are the normalized plunge displacement and its time derivatives,

α , $\dot{\alpha}$, $\ddot{\alpha}$ are the pitch displacement and its time derivatives,

F_V , T_V are the input voltages to the linear and angular motors respectively.

All the coefficients and constants are defined in Appendices A and C.

C-1 Continuous System

Most of the mathematical representation of dynamic systems including the ones above can be described by the following linear, time-invariant, state differential equations:

$$\dot{x}(t) = Fx(t) + Gu(t) + \Gamma w(t), \quad (2.13a)$$

$$z(t) = Hx(t) + J_u u(t) + v(t), \quad (2.13b)$$

where

$x(t)$: $n_s \times 1$ state vector, with

$$E \{ x(t_0) \} = \bar{x}_0, \quad E \{ [x(t_0) - \bar{x}_0][x(t_0) - \bar{x}_0]^T \} = P_0,$$

$u(t)$: $n_c \times 1$ control vector,

$z(t)$: $n_{ob} \times 1$ observation vector,

$w(t)$: $n_g \times 1$ white process disturbance vector, with

$$E \{ w(t) \} = 0, \quad E \{ w(t)w^T(\tau) \} = Q_w \delta(t - \tau),$$

or it can be simply written as $w(t)$: $N[0, Q_w]$,

where Q_w is the power spectral density of $w(t)$,

$v(t)$: $n_{ob} \times 1$ white measurement noise vector, with

$$E \{ v(t) \} = 0, \quad E \{ v(t)v^T(\tau) \} = R_v \delta(t - \tau),$$

or it can be simply written as $v(t)$: $N[0, R_v]$,

where R_v is the power spectral density of $v(t)$,

t : $t \geq t_0$ time.

Furthermore, it is assumed that $w(t)$ and $v(t)$ are correlated, i.e. $E \{ w(t)v^T(\tau) \} = V\delta(t-\tau)$, where V is the cross spectral density of $w(t)$ and $v(t)$ [48], while the initial state $x(t_0)$ is uncorrelated with $w(t)$ and $v(t)$; $u(t)$ is a given known input to the system.

Suppose that a full-order estimator of the form [15, p. 351]

$$\dot{\hat{x}}(t) = F\hat{x}(t) + Gu(t) + K(t)[z(t) - H\hat{x}(t) - J_u u(t)] \quad (2.14)$$

is used to estimate the system state, and the estimation error is given by

$$e(t) = \hat{x}(t) - x(t). \quad (2.15)$$

The estimator can be designed optimally by finding the estimator gain matrix $K(\tau)$, $t_0 \leq \tau \leq t$, and the initial condition $\hat{x}(t_0)$, so as to minimize the weighted sum of the mean square estimation errors

$$J^o = \min_{K(t)} E \{ e^T(t) W e(t) \} = \min_{K(t)} \text{tr} [W P(t)], \quad (2.16)$$

where W is a symmetric positive-definite weighting matrix, and $P(t) = E \{ e(t)e^T(t) \}$ is the estimation error covariance matrix.

First subtracting Eq. (2.13a) from Eq. (2.14) and using Eq. (2.13b), we obtain

$$\dot{e}(t) = [F - K(t)H]e(t) + K(t)v(t) - \Gamma u(t), \quad (2.17a)$$

$$e(t_0) = e_0 = \hat{x}(t_0) - x(t_0). \quad (2.17b)$$

It follows from the above equation that $P(t)$ satisfies the following differential equation

$$\begin{aligned} \dot{P}(t) = & [F - K(t)H]P(t) + P(t)[F - K(t)H]^T \\ & + K(t)R_v K^T(t) + \Gamma Q_w \Gamma^T - \Gamma V K^T(t) - K(t)V^T \Gamma^T, \end{aligned} \quad (2.18a)$$

$$P(t_0) = P_0. \quad (2.18b)$$

Substituting Eq. (2.18) into Eq. (2.16), and using the gradient table [49] in Appendix D to take derivatives, we obtain

$$\begin{aligned} J = \text{tr} \left\{ W \left[\int_{t_0}^t \left\{ [F - K(\tau)H]P(\tau) + P(\tau)[F - K(\tau)H]^T \right. \right. \right. \\ \left. \left. \left. + K(\tau)R_v K^T(\tau) + \Gamma Q_w \Gamma^T - \Gamma V K^T(\tau) - K(\tau)V^T \Gamma^T \right\} d\tau + P_0 \right] \right\}, \end{aligned} \quad (2.19)$$

$$\frac{\partial J}{\partial K} = W \left[\int_{t_0}^t \{ -2P(\tau)H^T + 2K(\tau)R_v - 2\Gamma V \} d\tau \right], \quad (2.20)$$

$$\frac{\partial^2 J}{\partial K^2} = 2W \int_{t_0}^t R_v d\tau \geq 0. \quad (2.21)$$

In order to minimize J with respect to K , $\frac{\partial J}{\partial K}$ must vanish, that is,

$$-2P(\tau)H^T + 2K(\tau)R_v - 2\Gamma V \equiv 0, \quad t \geq \tau \geq t_0, \quad (2.22)$$

which leads to

$$K^o(t) = [P(t)H^T + \Gamma V]R_v^{-1}, \quad t \geq t_0. \quad (2.23)$$

It can be seen that $K^o(t)$ is independent of the choice of the weighting matrix W .

Using the optimal gain matrix of Eq. (2.23) in Eq. (2.18), $P(t)$ now becomes the solution of the matrix Riccati equation

$$\begin{aligned} \dot{P}(t) = & [F - \Gamma V R_v^{-1} H] P(t) + P(t) [F - \Gamma V R_v^{-1} H]^T \\ & - P(t) H^T R_v^{-1} H P(t) + \Gamma Q_w \Gamma^T \\ & - \Gamma V R_v^{-1} V^T \Gamma^T, \quad t \geq t_0, \end{aligned} \quad (2.24a)$$

$$P(t_0) = P_0. \quad (2.24b)$$

Since Eq. (2.16) can be rewritten as [15, p. 342]

$$\begin{aligned} E \{ e^T(t) W e(t) \} = & \bar{e}^T(t) W \bar{e}(t) \\ + E \{ [e(t) - \bar{e}(t)]^T W [e(t) - \bar{e}(t)] \}, \end{aligned} \quad (2.25a)$$

where

$$\bar{e}(t) = E \{ e(t) \}. \quad (2.25b)$$

It is a sum of two positive quadratic terms, the first term of which is obviously minimal when $\bar{e}(t) = 0$. This can be achieved by letting $\bar{e}(t_0) = 0$, because $\bar{e}(t)$ obeys the homogeneous differential equation

$$\dot{\bar{e}}(t) = [F - K(t)H] \bar{e}(t), \quad (2.26)$$

so the initial condition of the estimator can be chosen as $\hat{x}(t_0) = \bar{x}_0$.

Since the system is time invariant, i.e. $F, G, \Gamma, H, J_w, Q_w, R_v, V$ are all constant matrices, it can be proved that the estimating process will reach a steady state as $t \rightarrow \infty$ [16, p. 366].

The OPTSYS computer program developed by Hall and Bryson [27] uses the eigenvector decomposition technique to solve for the steady state estimator gain and root mean square (rms) estimation error. Since the use of accelerome-

ters as measuring devices is common in most control applications, OPTSYS has been modified by the author to the LOPTSYS to accept the more general input form

$$\dot{x}(t) = Fx(t) + Gu(t) + \Gamma w(t), \quad (2.27a)$$

$$z(t) = H_{zd}\dot{x}(t) + H_z x(t) + J'_u u(t) + J'_w w(t) + v'(t), \quad (2.27b)$$

where

$$\begin{aligned} w(t): N[0, Q_w], \quad v'(t): N[0, R_v], \\ E\{w(t)v'^T(\tau)\} = 0. \end{aligned} \quad (2.27c)$$

Substituting Eq. (2.27a) into Eq. (2.27b), it can be shown that [Refs. 50, pp. 2-3, and 51, p. 73, and 52]

$$\begin{aligned} z(t) = [H_{zd}F + H_z]x(t) + [H_{zd}G + J'_u]u(t) \\ + [H_{zd}\Gamma + J'_w]w(t) + v'(t), \end{aligned} \quad (2.28)$$

so comparing with Eq. (2.13b), we have

$$\begin{aligned} H &= H_{zd}F + H_z, \\ J_u &= H_{zd}G + J'_u, \\ J_w &= H_{zd}\Gamma + J'_w, \\ v(t) &= [H_{zd}\Gamma + J'_w]w(t) + v'(t), \\ R_v &= [H_{zd}\Gamma + J'_w]Q_w[H_{zd}\Gamma + J'_w]^T + R_v', \\ V &= Q_w[H_{zd}\Gamma + J'_w]^T. \end{aligned} \quad (2.29)$$

It is important to know that the derivative term introduces a direct feed through of the process disturbance into the measurement noise and it is highly sensor location dependent.

C-2 Discrete System

In this research the evaluation of estimation quality for different sensor numbers and locations is carried out on a digital computer. So the previous development has to be extended to the discrete case. The discrete estimator gain found in this section will be used for our discrete estimator implementation.

First Eq. (2.28) is rewritten as

$$z(t) = Hx(t) + J_u u(t) + J_w w(t) + v'(t). \quad (2.30)$$

Instead of modeling $w(t)$ and $v'(t)$ as white noises, we must think of them as colored noises with variances Q_w and $R_{v'}$, and correlation times T_w and $T_{v'}$, respectively. That is,

$$T_w \dot{w}(t) + w(t) = \eta_w(t), \quad (2.31a)$$

$$T_{v'} \dot{v}'(t) + v'(t) = \eta_{v'}(t), \quad (2.31b)$$

where $\eta_w(t)$ and $\eta_{v'}(t)$ are white noise processes with power spectral densities $2T_w Q_w$ and $2T_{v'} R_{v'}$, respectively.

Let $x_a \equiv \begin{bmatrix} x^T & w^T & v'^T & T \end{bmatrix}^T$ and $\eta \equiv \begin{bmatrix} \eta_w^T & \eta_{v'}^T \end{bmatrix}^T$, Eqs. (2.27a), (2.30) and (2.31) become

$$\dot{x}_a(t) = F_a x_a(t) + G u(t) + \Gamma_a \eta(t), \quad (2.32a)$$

$$z(t) = H_a x_a(t) + J_u u(t), \quad (2.32b)$$

where

$$F_a = \begin{bmatrix} F & \Gamma & 0 \\ 0 & -\frac{1}{T_w} & 0 \\ 0 & 0 & -\frac{1}{T_v} \end{bmatrix}, \quad (2.33a)$$

$$\Gamma_a = \begin{bmatrix} 0 & 0 \\ \frac{1}{T_w} & 0 \\ 0 & \frac{1}{T_v} \end{bmatrix}, \quad (2.33b)$$

$$H_a = [H \ J_w \ I], \quad (2.33c)$$

$$\eta = N[0, Q], \quad Q = \text{diag} [2T_w Q_w, 2T_v R_v], \quad (2.33d)$$

which is a system with no white noise measurement.

Thus the discrete system is of the form [Refs. 53-55]

$$x_a(k+1) = F_a x_a(k) + G_a u(k) + \eta_a(k), \quad (2.34a)$$

$$z(k) = H_a x_a(k) + J_u u(k). \quad (2.34b)$$

If we use a zero-order hold for the control, that is,

$$u(t) = u(t_k), \quad t_k \leq t < t_{k+1}, \quad k = 0, 1, 2, \dots, \quad (2.35)$$

and assume that the observation is made at the controlling instant t_k , then

$$x_a(t_{k+1}) = \Phi(t_{k+1}, t_k)x_a(t_k) + \left[\int_{t_k}^{t_{k+1}} \Phi(t_{k+1}, \tau) G d\tau \right] u(t_k) + \eta(t_k), \quad (2.36a)$$

$$z(t_k) = H_a x_a(t_k) + J_u u(t_k). \quad (2.36b)$$

where $\Phi(t_{k+1}, t_k)$ is the state transition matrix from time t_k to t_{k+1} .

Comparing Eq. (2.34) with Eq. (2.36) we obtain:

$$\begin{aligned} F_d &= \Phi(t_{k+1}, t_k), \\ G_d &= \int_{t_k}^{t_{k+1}} \Phi(t_{k+1}, \tau) G d\tau, \\ \eta_d(k) &= \eta(t_k) = \int_{t_k}^{t_{k+1}} \Phi(t_{k+1}, \tau) \Gamma_a \eta(\tau) d\tau, \end{aligned} \quad (2.37a)$$

and

$$\begin{aligned} E \{ x_a(k_0) \} &= \bar{x}_{a_0}, \quad E \{ [x_a(k_0) - \bar{x}_{a_0}] [x_a(k_0) - \bar{x}_{a_0}]^T \} = M_0, \\ E \{ \eta_d(k) \} &= 0, \quad Q_d = E \{ \eta_d(k) \eta_d^T(k) \} \\ &= \int_{t_k}^{t_{k+1}} \Phi(t_{k+1}, \tau) \Gamma_a Q \Gamma_a^T \Phi^T(t_{k+1}, \tau) d\tau. \end{aligned} \quad (2.37b)$$

In the usual case in which the sampling instants are equally spaced, i.e. $t_{k+1} - t_k = T_s$, while the system is time-invariant, then

$$F_d = \Phi(t_{k+1}-t_k) = \Phi(T_s) = e^{F_s T_s},$$

$$G_d = \left[\int_0^{T_s} e^{F_s^T \tau} d\tau \right] G,$$

$$Q_d = \int_0^{T_s} e^{F_s^T \tau} \Gamma_s Q \Gamma_s^T e^{F_s \tau} d\tau. \quad (2.38)$$

Similar to the continuous case, we can design an optimal discrete estimator as [15, p. 550]

$$\begin{aligned} \hat{x}_a(k+1) = & \bar{x}_a(k+1) + K(k+1) \times \\ & [z(k+1) - H_a \bar{x}_a(k+1) - J_a u(k+1)], \end{aligned} \quad (2.39a)$$

where

$$\bar{x}_a(k+1) = F_d \hat{x}_a(k) + G_d u(k), \quad (2.39b)$$

by finding the gain matrix $K(j)$, $k_0 \leq j \leq k$, and the initial state $\hat{x}_a(k_0)$ in order to minimize the weighted sum of the mean square estimation errors

$$J^o = \min_{K(k)} E \{ e^T(k) W e(k) \} = \min_{K(k)} \text{tr} [W P(k)], \quad (2.40a)$$

where W is a symmetric positive-definite weighting matrix, and

$$e(k) = \hat{x}_a(k) - x_a(k), \quad P(k) = E \{ e(k) e^T(k) \}. \quad (2.40b)$$

Subtracting Eq. (2.34a) from Eq. (2.39a) and using Eqs. (2.34b) and (2.39b), we obtain

$$e(k+1) = [I - K(k+1)H_a] [\bar{x}_a(k+1) - x_a(k+1)]. \quad (2.41)$$

It follows from the above equation that $P(k)$ satisfies the following recurrence relation,

$$P(k+1) = [I - K(k+1)H_a]M(k+1)[I - K(k+1)H_a]^T, \quad (2.42a)$$

where

$$\begin{aligned} M(k+1) &= E \{ [\bar{x}_a(k+1) - x_a(k+1)][\bar{x}_a(k+1) - x_a(k+1)]^T \} \\ &= E \{ [F_d e(k) - \eta_d(k)][F_d e(k) - \eta_d(k)]^T \} \\ &= F_d P(k) F_d^T + Q_d, \end{aligned} \quad (2.42b)$$

which is the covariance matrix of the estimation error before measurement.

Substituting Eq. (2.42a) into Eq. (2.40a), J can be found as

$$J = \text{tr} \left\{ W \left[[I - K(k+1)H_a]M(k+1)[I - K(k+1)H_a]^T \right] \right\}, \quad (2.43)$$

and its derivatives are

$$\frac{\partial J}{\partial K} = W \left[-2[I - K(k+1)H_a]M(k+1)H_a^T \right], \quad (2.44)$$

$$\frac{\partial^2 J}{\partial K^2} = 2W[H_a M(k+1)H_a^T] \geq 0. \quad (2.45)$$

J can be minimized with respect to K by letting $\frac{\partial J}{\partial K}$ equal to zero, that is,

$$-2[I - K(k+1)H_a]M(k+1)H_a^T \equiv 0. \quad (2.46)$$

From the above equation, $K^o(k+1)$ can be solved as

$$K^o(k+1) = M(k+1)H_a^T \times [H_a M(k+1)H_a^T]^{-1}. \quad (2.47a)$$

with initial condition

$$M(k_0) = M_0. \quad (2.47b)$$

Substituting Eq. (2.47a) into Eq. (2.42a), then

$$P(k+1) = [I - K^o(k+1)H_a]M(k+1). \quad (2.48)$$

As in the continuous case, we can let $\bar{a}(k_0) = 0$ by choosing

$$\hat{x}_a(k_0) = \bar{x}_{a_0}. \quad (2.49)$$

For a time invariant system, i.e. F_d , G_d , H_a , J_w , Q_d are all constant matrices, it can also be proved that the estimating process will reach a steady state as in the continuous case. A computer program DISC developed by Katz [28] can be used to find the steady state solution, but it is not able to handle the correlation between the process disturbance and measurement noise. So a program coded in FORTRAN was developed by the author to iterate Eqs. (2.47-2.48, 2.42b) until the steady state in Eqs. (2.47-2.48) is reached. Better techniques can be used to find the steady state solution at faster convergence speed but they are not considered here.

D. EXPERIMENTAL SYSTEM OBSERVABILITY ANALYSIS

For ease of analysis and notation, we will use the continuous formulation hereafter, and the system is assumed to be time-invariant.

D-1 Differential Equation Investigation

As derived in Appendix B-1, the system equations of the physical system, Eqs. (A-23)-(A-24), are repeated here

$$M_T \ddot{h} + S_\alpha \ddot{\alpha} + C_h \dot{h} + K_h h = F - \frac{T_\alpha}{l} - L, \quad (2.50a)$$

$$S_\alpha \ddot{h} + I_\alpha \ddot{\alpha} + C_\alpha \dot{\alpha} + K_\alpha \alpha = T_\alpha + M_\alpha. \quad (2.50b)$$

Without considering the driving forces and aerodynamic forces, i.e. *in vacuo*, and neglecting the damping effects, the equations normalized by the the semi-chord can be written as

$$\ddot{\bar{h}} = -\frac{\omega_h^2}{K} \bar{h} + \frac{K_2 \omega_\alpha^2 \bar{x}_\alpha}{K} \alpha, \quad (2.51a)$$

$$\ddot{\alpha} = \frac{\omega_h^2 \bar{x}_\alpha}{K \bar{r}_\alpha^2} \bar{h} - \frac{\omega_\alpha^2}{K} \alpha, \quad (2.51b)$$

where all the coefficients are defined in Appendix C.

Using a linear accelerometer located at a distance \bar{d} away from the elastic axis (EA) for linear acceleration measurement, \bar{z} , see Fig. II-3,

$$\begin{aligned} \bar{z} &= \ddot{\bar{h}} + \bar{d} \ddot{\alpha} \\ &= \frac{\omega_\alpha^2}{K} (K_2 \bar{x}_\alpha - \bar{d}) \alpha + \frac{\omega_h^2}{K} \left(\frac{\bar{d} \bar{x}_\alpha}{\bar{r}_\alpha^2} - 1 \right) \bar{h}, \end{aligned} \quad (2.52)$$

and the second derivative of this measurement is

$$\ddot{z} = \left[\frac{\omega_\alpha^2 \omega_h^2 \bar{x}_\alpha}{K^2 \bar{r}_\alpha^2} (K_2 \bar{x}_\alpha - \bar{d}) - \frac{\omega_h^4}{K^2} \left(\frac{\bar{d} \bar{x}_\alpha}{\bar{r}_\alpha^2} - 1 \right) \right] \bar{h} + \left[- \frac{\omega_\alpha^4}{K^2} (K_2 \bar{x}_\alpha - \bar{d}) + \frac{K_2 \omega_h^2 \omega_\alpha^2 \bar{x}_\alpha}{K^2} \left(\frac{\bar{d} \bar{x}_\alpha}{\bar{r}_\alpha^2} - 1 \right) \right] \alpha. \quad (2.53)$$

Combining Eqs. (2.52) and (2.53), we can solve for \bar{h} and α in terms of \bar{z} and $\ddot{\bar{z}}$ provided the determinant

$$\Delta = \frac{\omega_k^2 \omega_\alpha^2}{K^2} \left[(K_2 \bar{x}_\alpha - \bar{d}) \omega_\alpha^2 - \left(\frac{\bar{d} \bar{x}_\alpha}{\bar{r}_\alpha^2} - 1 \right) \bar{d} \omega_k^2 \right] \quad (2.54a)$$

$$= -\frac{\omega_h^2 \omega_\alpha^2}{K^2} \left[\frac{\bar{x}_\alpha \omega_h^2}{\bar{r}_\alpha^2} \bar{d}^2 + (\omega_\alpha^2 - \omega_h^2) \bar{d} - K_2 \bar{x}_\alpha \omega_\alpha^2 \right] \quad (2.54b)$$

does not vanish.

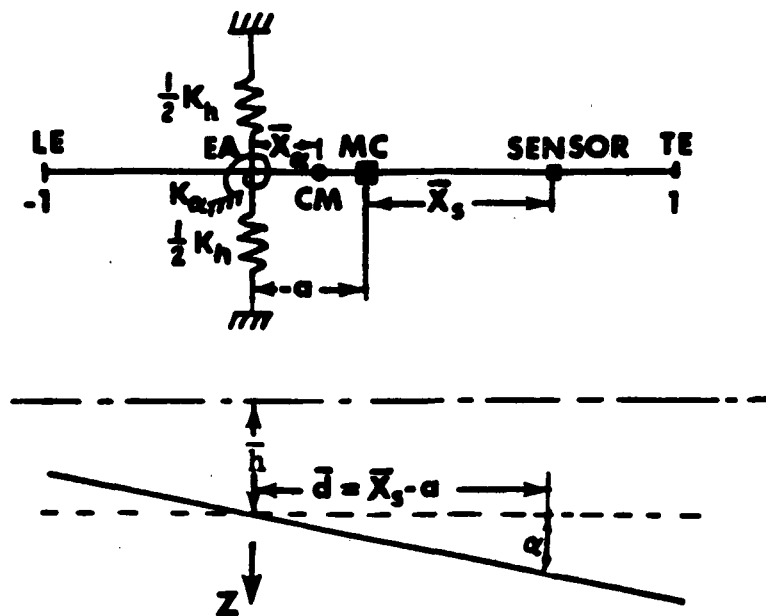


Fig. II-3 Acceleration Measurement
(An accelerometer located at \bar{x} , w.r.t. midchord (MC)
is \bar{d} from the elastic axis (EA))

Since $\bar{d} = \bar{x}_s - a$, the determinant Δ can be plotted as a function of \bar{x}_s for given system parameter values:

$$\omega_k^2 = 1821.58 \text{ (rad/sec)}^2$$

$$\omega_\alpha^2 = 3737.83 \text{ (rad/sec)}^2$$

$$K_2 = 0.3684$$

$$K = 0.96469$$

$$\bar{x}_\alpha = 0.19$$

$$\bar{d} = \bar{x}_s - a$$

$$\bar{r}_\alpha^2 = 0.37668$$

$$a = -0.3$$

$$\bar{x}_s : -1.0 \leq \bar{x}_s \leq 1.0. \quad (2.55)$$

as in Fig. II-4.

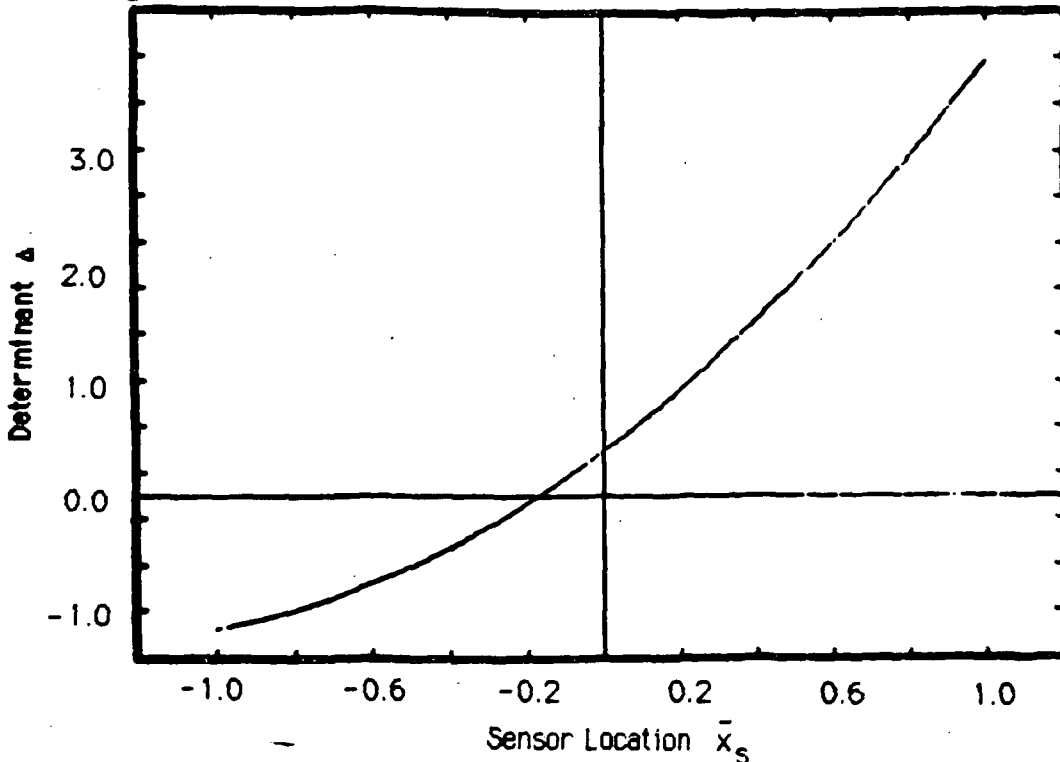


Fig. II-4 Determinant Δ vs Different Single Sensor Locations \bar{x}_s

It can be seen that $\Delta = 0$ at $\bar{x}_s \approx -0.2$, that is, the system will lose its observability if we put an accelerometer at this location. The following example will be used to explain the physical meaning of this singularity.

Example: (see Figure II-5)

Suppose an airfoil with mass, m and moment of inertia about EA, I_o is suspended at point O, which is of distance d away from EA. Assume a linear spring with spring constant K_h and an angular spring with spring constant K_α is attached to the airfoil at EA. Now displace EA laterally away from its neutral position a small distance x and release, the reaction force at point O in x direction R_x can be solved as follows.

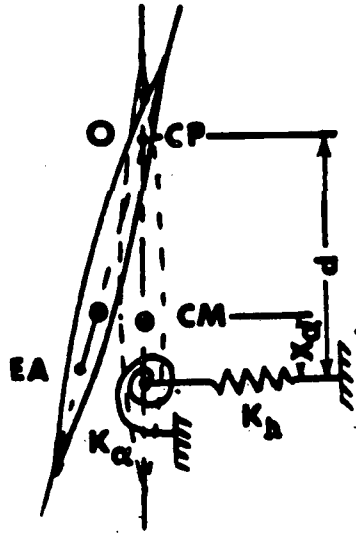


Fig. II-5 Example

The force and moment equations about point O are

$$R_x - K_h x = m \ddot{x}_c = m(d - x_\alpha) \ddot{\theta},$$

$$-K_\alpha \frac{x}{d} - K_h x d = I_o \ddot{\theta},$$

so

$$R_x = \frac{m(d - x_\alpha)}{I_o} [-K_\alpha \frac{x}{d} - K_h x d] + K_h x.$$

Since

$$\begin{aligned} K_h &= m\omega_h^2, \\ K_\alpha &= I_\alpha\omega_\alpha^2, \\ I_o &= mr_o^2 = mr_\alpha^2 - mx_\alpha^2 + m(d - x_\alpha)^2, \end{aligned}$$

and

$$r_o^2 = r_\alpha^2 - x_\alpha^2 + (d - x_\alpha)^2 = r_\alpha^2 - 2x_\alpha d + d^2,$$

so

$$\begin{aligned} R_z &= \frac{d - x_\alpha}{r_o^2} [-m\omega_h^2 x d - mr_\alpha^2 \omega_\alpha^2 \frac{x}{d}] + m\omega_h^2 x \\ &= \frac{mx}{r_o^2} [\omega_h^2 (r_\alpha^2 - 2x_\alpha d + d^2) - (d - x_\alpha) d \omega_h^2 - r_\alpha^2 \omega_\alpha^2 \frac{(d - x_\alpha)}{d}] \\ &= \frac{mx}{r_o^2} \frac{r_\alpha^2}{d} [\omega_\alpha^2 (x_\alpha - d) - d \omega_h^2 (\frac{x_\alpha d}{r_\alpha^2} - 1)]. \end{aligned} \quad (2.56)$$

Thus if d is so chosen that $R_z = 0$, the accelerometer will have zero measurement at that position. Physically, this is the center of percussion (CP), where there is zero specific force. Comparing with Eq. (2.54a), they are equivalent when $K_2 = 1$. Since plane motion is involved in this example and when there are no other forces applied, the instantaneous center will be located at the center of percussion, where the ratio of linear and angular accelerations is such that there are no movements during vibration [29, p. 481]. When external forces are applied, the acceleration measurements at CP may not be zero but the ratio of the incoming linear and angular components is such that there will be no distinctions between them. This can be seen by letting

$$\omega_\alpha^2 (x_\alpha - d) = d \omega_h^2 (\frac{x_\alpha d}{r_\alpha^2} - 1)$$

in Eq. (2.52). Then the measurement contains only one of the frequency components, either plunge or pitch but not both.

D-2 Observability Matrix

A more systematic way to check the observability is to write the system equation in the state space form as Eq. (2.13). Equation (2.11) is first used for this investigation. If only one accelerometer is used, the measurement equation can be written as

$$z(t) = H_{zd}\dot{x}(t) + v(t), \quad (2.57a)$$

where

$$H_{zd} = [0 \ 1 \ 0 \ (\bar{x}_0 - a)], \quad (2.57b)$$

and

$$x(t) = [\bar{h}(t) \ \dot{\bar{h}}(t) \ \alpha(t) \ \dot{\alpha}(t)]^T. \quad (2.57c)$$

Using Eq. (2.29), we have for our physical system that

$$\begin{aligned} H &= H_{zd}F, \\ J_u &= H_{zd}G, \\ v(t) &= H_{zd}\Gamma w(t) + v'(t), \\ R_v &= H_{zd}\Gamma Q_w\Gamma^T H_{zd}^T + R'_v, \\ V &= Q_w\Gamma^T H_{zd}^T, \end{aligned} \quad (2.58)$$

where we assume $V' = 0$.

Then the observability matrix O_{ob} can be constructed as

$$O_{ob} = \begin{bmatrix} H \\ HF \\ HF^2 \\ HF^3 \end{bmatrix}. \quad (2.59)$$

In general, O_{ob} is an $(n_{ob} \times n_s)$ by n_s rectangular matrix. The determinant of the n_s by n_s square matrix $O_{ob}^T O_{ob}$, $\det(O_{ob}^T O_{ob})$, can be plotted as a function of \bar{x}_s . In this formulation the aerodynamic effect can be considered easily by using Eq. (2.12) which adds an additional aerodynamic state. Now the measurement distribution matrix becomes

$$H_{zd} = [0 \ 1 \ 0 \ (\bar{x}_s - a) \ 0], \quad (2.60a)$$

$$z(t) = [\bar{h}(t) \ \dot{\bar{h}}(t) \ \alpha(t) \ \dot{\alpha}(t) \ \beta(t)]^T, \quad (2.60b)$$

and the observability matrix will be

$$O_{ob} = \begin{bmatrix} H \\ HF \\ HF^2 \\ HF^3 \\ HF^4 \end{bmatrix}. \quad (2.61)$$

The $\det(O_{ob}^T O_{ob})$ can thus be plotted for various wind speeds. Figure II-6a is a plot of the theoretical estimation error performance index $\text{tr}(WP)$ versus different single sensor locations \bar{x}_s at zero wind speed, where $W = \text{diag}[1, 10^{-1}, 10, 10^{-2}, 1]$. This result is obtained from the steady state covariance analysis, it gives finite estimation error for finite power spectral density inputs of the process disturbance and measurement noise even at $\bar{x}_{s,\min}$. Figure II-6b shows the $\det(O_{ob}^T O_{ob})$ versus different single sensor locations \bar{x}_s at zero wind speed. For different wind speeds, the plots look the same except the $\bar{x}_{s,\min}$ corresponding to the minimum value of $\det(O_{ob}^T O_{ob})$ will be different.

EST. ERROR VS. LOCATIONS OF SENSOR ALONG THE WING CHORD
WIND SPEED = 1.00 m/sec

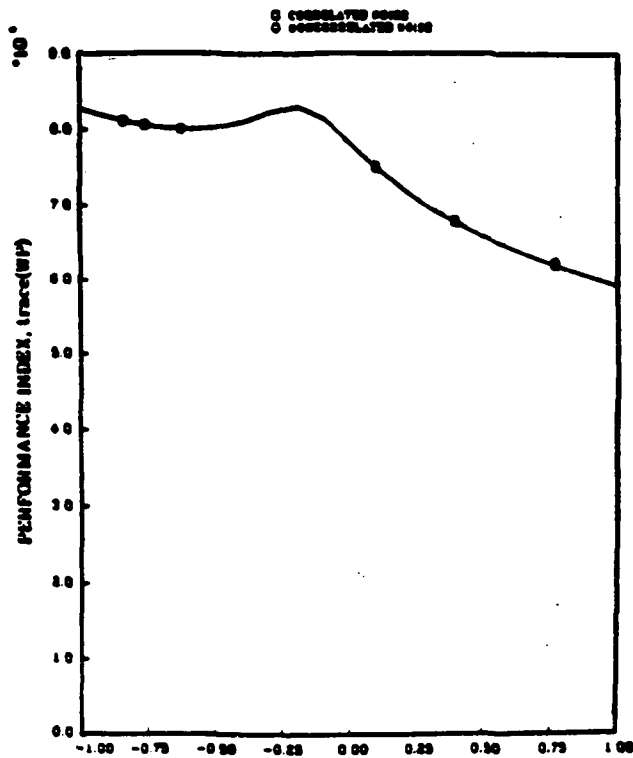


Fig. II-6a Performance Index $tr(WP)$
vs Different Single Sensor Locations \bar{x} , at Zero Wind Speed

DETERMINANT OF OB MATRIX VS. SENSOR LOCATION
WIND SPEED = 1.0 m/sec

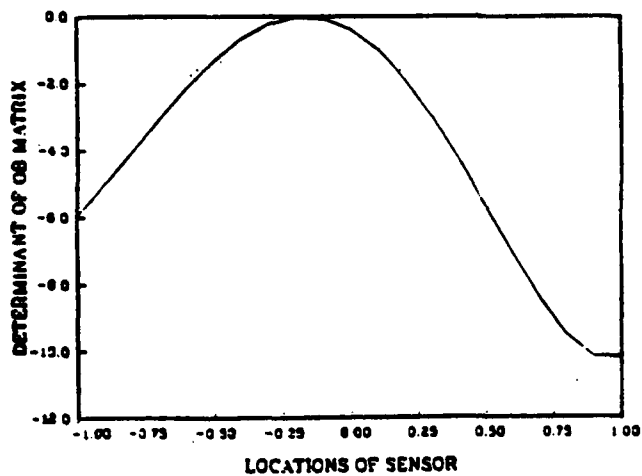


Fig. II-6b Determinant $\det(O_{ob}^T O_{ob})$
vs Different Single Sensor Locations \bar{x} , at Zero Wind Speed

By comparing the plots in Fig. II-6, we can see that $\bar{x}_{s,\min}$ corresponds to the unobservable location of the sensor. The same conclusion also holds for varying wind speeds. Otherwise, the absolute magnitude of $\det(O_{ob}^T O_{ob})$ bears no direct relationship with the observability of the system. This can be seen that for the same magnitude of $\det(O_{ob}^T O_{ob})$ the corresponding sensor locations can have different results for $\text{tr}(WP)$. Actually, the $\det(O_{ob}^T O_{ob})$ can only provide binary information about the system to be analyzed, i.e. either observable (when $\det(O_{ob}^T O_{ob}) \neq 0$) or unobservable (when $\det(O_{ob}^T O_{ob}) = 0$) [16, p. 457].

D-3 Transfer Function and Modal Form

Using the state space formulation Eq. (2.13a) and the measurement equation Eq. (2.13b), we can find the transfer function from $w(t)$ to $z(t)$ as

$$\frac{Z(s)}{W(s)} = sHT(sI - \Lambda)^{-1}T^{-1}\Gamma, \quad (2.62)$$

and the modal form as

$$\dot{\xi}(t) = \Lambda\xi(t) + T^{-1}Gu(t) + T^{-1}\Gamma w(t), \quad (2.63a)$$

$$z(t) = HT\xi(t) + J_u u(t) + v(t), \quad (2.63b)$$

where $\Lambda = T^{-1}FT$, $\xi(t) = T^{-1}x(t)$, and T is the right eigenvector matrix of the open-loop system.

The product of disturbability times observability can be determined by examining the transfer functions or the modal distribution matrices. Figure II-7 shows the pole-zero loci for different single sensor locations and various wind

speeds. The conclusion from this figure is that at the unobservable or undisturbable position of the sensor, there is an exact pole-zero cancellation of the pitch mode. It seems that as the separation between the pole and zero increases, the estimation error for that mode decreases. Although this qualitative behavior is general for all cases, we did not use it for best sensor location searches.

If (z, w) were scaled so that one unit of each component is of comparable significance, then $(HT)_i$ and $(T^{-1}\Gamma)_i$ indicate relative observability and disturbance of i th mode. Outer product of these two vectors forms a rank one residue matrix. The norm of this matrix equals the product of the length of these two vectors, and it is a measure of the significance of i th mode in the input-output relation.

A thorough examination of the residue matrices reveals useful information about its connection with the magnitude of the estimation error and it can help to locate the unobservable or undisturbable location of the sensor.

E. CRITERIA FOR CHOOSING THE BEST SENSOR LOCATION

The choice of sensor location represents a significant design freedom available to the designer. However, it is usually not a very straightforward choice to make. To make a good choice, it is necessary to have a standardized criterion to choose the sensor number and their locations. Most important, it must be a quantitative measure that can be easily computed and have a physical interpretation so that engineering judgement can be based upon it. In order to get a perspective on this research, it may be helpful to review the criterion proposed by Vander Velde [12-14].

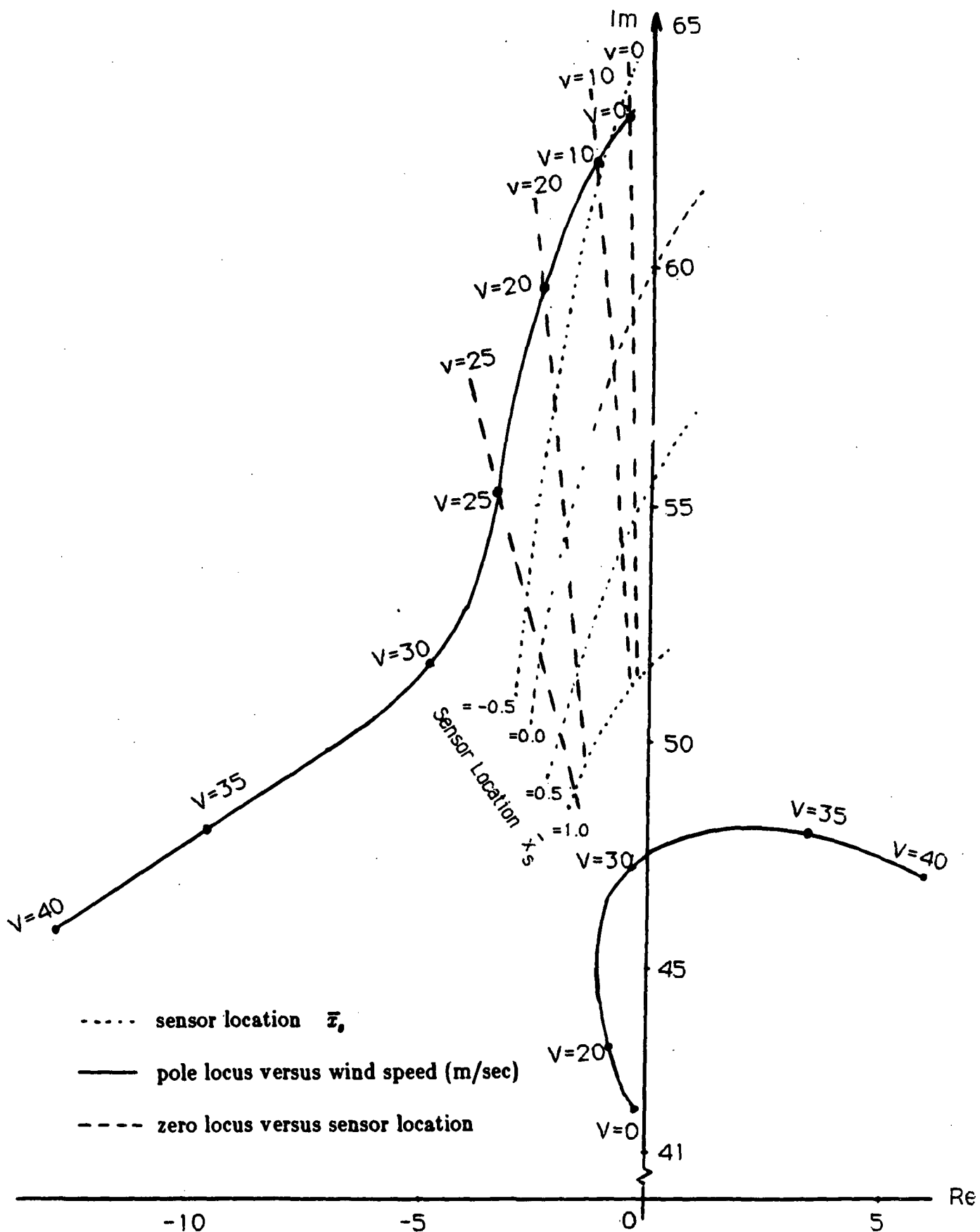


Fig. II-7 Pole-Zero Loci for Different Single Sensor Location at Various Wind Speeds

E-1 Degree of Observability (DO)

For the Kalman filter with uncorrelated process disturbance and measurement noise, i.e. $V = 0$, from Eq. (2.24) the estimation error covariance matrix can be found satisfying the following equations

$$\dot{P}(t) = FP(t) + P(t)F^T - P(t)H^TR_s^{-1}HP(t) + \Gamma Q_w \Gamma^T, \quad t \geq t_0, \quad (2.64a)$$

$$P(t_0) = P_0. \quad (2.64b)$$

Vander Velde chooses $Q_w = 0$ by arguing that it is an external influence not related to the sensor set (however, this is not true when accelerometers are used as we pointed out at the end of Section C-1) and uses the information matrix $S(t) = P^{-1}(t)$ formulation, then Eq. (2.64) becomes

$$\dot{S}(t) = -S(t)F - F^TS(t) + H^TR_s^{-1}H, \quad t \geq t_0, \quad (2.65a)$$

$$S(t_0) = S_0, \quad (2.65b)$$

using the fact that

$$\dot{P}(t) = -P(t)\dot{S}(t)P(t). \quad (2.66)$$

Assuming there is no information about the initial state, i.e. $P_0 = \infty$ or $S_0 = 0$, one is interested in measuring how much information has been accumulated in $S(T_e)$ up to a specified estimation time T_e , that is, the size of $S(T_e)$. This can be obtained by reference to the quadratic surface in the x -space, i.e.

$$x^TS^{-1}x = 1. \quad (2.67)$$

After the transformation

$$y = Tx, \quad (2.68)$$

where $T = \text{diag} [|e_{1_{\max}}|, \dots, |e_{i_{\max}}|, \dots, |e_{n_{\max}}|]$ and $e_{i_{\max}}$ are the maximum errors that can be tolerated in the directions x_i , the volume of the transformed ellipsoid can now be measured in the equimeasure space. The degree of observability (DO) is defined as the maximum spherical volume (V_S) contained in the n_e -dimensional ellipsoid (V_E) plus a lesser weighted excess volume ($V_E - V_S$) due to the nonideal volume distribution. Specifically,

$$\text{DO} = \left[V_S + \frac{V_S}{V_E} (V_E - V_S) \right]^{1/n_e}, \quad (2.69a)$$

with

$$V_E = \prod_{i=1}^{n_e} \sqrt{\nu_i}$$

$$V_S = (\sqrt{\nu_{\min}})^{n_e}, \quad (2.69b)$$

and ν_i are the eigenvalues of $TS(T_e)T$.

E-2 Sensor Location Index (SLI)

In Section A, the performance index for optimally designed estimator at steady state is found to be

$$J_{ss}^o = \min_{K_{ss}} \text{tr} [WP_{ss}], \quad (2.70)$$

where P_{ss} is the solution of the steady state Riccati equation

$$\begin{aligned} [F - \Gamma VR_v^{-1}H]P_{ss} + P_{ss}[F - \Gamma VR_v^{-1}H]^T - P_{ss}H^TR_v^{-1}HP_{ss} \\ + \Gamma Q_w \Gamma^T - \Gamma VR_v^{-1}V^T\Gamma^T = 0. \end{aligned} \quad (2.71)$$

It can be seen that P_{ss} as well as J_{ss}^o are functions of the measurement distribution matrix H . Specifically, they are functions of the sensor location along the wing chord, \bar{x}_s , for single sensor case. This is also true for multiple sensors, in which case, \bar{x}_s will be interpreted as a vector. The performance index can be plotted as a function of \bar{x}_s , and by a simple judgement, the location where it has the smallest value should correspond to the best sensor location under given conditions.

The above conclusion suggests that a similar sensor location index

$$J_{SL}^o = \min_H J_{ss}^o = \min_H \{ \min_{K_{ss}} \text{tr} [WP_{ss}] \} \quad (2.72a)$$

can be used to find the best sensor location, where W is a symmetric positive-definite weighting matrix and can be chosen similarly to T as

$$W = \text{diag} \left[\frac{1}{e_{1_{\max}}^2}, \dots, \frac{1}{e_{i_{\max}}^2}, \dots, \frac{1}{e_{n_{\max}}^2} \right]. \quad (2.72b)$$

To incorporate the constraint of Eq. (2.71), we introduce the use of a Lagrangian multiplier matrix Λ , and denote the Eq. (2.71) by $f(P_{ss}, H)$. Then Eq. (2.72) can be written as

$$J_{SL} = \min_H \text{tr} [WP_{ss} + \Lambda f(P_{ss}, H)], \quad (2.73)$$

since

$$\Lambda f(P_{ss}, H) = 0. \quad (2.74)$$

After substituting and using the gradient table in Appendix D and Eq. (2.23), we can find that

$$\frac{\partial J_{SL}}{\partial P_{ss}} = [F - K_{ss}H]^T \Lambda + \Lambda [F - K_{ss}H] + W, \quad (2.75)$$

$$\frac{\partial J_{SL}}{\partial H} = -2K_{ss}^T \Lambda P_{ss}. \quad (2.76)$$

The gradient of J_{SL} w.r.t. each individual sensor location is obtained by applying the chain rule. Using Eqs. (2.58) and (2.60a), we have in our case that

$$\frac{\partial J_{SL}}{\partial \bar{x}_s} = -2K_{ss}^T \Lambda P_{ss} F_{4j}^T, \quad (2.77)$$

where F_{4j} is a 1 by n_s matrix which is identical to the 4th row of the F matrix. For multiple sensor case, \bar{x}_s can be considered as a n_{ob} by 1 vector.

In order to minimize J_{SL} , both $\frac{\partial J_{SL}}{\partial P_{ss}}$ and $\frac{\partial J_{SL}}{\partial H}$ must vanish.

E-3 Gradient Search Procedure

The gradient searching process for the optimal sensor location can be proceeded as:

1. guessing initial value of \bar{x}_s with which to compute the component values of the H matrix,
2. using LOPTSYS to solve for P_{ss} and K_{ss} ,
3. solving the Riccati equation of Eq. (2.75) for Λ ,
4. computing the gradient $\frac{\partial J_{SL}}{\partial H}$ of Eq. (2.76), and $\frac{\partial J_{SL}}{\partial \bar{x}_s}$ of Eq. (2.77),
5. if $\frac{\partial J_{SL}}{\partial \bar{x}_s} \leq \epsilon$ (a small number close to zero given by the designer), stop; otherwise
6. computing

$$\bar{x}_{s_{\text{new}}} = \bar{x}_{s_{\text{old}}} - \frac{\partial J_{SL}}{\partial \bar{x}_s} \Delta \bar{x}_s, \quad (2.78)$$

under the constraint of $-1 \leq \bar{x}_s \leq 1$,

7. go back to step 2.

This procedure is also shown by the flow chart in Fig. II-8.

Figure II-9 shows the sensor location index J_{SL} versus different single sensor locations \bar{x}_s and Table II-1 gives the values of J_{SL} and $\frac{\partial J_{SL}}{\partial \bar{x}_s}$. From

which we can see that $\frac{\partial J_{SL}}{\partial \bar{x}_s}$ truly reflects the slope of the curve and a local minimum exists.

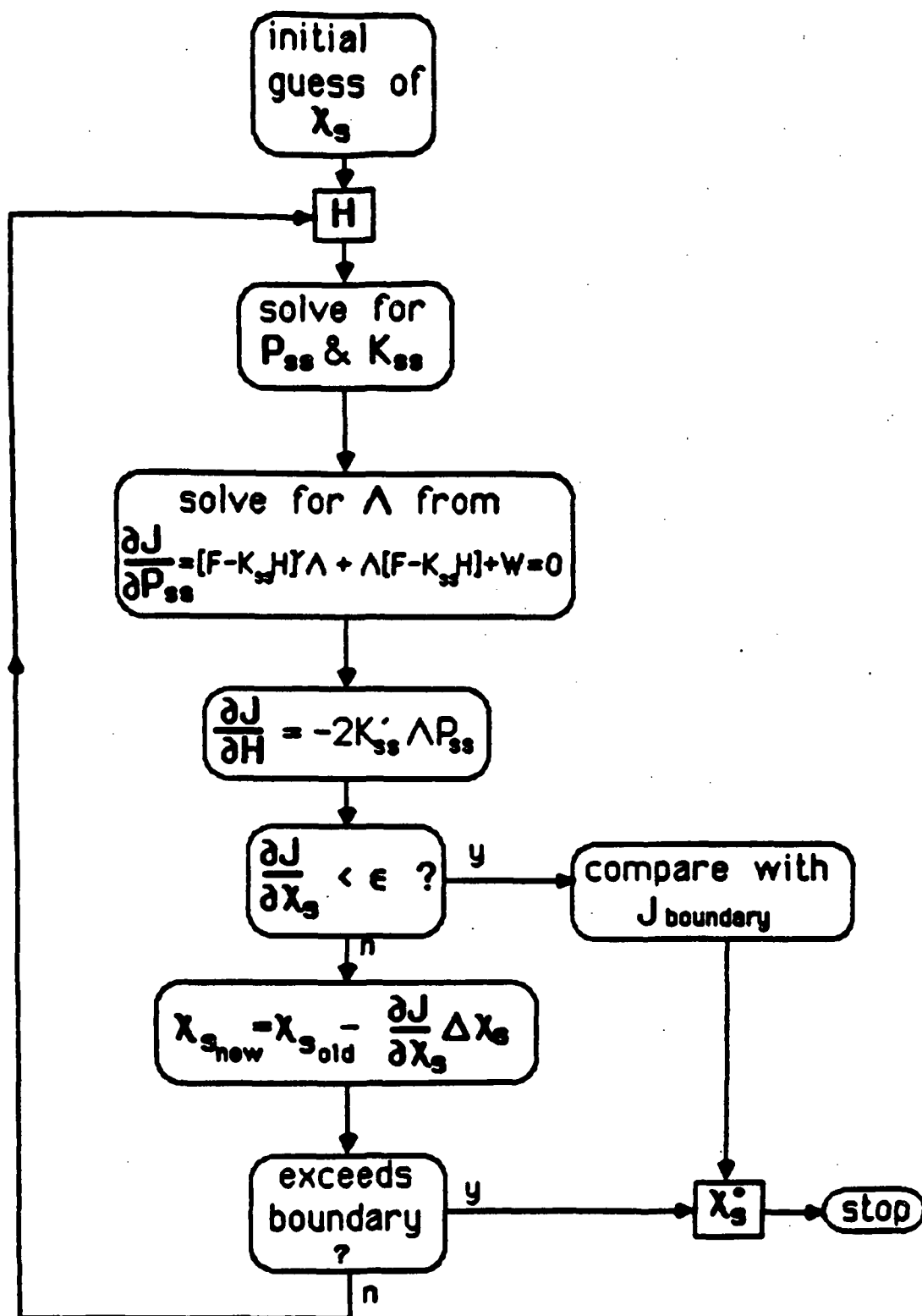


Fig. II-8 Gradient Search Procedure for the Optimal Sensor Location

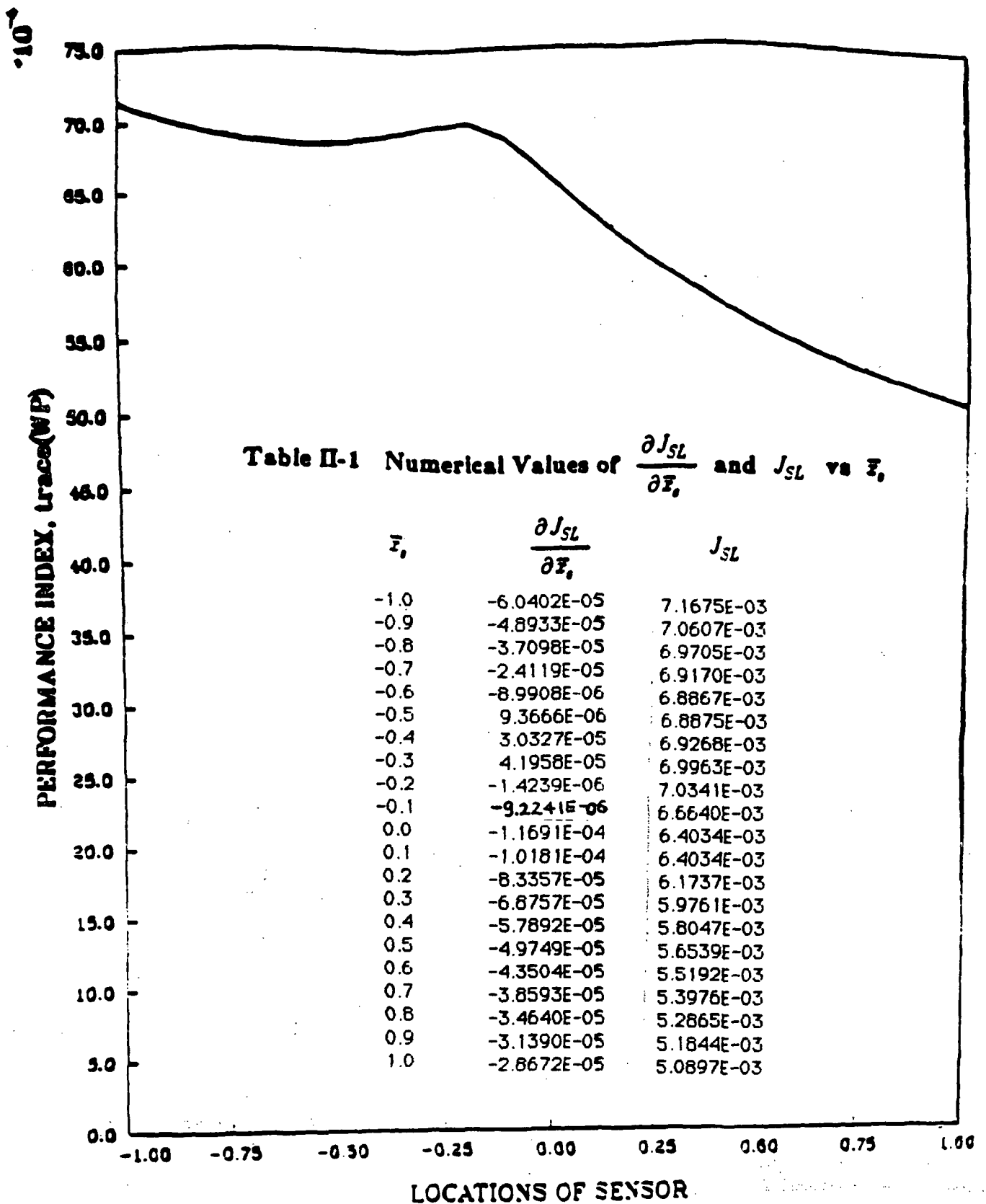


Fig. II-9 Sensor Location Index J_{SL} vs Different Single Sensor Locations \bar{x}_s

Using the gradient $\frac{\partial J_{SL}}{\partial H}$ for sensor location search is easy and convenient, however, $\frac{\partial J_{SL}}{\partial H} = 0$ can lead to a local minimum. So the use of it must be with care.

E-4 Comparison between the SLI and DO When $Q_w = 0$

Since in the actual applications, the process disturbance may be close to zero, i.e. $Q_w \rightarrow 0$, and $V \rightarrow 0$, then the P_{∞} will approach zero. In this case, we could take into account the estimation time T_e to avoid the singular result and solve Eq. (2.24) by integration.

Figure II-10 shows the result by letting $Q_w = 0$, $V = 0$ and $T_e = 1$ sec. It can be seen that the trailing edge is still the best location to install an accelerometer while the center of percussion is still the worst.

Using Vander Velde's information matrix formulation, Fig. II-11 shows the sum of its weighted diagonal terms versus different single sensor locations. It shows the trailing edge is the best sensor location, however at the center of percussion the index value does not go to zero. Because, in modal form, only one diagonal term vanishes when the sensor is at the center of percussion.

Figure II-12 is a plot of the information matrix determinant versus different single sensor locations and it shows zero value at the center of percussion while the best sensor location is still at the trailing edge.

For finite time estimation, the SLI is independent of the initial value assumptions because of their fast decaying rates for stable systems. However, this is not true for the DO. For some cases, the available initial information may dominate the value of the DO and makes the sensor location preference indistinguishable.

WIND SPEED = 1.00 m/sec

□ = NONCORRELATED NOISE

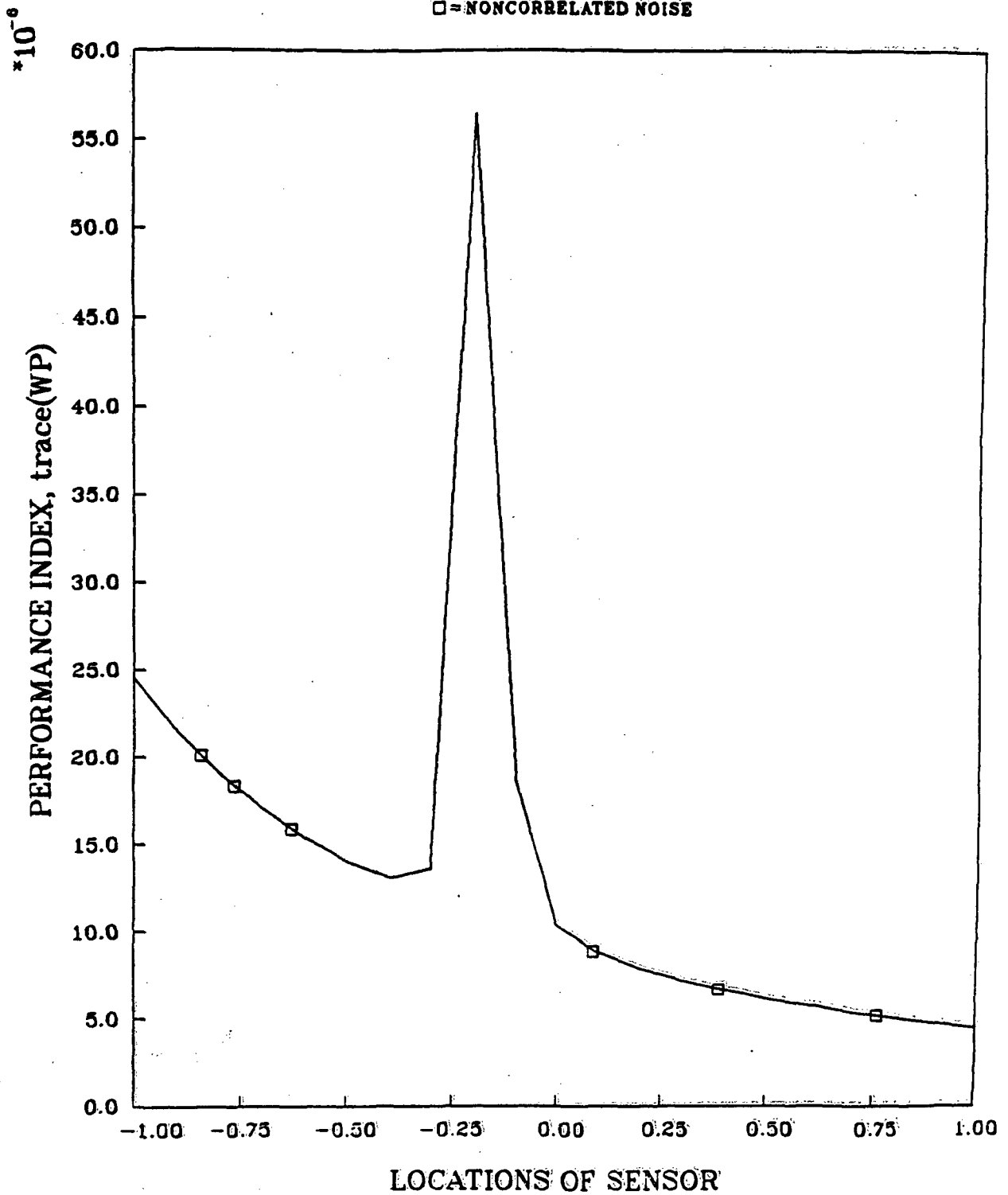
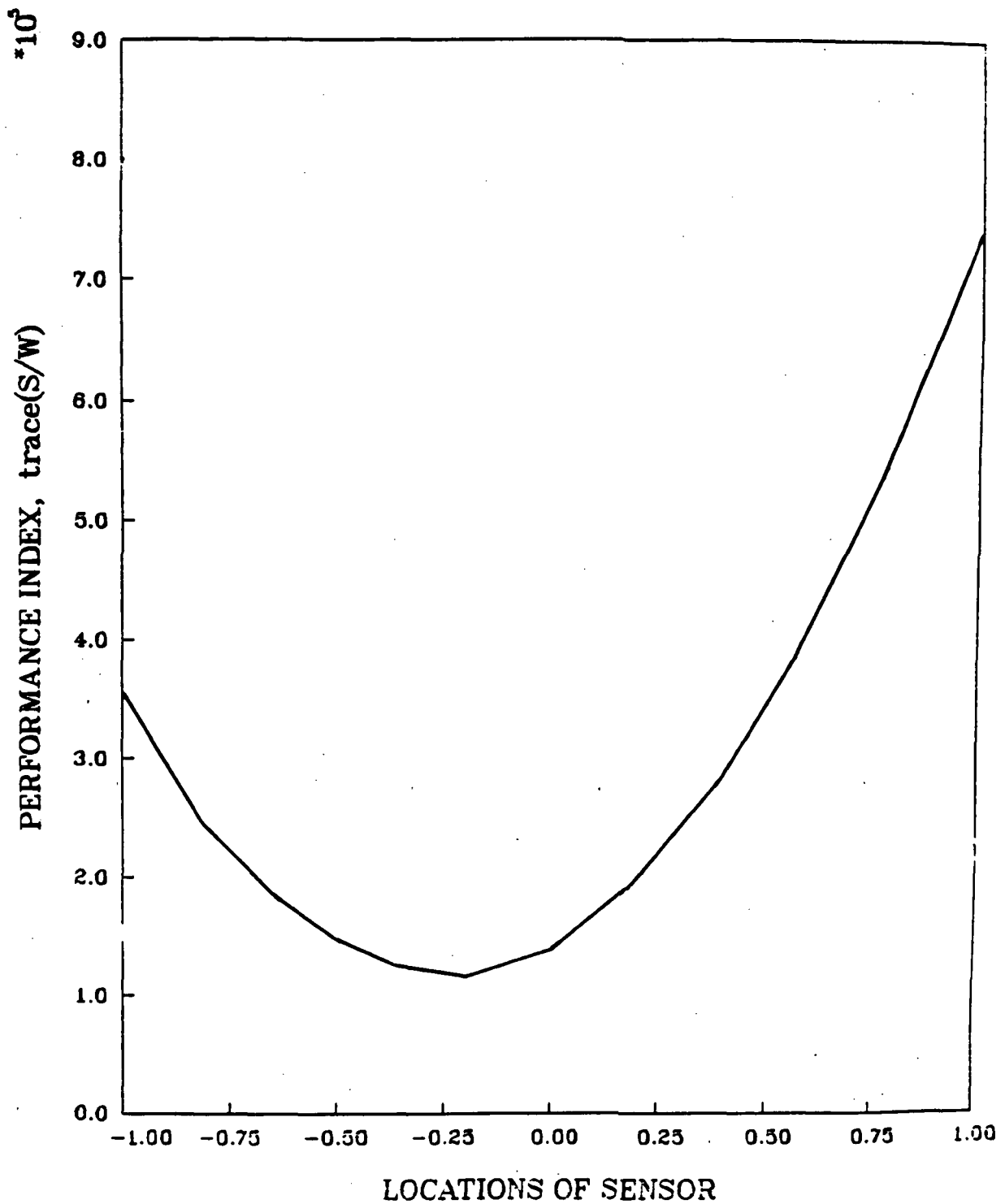


Fig. II-10 Sensor Location Index J_{SL} vs Different Single Sensor Locations \bar{x} , for $Q_v = 0$, $V = 0$, $T_e = 1$ sec

WIND SPEED = 1.00 m/sec, ESTIMATION TIME = 1.00 sec.



**Fig. II-11 Performance Index $\text{tr}(S/W)$
vs Different Single Sensor Locations \bar{x}_i for $T_e = 1$ sec**

WIND SPEED = 1.00 m/sec, ESTIMATION TIME = 1.00 sec.

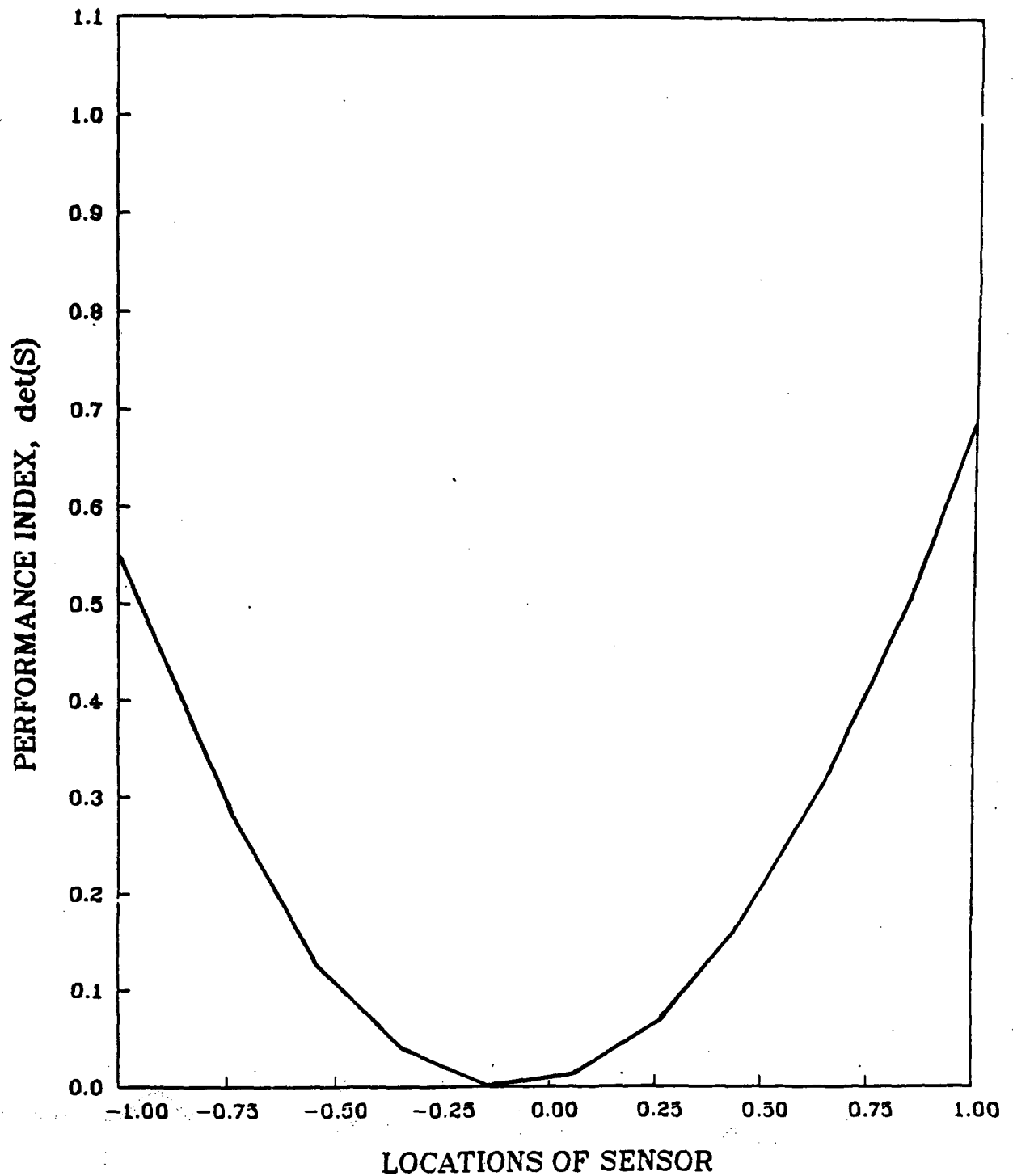


Fig. II-12 Performance Index $\det(S)$
vs Different Single Sensor Locations \bar{x} , for $T_e = 1$ sec

E-5 Relative Merits of the SLI versus DO

Compared with the degree of observability (DO) suggested by Vander Velde, we have chosen to use the sensor location index (SLI) because it is more convenient for our purposes for the following reasons:

- 1) Practically, it is much more meaningful to measure directly the state estimation error than the hypothetical ellipsoid volume, especially when the system state has physical meanings.
- 2) The measurement noise will include the process disturbance when accelerometers are used, see Eq. (2.29). This inclusion of the process disturbance is highly sensor location dependent and it may affect the choice of the optimal sensor location. The sensor location index takes this into account in its formulation. However, in our case both the SLI and DO give the same answer.
- 3) When evaluated for a finite time to avoid singular results the sensor location index is independent of the initial value.
- 4) The existing design program LOPTSYS and some of its supporting subroutines were developed at Stanford. They are available and make it straightforward to compute J_{SL} ; the value of J_{SL} could be computed as a by product during the design process.
- 5) Most important of all, this choice of sensor location index J_{SL} makes the gradient formulation easy to handle and compute thus making J_{SL} tractable for the optimal sensor location search.

F. DOUBLE SENSORS CASES

Figure II-13 shows the theoretical results of single sensor as well as double sensors, with one sensor fixed, versus varying sensor locations along the wing chord. Due to the existence of Q_w and V , there is no simple relationship between the single sensor and collocated double sensors at the same sensor location. Adding a second sensor generally improves the SLI, with the improvement increasing as the second sensor moves toward the trailing edge.

The best location for the second sensor is still at the trailing edge, same as the first one. This result shows however the negative side of our sensor location index definition, namely it is too dependent on the mathematical modeling of the physical system. For example, a practical estimator designer would rather choose to put one sensor at the leading edge and one at the trailing edge. Their measurements can then be used to solve for the linear and angular accelerations which are independent of the system modeling. So the two sensors can get 2 DOF information directly albeit the initial conditions. Since these dc information is rarely needed for flutter suppression, it suggests that a frequency-band weighted SLI may be useful to cope with system parameter uncertainties and modeling errors. A more realistic criterion which takes this into consideration will be recommended for the future research.

WIND SPEED = 20.94 m/sec

DOUBLE SENSORS WITH ONE FIXED AT -1.
DOUBLE SENSORS WITH ONE FIXED AT -.5
DOUBLE SENSORS WITH ONE FIXED AT 0.

DOUBLE SENSORS WITH ONE FIXED AT .5
DOUBLE SENSORS WITH ONE FIXED AT 1.
SINGLE SENSOR

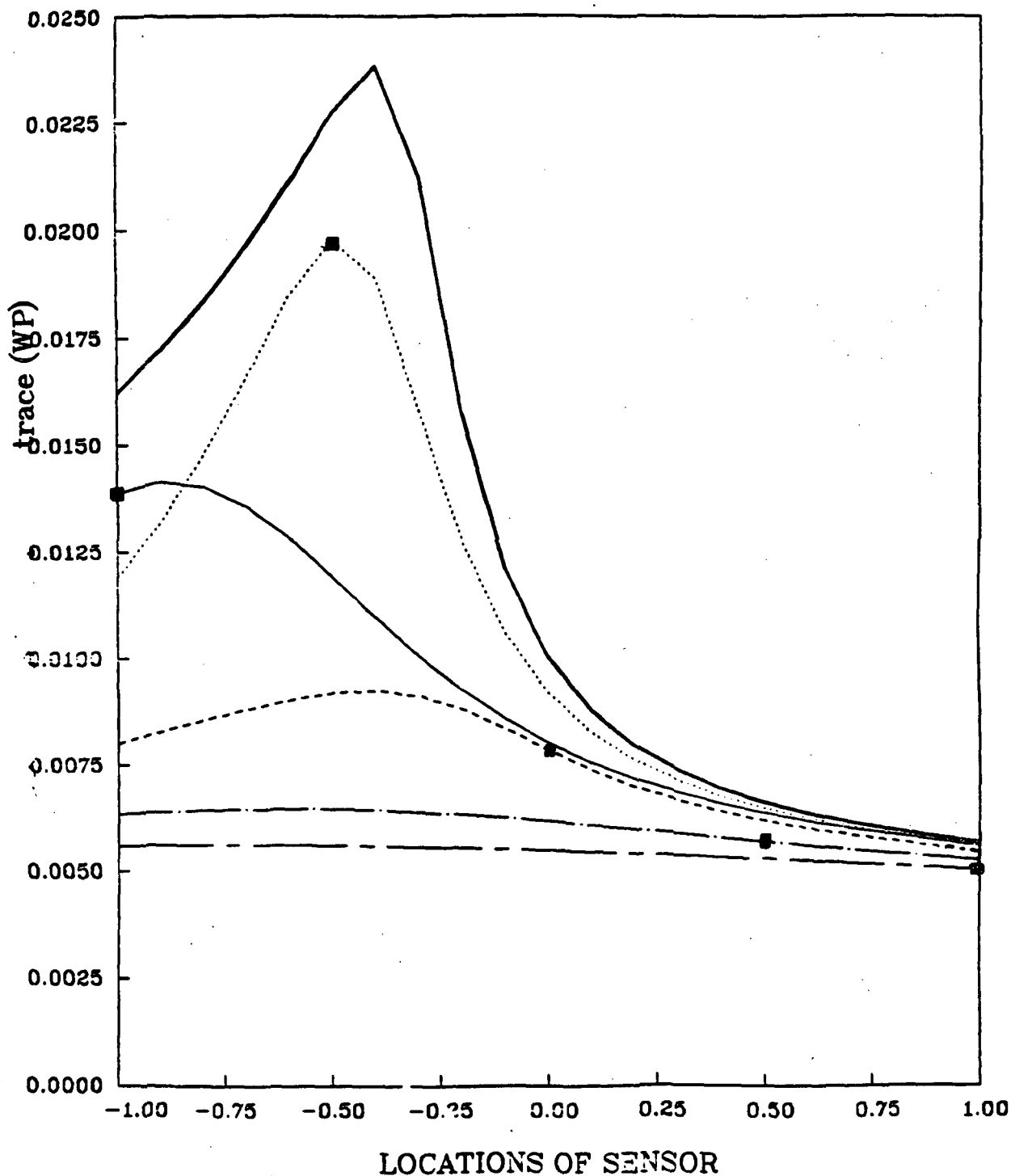


Fig. II-13 Single Sensor and Double Sensors Cases

Chapter III

EXPERIMENTAL APPARATUS

A. INTRODUCTION

The idea of the typical section wing was devised during the 1930's by Theodorsen and Garrick to simulate an actual wing by matching the properties at a station 70-75% of the distance from the centerline to the tip [18, p. 189]. Ideally, as shown in Fig. III-1, it consists of a thin, rigid wing immersed in a two dimensional, incompressible airstream, suspended by two sets of springs allowing elastically restrained but uncoupled rotation about the elastic axis (EA, line of shear centers [18, p. 281]) and translation perpendicular to the free stream airflow.

This chapter describes an experimental apparatus that is the physical realization of the ideal two DOF (degree of freedom) typical section wing. Its suspension system was built by Rock in 1978 to investigate the aeroelastic stability of a simple, two DOF wing in Stanford's small, subsonic wind tunnel [25]. This suspension system provides spring restraints for plunge and pitch movements while allowing virtually no elastic coupling between these two motions. It is also characterized by small structural damping and relatively high stiffness in the remaining DOF's.

A schematic view of the complete system is shown in Fig. III-2. A description of the major subsystems is presented, followed by a summary of system parameters and a discussion of the system performance.

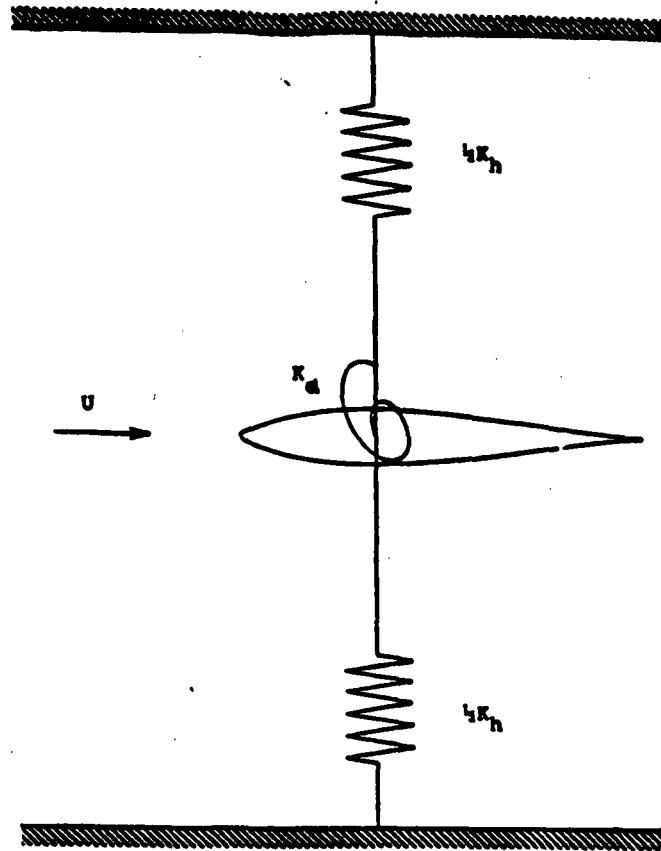


Fig. III-1 Typical Section Wing

B. WIND TUNNEL

The wind tunnel used in this research at Stanford University is a small, closed-circuit, subsonic, vented tunnel, see Fig. III-3 for its plane view [56]. It has a dynamic pressure range of 200 N/m^2 to 2000 N/m^2 (an airspeed range of 19 m/sec to 65 m/sec , $M_{\max} = 0.2$). The dynamic pressure is controlled by adjusting the pitch angle of a 16-blade constant speed (19 Hz) fan. Five screens upstream reduce the mean turbulence level at the test section to approximately 1% . The contraction ratio is 8.67 and the total distance around the center line is 25.1 m .

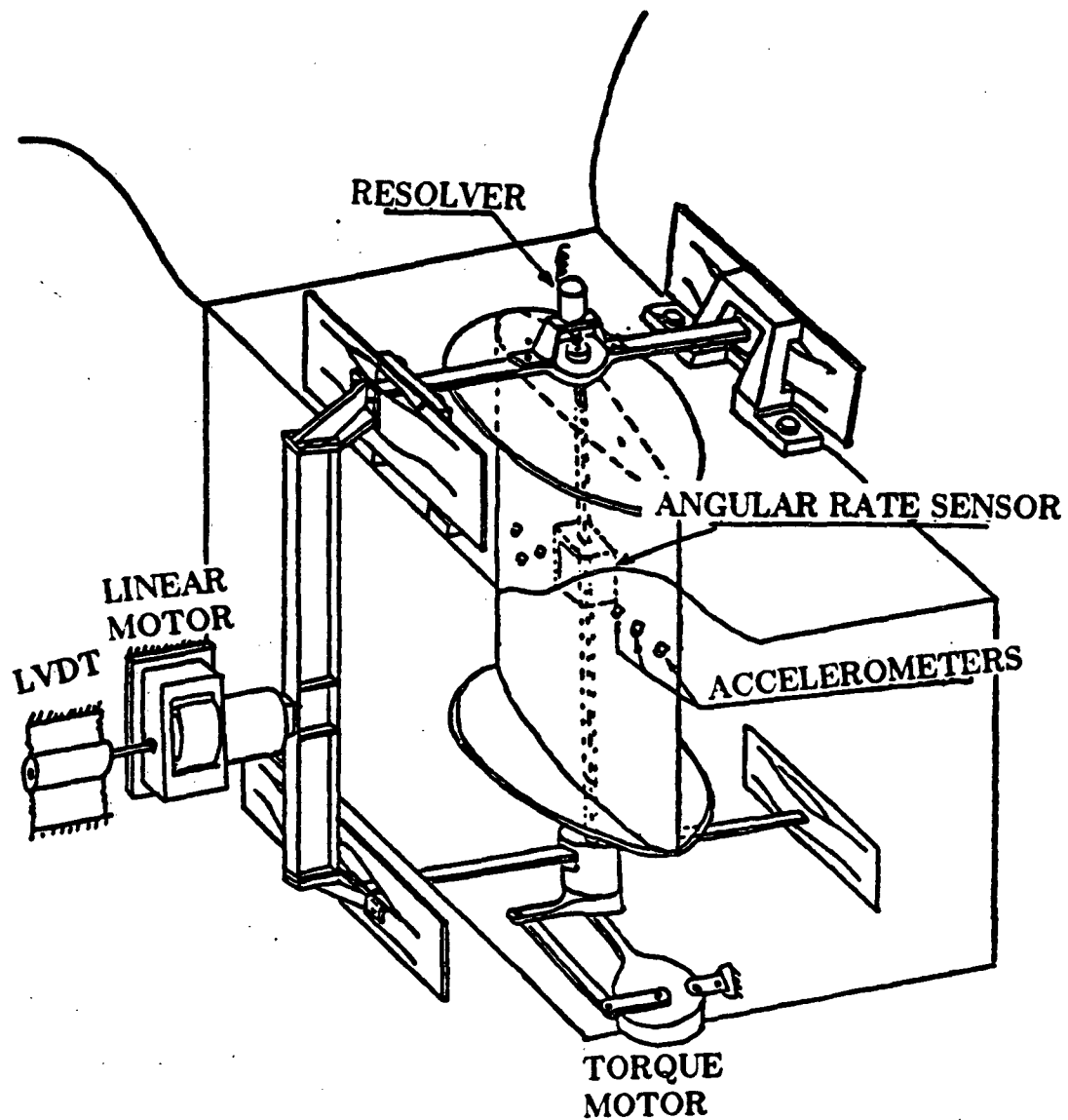


Fig. III-2 Experimental Apparatus

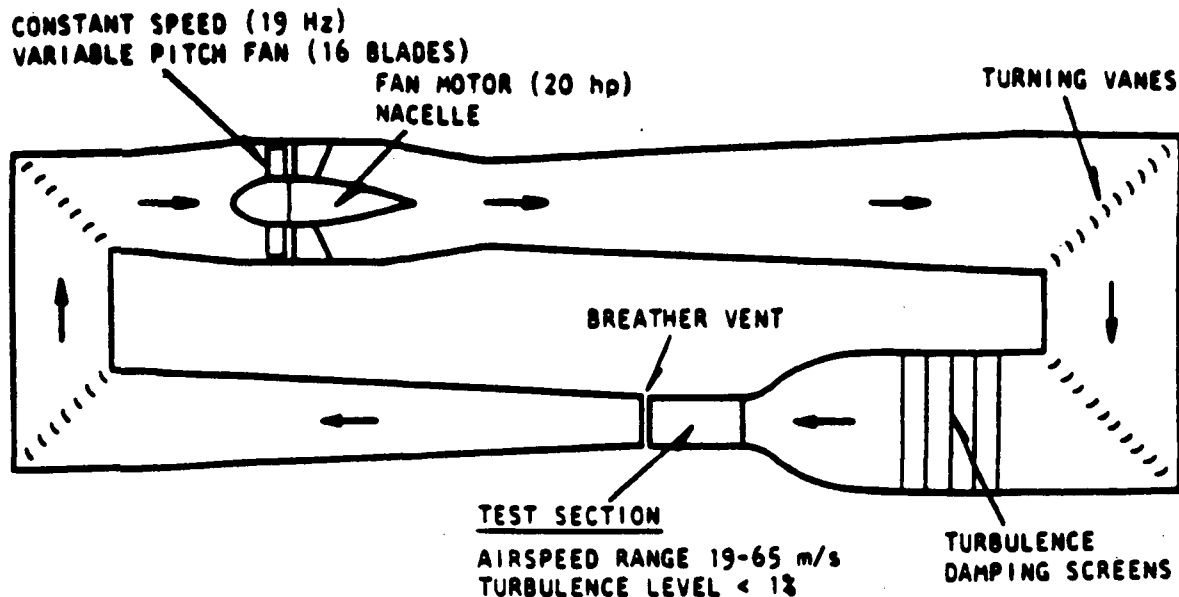


Fig. III-3 Plan View of the Stanford Subsonic Wind Tunnel

The test section is 0.4572 m (18 in.) square by 0.9017 m (35.5 in.) long. It consists of a welded steel frame with three removable Lexan walls and one steel bottom wall, mounted on a welded steel cart with castors for ease of handling.

The suspension system and actuators are bolted to mounts welded to the test section. All have been machined in place to provide proper alignment and rigidity. The only hardware inside the test section is the airfoil with its endplates as well as those sensors inside the airfoil for the "in-flight" estimation. All suspensions, actuators and monitoring sensors are located externally.

C. AIRFOIL

The airfoil is constructed of a fiberglass-laminate skin wrapped around a foam core. It has a NACA 0015 profile with a span of 0.4191 m (16.5 in.) and a chord of 0.2413 m (9.5 in.). A core of styrofoam is cut to the shape using a hot-wire passed over two aluminum templates (shown in Fig. III-4) numerically machined to NACA 0015 specifications [57, p. 113].

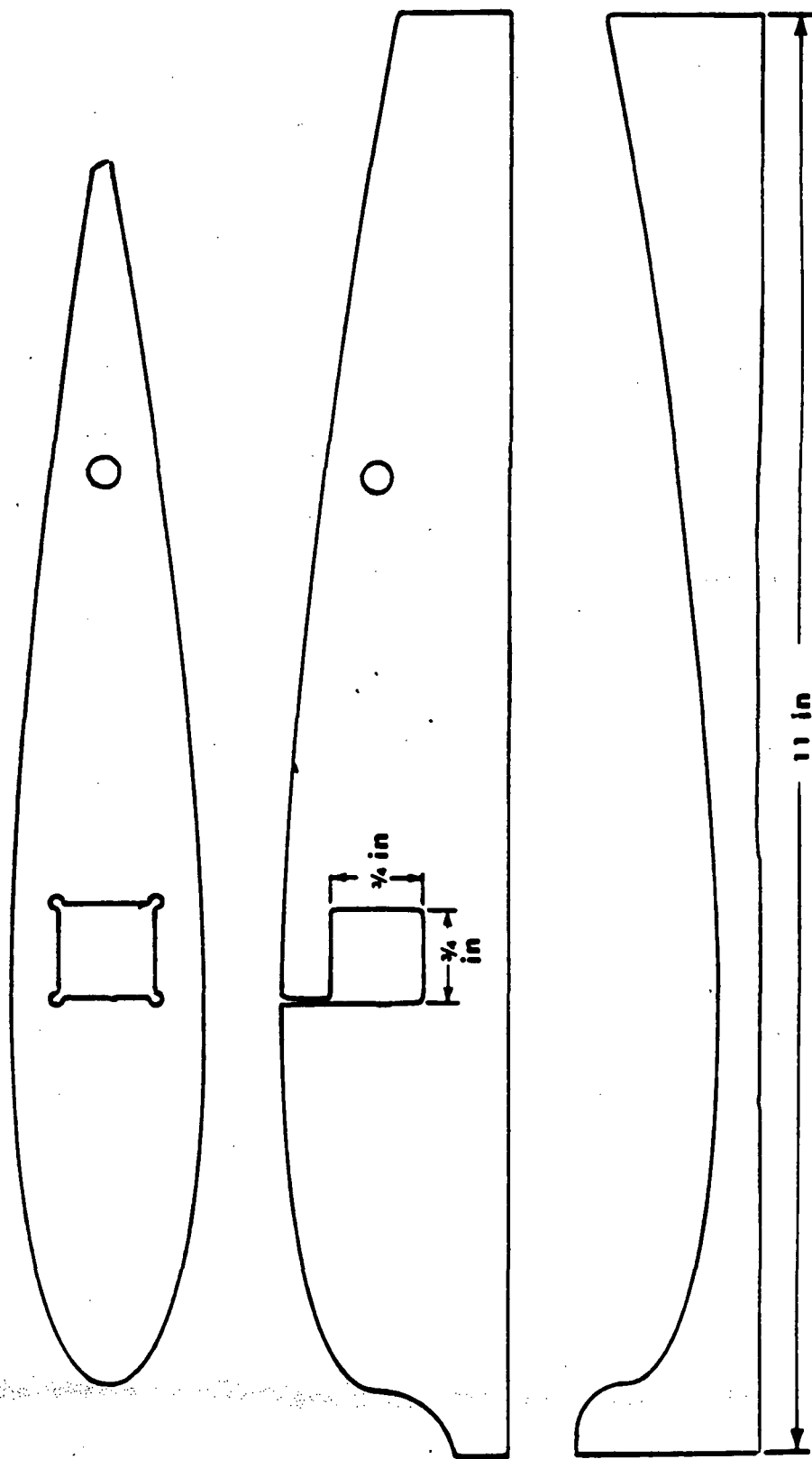


Fig. III-4 Templates for the NACA 0015 Wing Profile

Four layers of bidirectional weave fiberglass cloth and epoxy cover the core to provide structural rigidity and one layer of light weight fiberglass cover provides a smooth aerodynamic surface. Surface irregularities are removed by sanding and filling with quartz microspheres and resin.

The wing spar is initially a single piece of square aluminum tubing, 19.05 mm (0.75 in.) on a side and 3.175 mm (0.125 in.) thick, centered on the meanline at 35% of the chord behind the airfoil leading edge and extending out each wing tip to the external suspension. It is cut into two pieces to fit in a rectangular aluminum box which is constructed to mount an angular rate measuring device. The protruding ends on the box are fitted closely inside the cut spar tubing thus transmitting the structural loads across the wing, see Fig. III-5. Six accelerometers of two different sizes and sensitivities are installed inside of the airfoil for the "in-flight" estimation. They are mainly laid out in the middle of the wing section to maintain the symmetry of mass distribution, and fixed onto the surrounding styrofoam and one side of the fiberglass skin through epoxy and microsphere filler.

Circular endplates are fastened to each end of the airfoil, with a diameter a little bigger than the wing chord, machined from plexiglass 12.7 mm (0.5 in.) thick. A gap of 6.35 mm (0.25 in.) exists between each endplate and the wind tunnel wall to avoid boundary layer effects and maintain two-dimensional flow over the airfoil [26, p. 32]. Since both endplates move with the wing, they contribute significantly to the total apparent mass (10%) and moment of inertia (36%) of the system.

ORIGINAL PAGE IS
OF POOR QUALITY

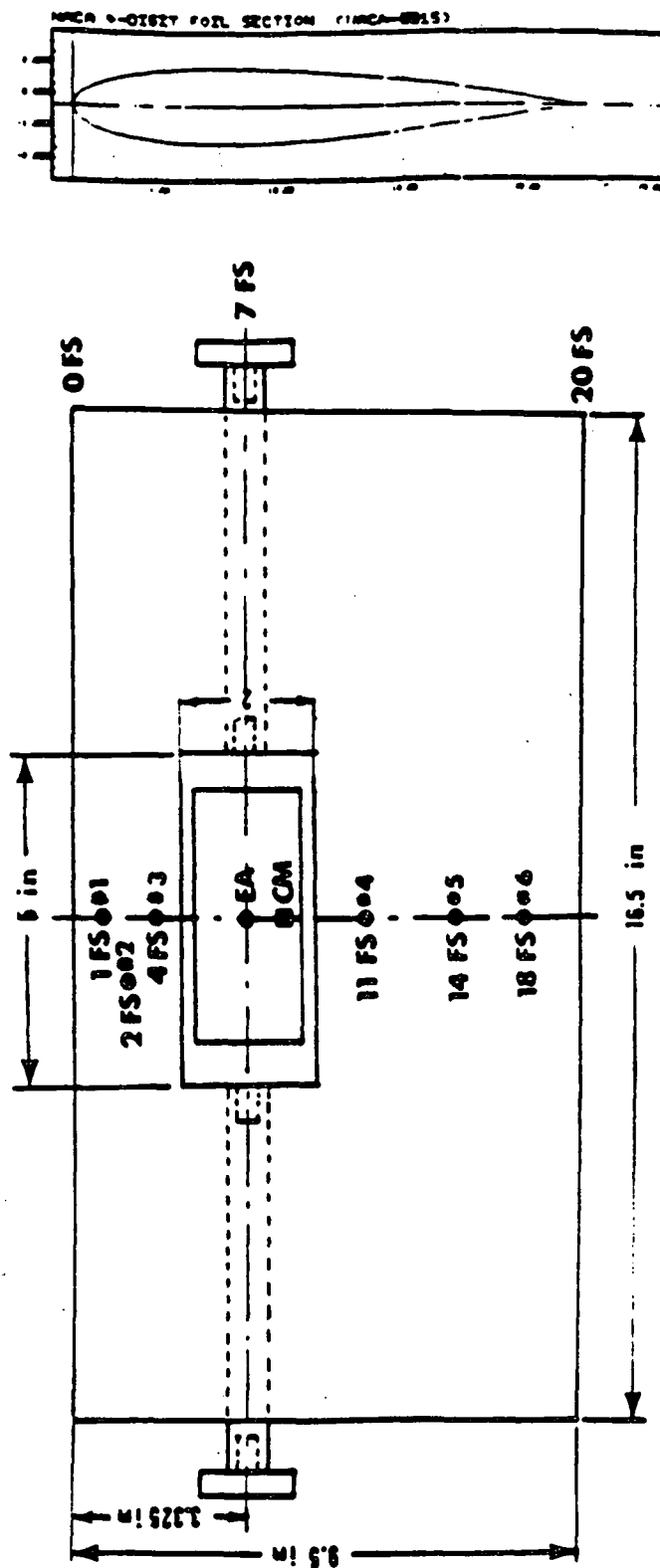


**Fig. III-5 NACA 0015 Model Wing Section Dimensions
and the Six Accelerometer Locations
(the 21 Flight Stations are 0.475 in. Apart)**

D. SUSPENSION SYSTEMS

The suspension system is designed to constrain the airfoil to move in the plunge and pitch DOF's without introducing any friction or elastic coupling into these motions. Hence, the suspension system employed can be treated statically as two independent systems -- one for plunge and one for pitch.

D-1 Plunge Suspension

The plunge suspension consists of four folded-cantilever springs mounted on the test section exterior, connected across the section top and bottom by light weight magnesium-aluminum cross beams. The cross beams are also connected along one vertical side of the test section by a third beam, as shown in Fig. III-2.

This arrangement constrains the airfoil to the plunge motion only (Fig. III-6, direction 2), and it is stiff in all the other directions. The only suspension losses are in the material flexural hysteresis and are very small. The plunge direction is designed to be horizontal rather than vertical to avoid the gravity bias.

The diagram of a single spring is given in Fig. III-7. It is stiff in directions 2, 3, and 4, but compliant in 5, 6, and 1, the desired direction. This spring can be analyzed as a group of four cantilever beams, two in parallel forming the center web, and two parallel split beams, each containing one half of both outside webs, which are in series with the central ones. The spring rate for displacement taken at the free end of a cantilever beam with the constraint condition of zero slope, is given by

$$K_s = \frac{12EI}{l^3}, \quad (3.1)$$

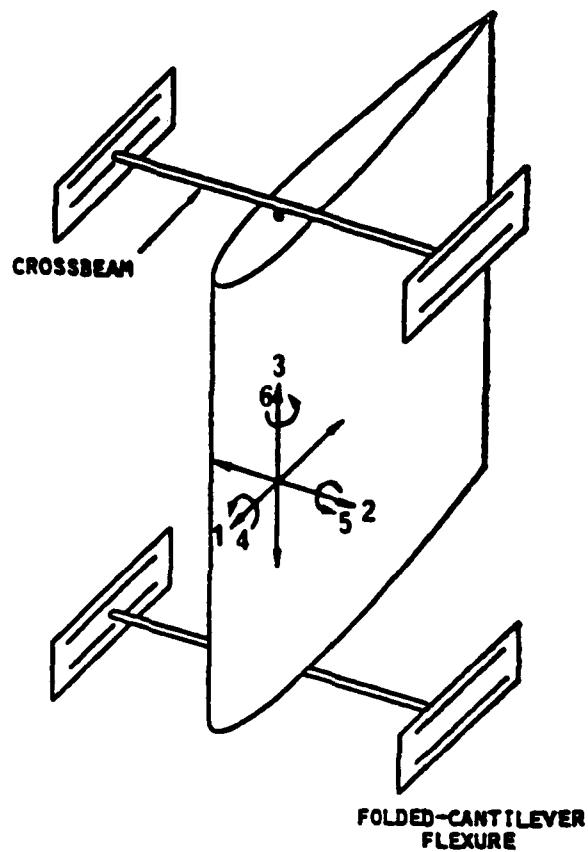


Fig. III-6 Arrangement of Plunge Suspension Springs and the Possible Degrees of Freedom of Motions

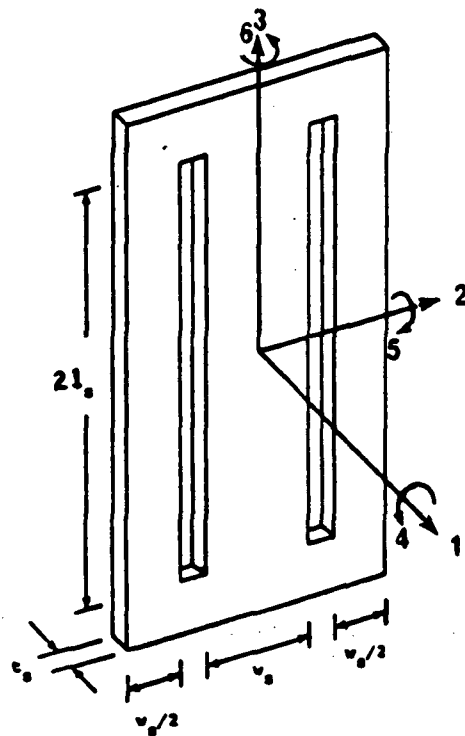


Fig. III-7 Folded Cantilever Spring

from elementary beam theory [58, p. 212], where $I = wt^3/12$. Since the four beams form a series-parallel set, the overall spring rate is the same as that of a single beam, given in Eq. (3.1).

Each spring was machined from Beryllium-Copper ($E = 1.28 \cdot 10^{11}$ N/m²) with $t = 1.68$ mm, $w = 28.6$ mm, and $l = 203$ mm. The resulting spring rate is

$$K_s = 2075 \text{ N/m}, \quad (3.2)$$

and the total spring rate along the plunge direction is

$$K_h = 4K_s = 8300 \text{ N/m}. \quad (3.3)$$

The measured spring rate of the actual system is 10383 N/m, 25% higher than its predicted value due to the uncertainties in the parameters E , l , w , but principally in t . The springs are offset by 10 mm to avoid snap-through at their zero position. Adjustable stops on the top and bottom cross beams allow the plunge travel to be restricted if necessary. They proved to be useful when operating in dynamically unstable situations. With the pitch DOF locked (see D-2), the total effective plunge mass and the structural damping in the plunge mode were experimentally determined by using an FFT analyzer, see Appendix C for details.

The vertical reinforcing beam shown in Fig. III-2 helps stiffen the suspension in the differential bending mode. The plunge actuator and plunge position sensor are located at the center of this beam. This location is chosen because it is at the node of the differential bending mode. Consequently, the actuator does not excite this mode and the sensor does not observe it either.

D-2 Pitch Suspension

The pitch suspension system is formed by torsional springs fastened between housings on the wing spar tips and the plunge cross beams as shown in Fig. III-8 for details. The springs are double cantilever Bendix flexural pivots, which allow elastically restrained pitch motion about the wing spar centerline. They are commercially available in a variety of spring rates and sizes. The bushings shown in Fig. III-8 allow the housings to accommodate different sized pivots. The spring rates for the plunge and pitch suspensions are designed or selected to allow the test system to have an adequate separation between those two major system modes and the desired flutter frequency. The two flexural pivots used have a measured combined spring rate of 43.04 N-m/rad. Adjustable stops are also provided for the pitch motion.

Since the mass of the plunge suspension is elastically decoupled from the pitch rotation, the actual mass of the system rotating about the pitch axis is considerably less than the total system mass M_T . The experimentally measured pitch mass M_2 , including the wing section and its endplates and part of the torque motor, is 2.075 kg. Its center is 0.0165 m behind the elastic axis thus yielding a value of $S_\alpha = M_2 x_\alpha = 0.04814$ kg-m.

The effective moment of inertia of the wing section and the pitch mode structural damping were experimentally determined by using an FFT analyzer, see Appendix C for details.

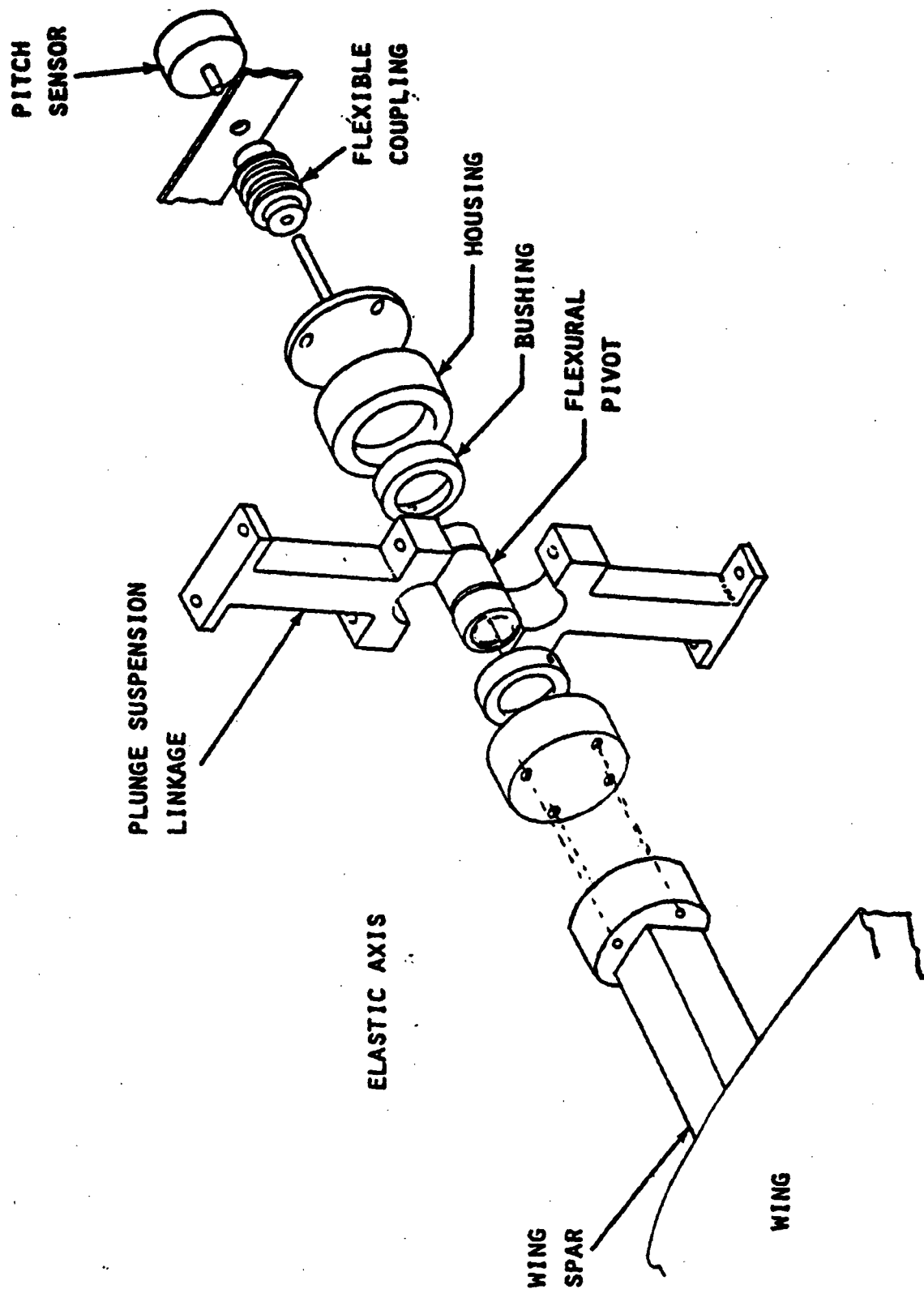


Fig. III-8 Exploded View of the Pitch Suspension System

E. ACTUATORS

Two actuators are used, one for each degree of freedom. They may be used independently or simultaneously to simulate the effect of an aerodynamic control surface.

E-1 Plunge Actuator

The plunge actuator is a linear motor (see Fig. III-9) of the type found in computer disc drives. It has a bandwidth of 65 Hz and is capable of 62 N ($11.7 V_{\text{input}}$) for short periods of time and 22 N ($4.15 V_{\text{input}}$) for continuous operation.

The voice coil current to force relationship is only linear within 5% but the repeatability (1%) is such that the motor can be easily compensated. The motor is driven by a current-drive amplifier to eliminate the back electromagnetic force (EMF) damping.

E-2 Pitch Actuator

The pitch actuator is an Aeroflex brushless torque motor shown in Fig. III-10. It is also driven by a current-drive amplifier. It has a bandwidth of 100 Hz and is capable of 2.12 N-m ($9.5 V_{\text{input}}$) for short periods of time and 1.06 N-m ($4.75 V_{\text{input}}$) for continuous operation.

The motor (2.27 kg) acts through the four-bar linkage shown in Fig. III-10 to reduce its apparent mass added to the airfoil by roughly 100:1.

ORIGINAL PAGE 10
OF POOR QUALITY

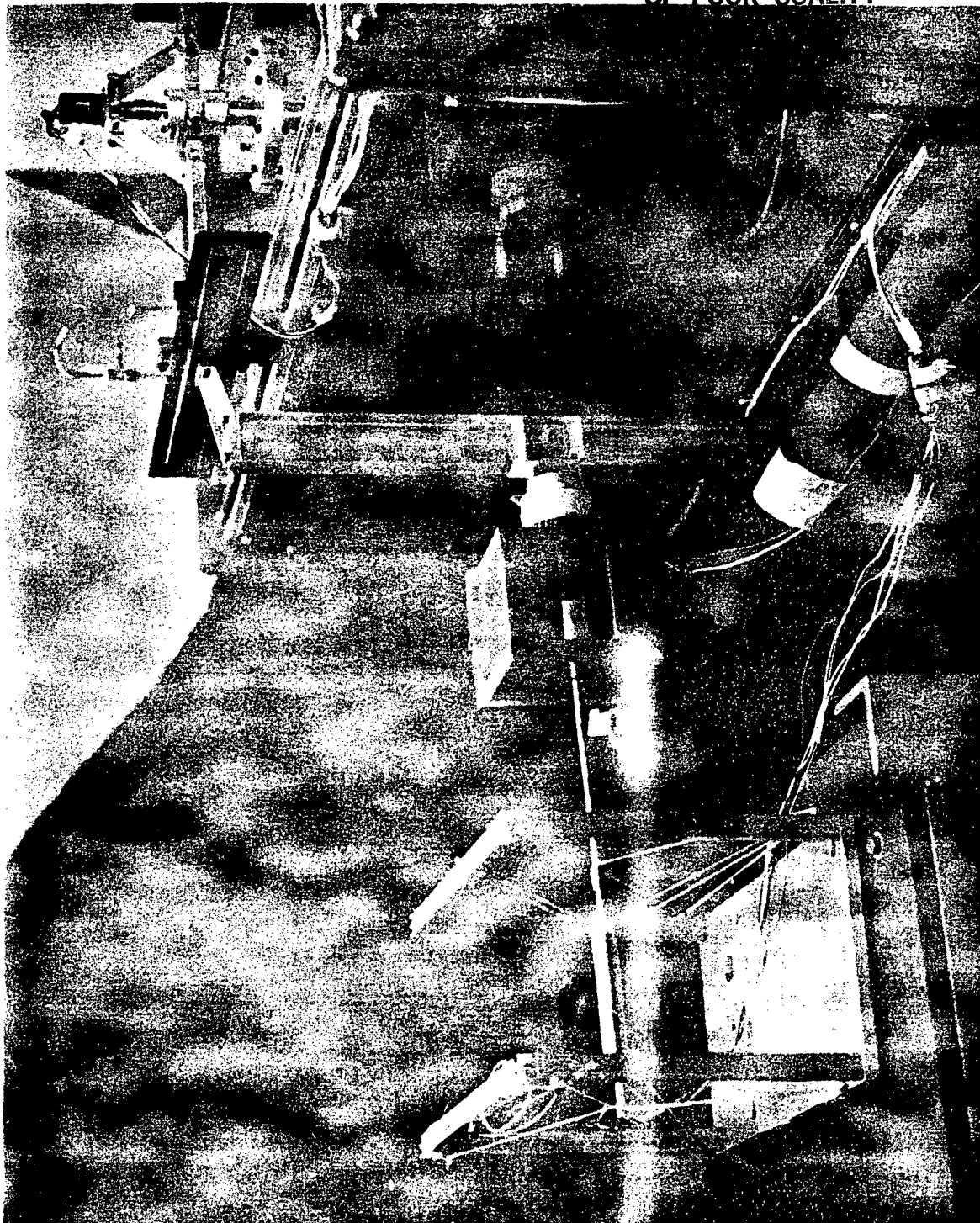


Fig. III-9 Linear Motor and LVDT with its Suspension

ORIGINAL PAGE IS
OF POOR QUALITY

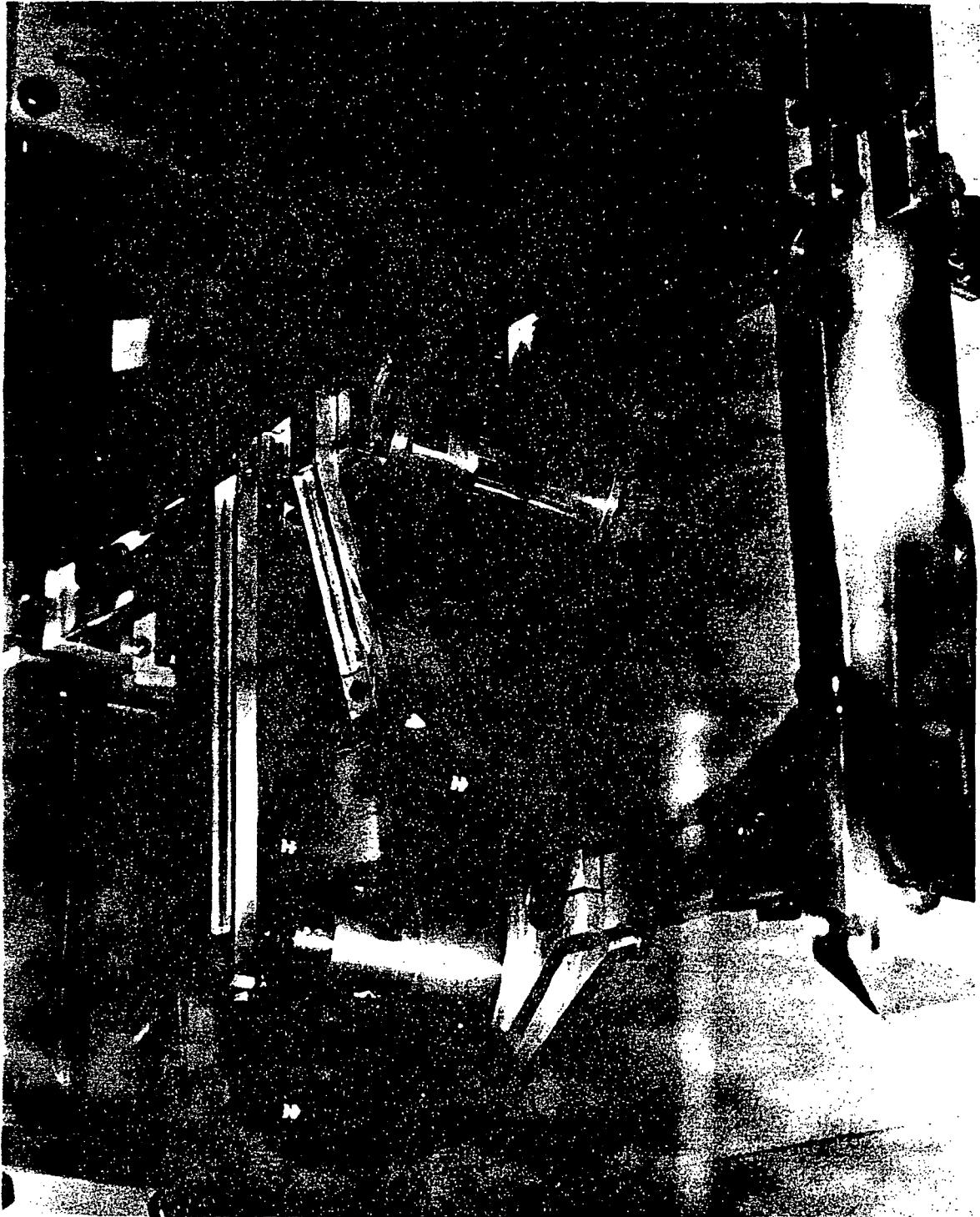


Fig. III-10 Torque Motor and Four-Bar Linkage

The operation of the linkage is explained with the aid of Fig. III-11. The elastic axis of the airfoil is constrained to move rectilinearly by the plunge suspension, Fig. III-11a. As the airfoil plunges, the linkage deflects without producing any torque (but it does produce an unbalanced force along the cross beam) about the elastic axis, Fig. III-11b. At any plunge position, however, the motor can transmit a torque through the linkage into the elastic axis, Fig. III-11c. All joints in the linkage are very compliant flex pivots. There are no bearings used in order to reduce the friction effects and maintain the repeatability of the system performance. Consequently, the only suspension losses are in the material flexural hysteresis and can be neglected.

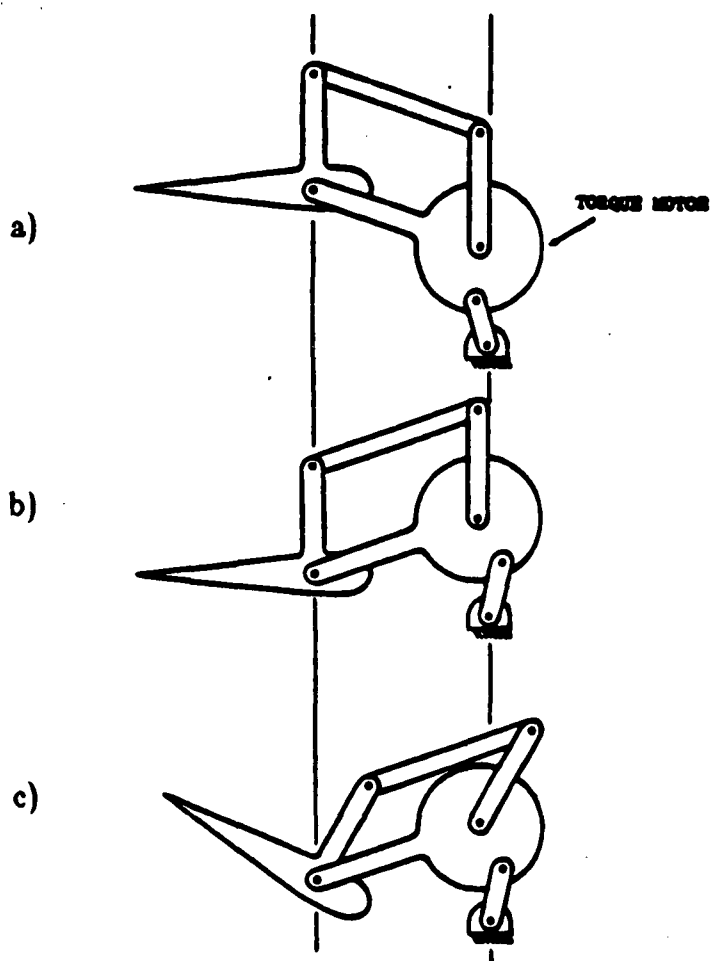


Fig. III-11 Operations of Four-Bar Linkage
a). Normal b). Translation c). Rotation

F. SENSORS

A monitoring sensor is provided for each degree of freedom. Six accelerometers inside the airfoil can be used in various combinations for the "in-flight" estimation. A pitot-static tube is provided for airspeed measurement.

F-1 Plunge Sensor

The plunge displacement transducer is a Schaevitz Engineering type 500 HR LVDT (linear variable differential transformer) which is excited with a 400 Hz signal, and when demodulated and filtered, produces an output voltage proportional to the plunge displacement. It is linear within 1% over the range ± 10 mm.

The sensor is isolated from motions of the wind tunnel walls and motions of the laboratory by suspending its case in an elastic suspension system (see Fig. III-9) with a natural frequency of about 2 Hz.

F-2 Pitch Sensor

The pitch angle sensor is a Kearfott type R235 -1-A resolver which is excited with a 400 Hz signal. It is linear within 1% over the range ± 5 degrees.

The resolver shaft is connected to the top flexural pivot housing using a flexible bellow coupling for protection. The resolver case is held by a bracket fixed to the top plunge suspension cross beam.

F-3 Linear Acceleration Sensors

Two different types of Piezoelectric Accelerometers, each with a different size and sensitivity, made by ENDEVCO are used -- model 2221D shear accelerometer weighs 12 gm with sensitivity 17 pC/g, and model 7701-100 isoshear accelerometer weighs 29 gm with sensitivity 100 pC/g.

Both types of accelerometers produce output charges proportional to the acceleration inputs. These outputs are converted by a model 2721B charge amplifier to voltage readings with a full scale (FS) ± 10 V.

F-4 Airspeed Sensor

Airspeed is measured with a United Sensor type PCD-8 KL pitot static tube connected to a gage-fluid filled manometer to read dynamic pressure in inches of water (a range of 0-8 in. or 0-2000 N/m²). The manometer is calibrated with 0.1 inches graduations (24.9 N/m²). The pitot tube is mounted approximately one half-chord ahead of the airfoil leading edge, and a similar distance above the test section centerline. This system has an accuracy of 1%. The ambient temperature and pressure are recorded at the wind tunnel for future conversion of the dynamic pressure to airspeed.

G. COMPUTER SYSTEMS

A DECLAB-23/MNC computer system is used for data acquisition and manipulation, monitoring and controlling of external apparatus. Its RT-11 operating system is a real-time, single-user operating system using FORTRAN IV programming language and PDP-11 assembly language. The Real-11/MNC software is designed for use with the RT-11 operating system to support the MNC-series hardware modules, which includes the real-time clock, digital input/output units, A/D and D/A converters, and a dual-multiplexer. The module function diagram is shown in Fig. III-12.

The A/D converter is a successive approximation type analog-to-digital converter with 12 bits resolution. Its full scale input range is ± 5.12 V bipolar with 40 μ sec typical data acquisition time. With its internal and the external dual-multiplexer it can sample up to 12 channels in quasi-differential mode.

There are 4 D/A converter channels with 12 bits resolution and output voltage ranges ± 2.56 V, ± 5.12 V, ± 10.24 V selected by users.

A Nicolet 660B dual-channel FFT analyzer is used for system identification; it facilitates the measuring of transfer function, damping ratio, spectrum distribution, and correlation function, etc.

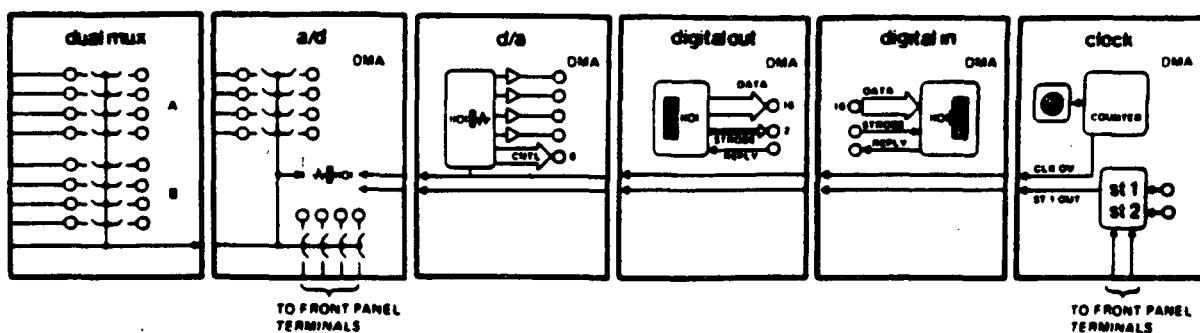


Fig. III-12 MNC-series Module Function Diagram

H. SYSTEM PARAMETERS

The definitions and experimentally measured values of the important physical parameters are summarized in Table III-1 along with error estimates. The procedures used to determine these values and error sources are detailed in Chapter IV and Appendix C.

Table III-1 Definition of Parameters

Definition of parameters				
Parameter	Definition	Experimental Value	Experimental Accuracy (%) (worst case)	Units
l	wing span	0.4191	0.5	m
c	wing chord	0.2413	0.8	m
b	semichord	0.1207	0.8	m
a	distance in semichord the EA lies aft of the MC	-0.3	0.8	-
M_2	wing mass	2.1	9.5	kg
M_1	suspension mass	3.395	4	kg
M_T	total mass	5.7	7.2	kg
K_2	mass ratio	0.3684	16.7	-
$I_\alpha = I_{\alpha T}$	total moment of inertia about the EA	0.01151	2.4	kg-m ²
K_h	plunge spring rate	10.38	1	kN/m
K_α	pitch spring rate	43.04	1	N-m/rad

* See explanation in Appendix C.

Table III-1 Definition of Parameters (cont)

ω_h	plunge modal frequency	6.65	0.7	Hz
ω_α	pitch modal frequency	10.05	0.7	Hz
ζ_h	plunge damping ratio	0.00448	-	-
ζ_α	pitch damping ratio	0.00932	-	-
\bar{x}_α	normalized distance the CM lies aft of the EA	0.19	11	-
S_α	dynamic coupling coefficient	0.04814	3.5	kg-m
\bar{r}_α^2	normalized squared radius of gyration	0.3767	11.2	-
K	moment of inertia ratio	0.9647	-	-
\bar{l}	normalized four linkage length	1.684	1.8	-
K_F	linear motor force constant	5.295	-	-
K_T	torque motor moment constant	0.2232	-	-
μ	mass ratio	246.0	10.3	-

I. APPARATUS PERFORMANCE

After a thorough investigation of the frequency response of the physical system by using the FFT analyzer, the overall performance of the system is sure to behave very closely to the ideal two DOF typical section shown in Fig. III-1. By comparing with the analytical transfer functions obtained in Fig. A-1, Section B-1, Appendix A, it can be seen that Figs. III-13 to III-16 truly describe them well in terms of the pole-zero locations. However, two complicating characteristics exist because of the four-bar linkage used with the torque motor and the excitation of differential modes.

I-1 Unbalanced Force Problem

Torque is transmitted to the elastic axis of the airfoil as described in Section E-2. However, the application of a torque generates an unbalanced force in the plunge DOF which is 180 degree out of phase with the linear motor force. This is explained with the aid of Fig. III-17. Although this force has been taken into account in the system modeling, it may still excite the differential plunge mode as shown in Fig. III-18.

I-2 Differential Modes Problem

The plunge differential mode discussed above which exists due to the arrangement of the plunge suspension and asymmetry of the system structure. Its existence can be easily removed by adjusting the mass center of the plunge DOF; also, it is not quite observable by the plunge position sensor in our system configuration. However, if the amplitude of this differential motion got large enough, it could cause binding of the plunge actuator, although this has not occurred so far.

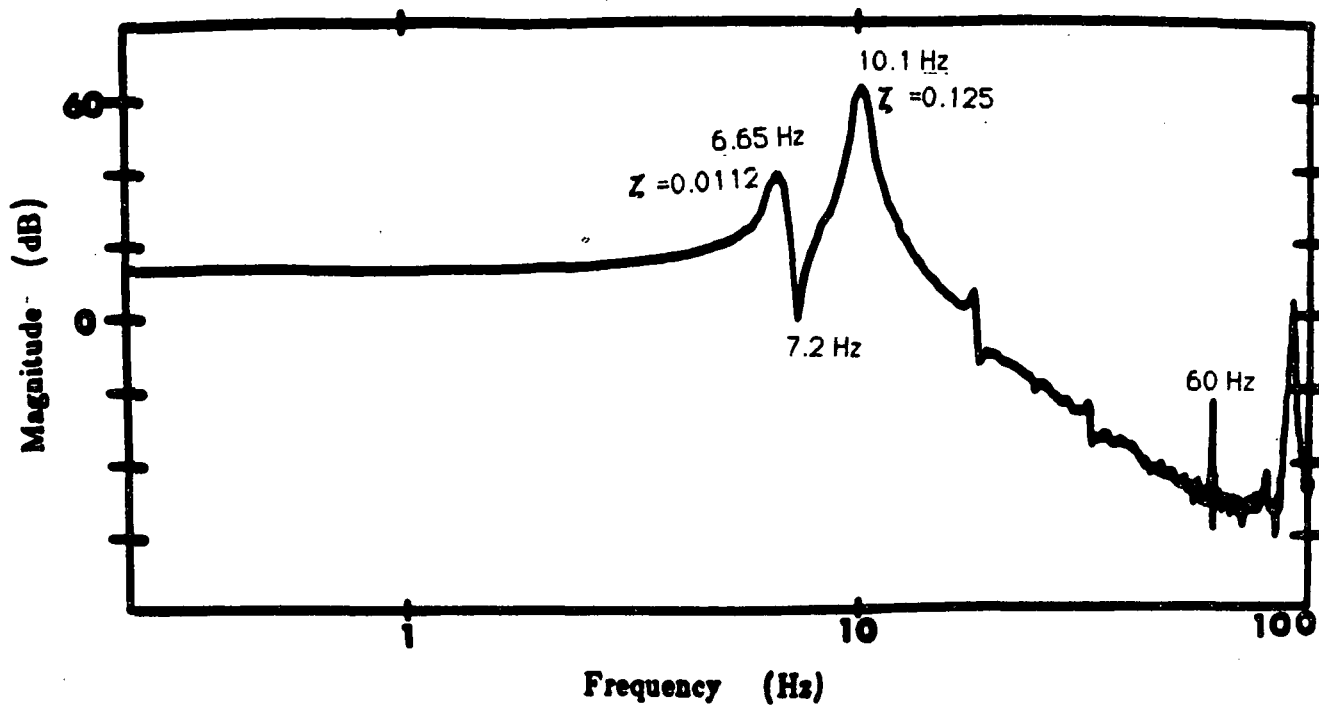


Fig. III-13 Magnitude of Transfer Function of h/F

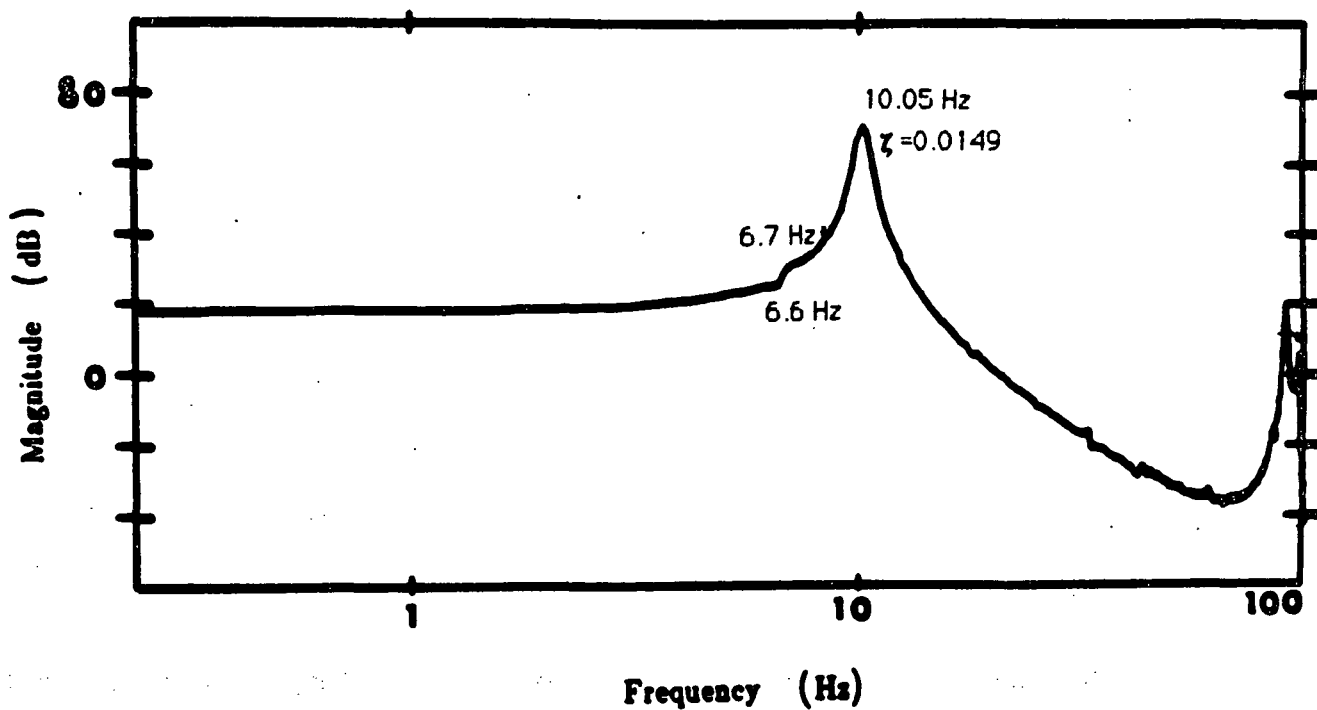


Fig. III-14 Magnitude of Transfer Function of α/F

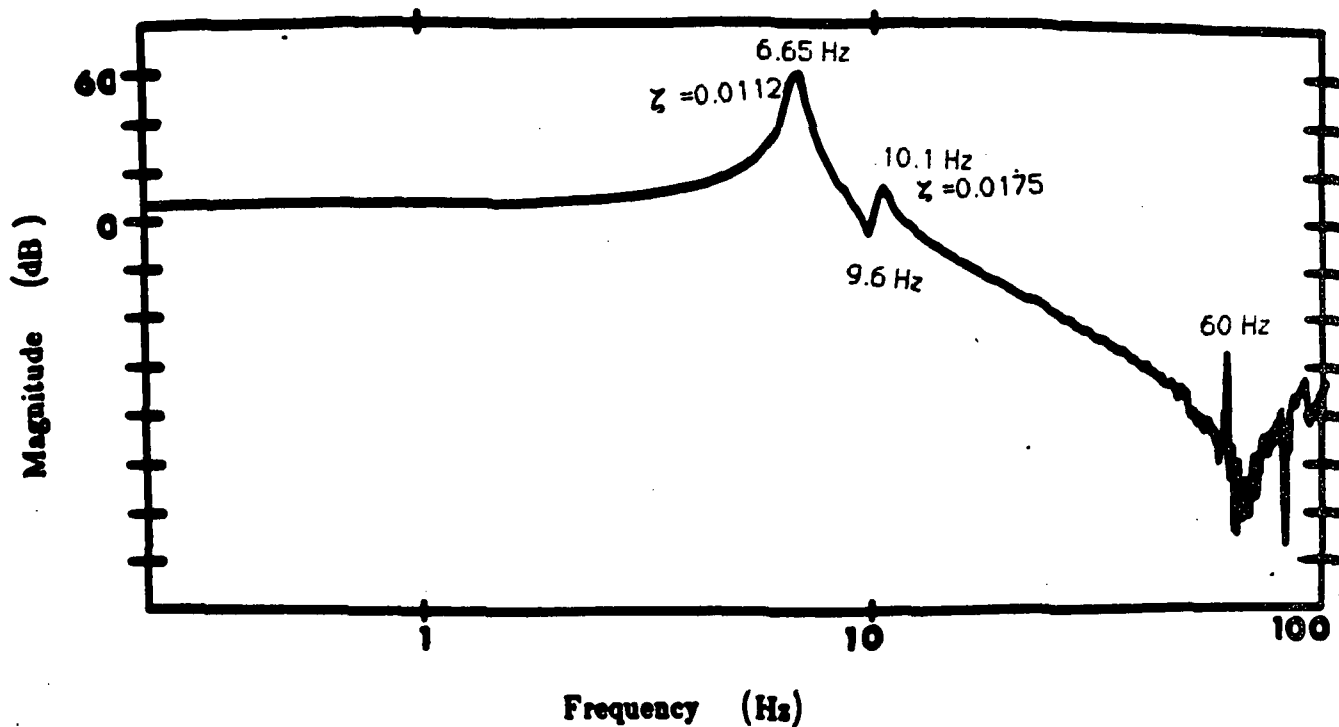


Fig. III-15 Magnitude of Transfer Function of a/T

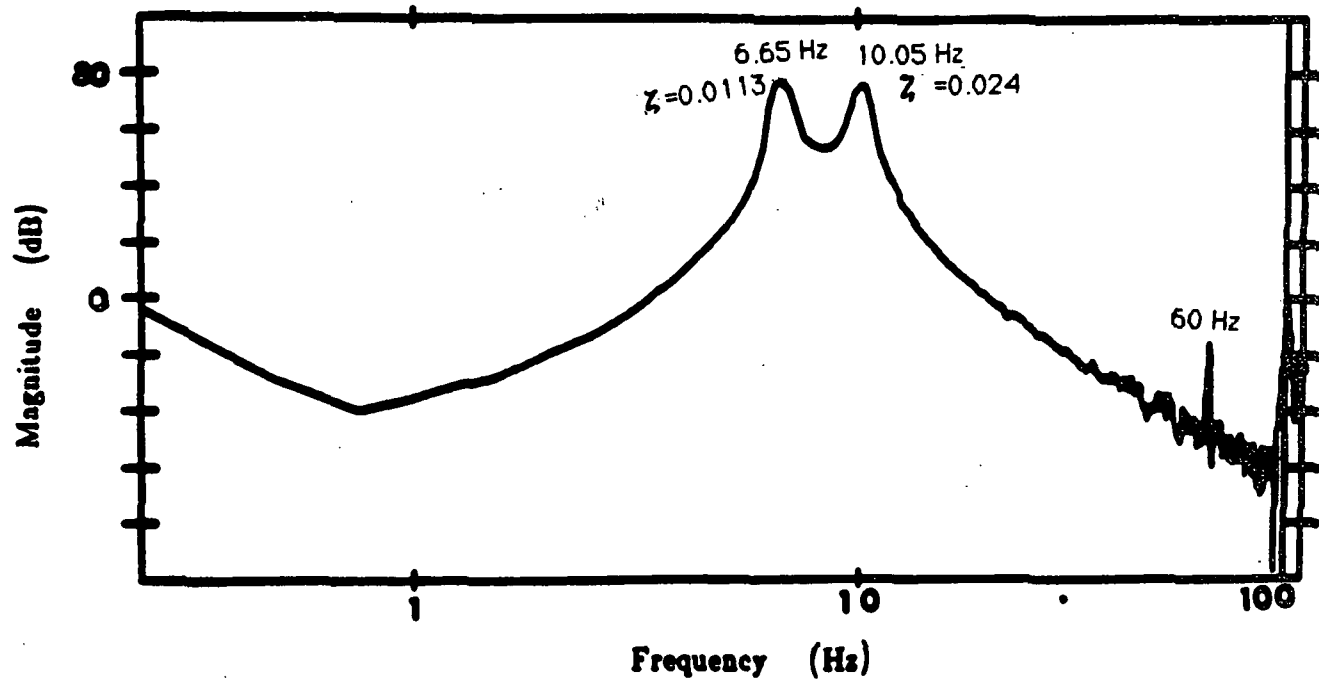


Fig. III-16 Magnitude of Transfer Function of h/T

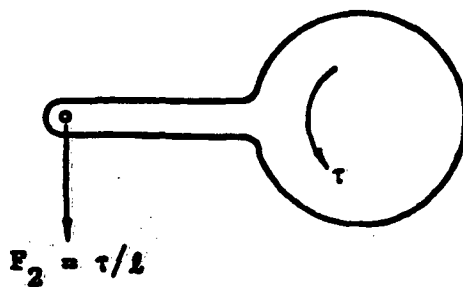
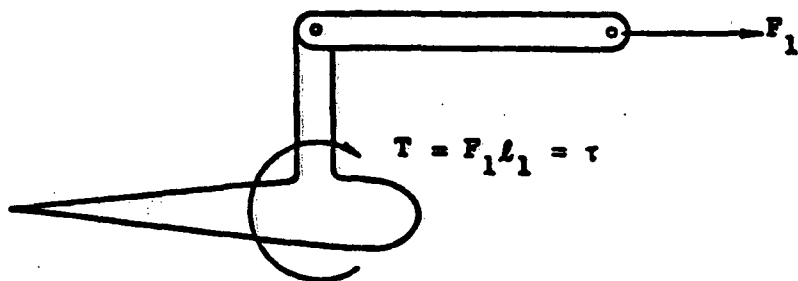
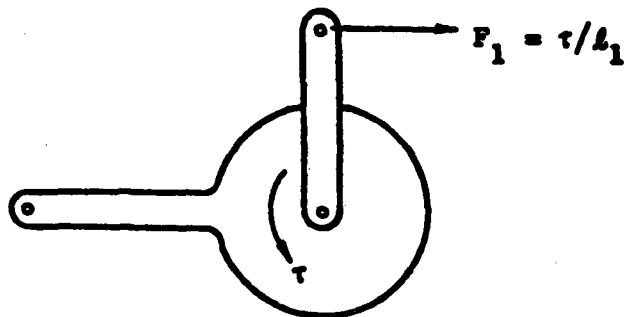
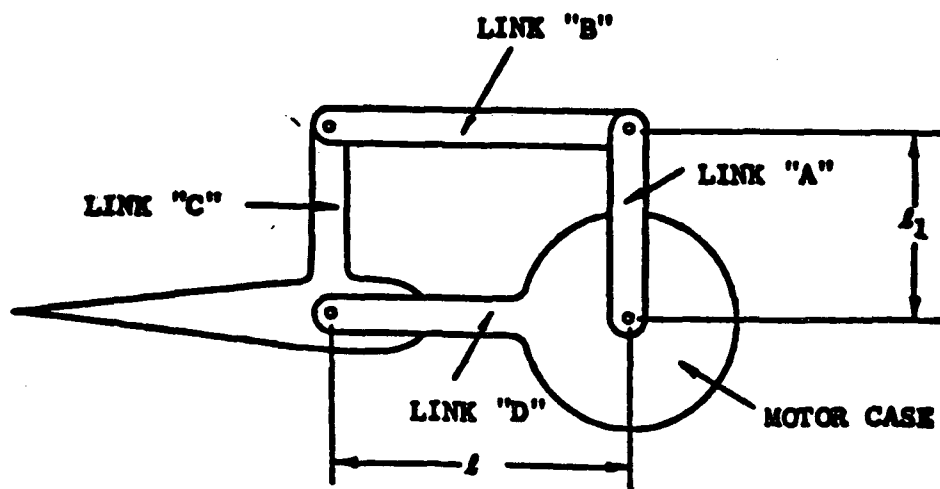
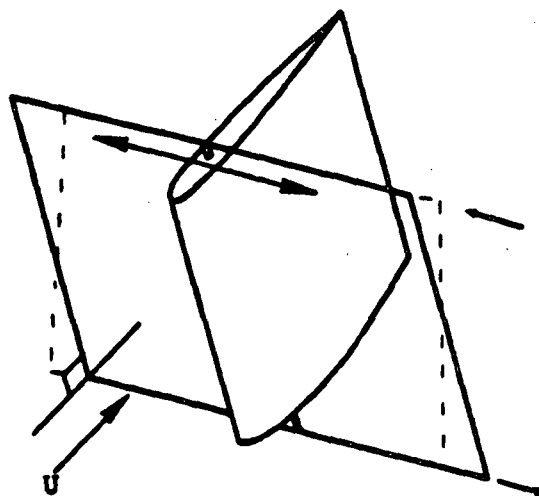


Fig. III-17 Unbalanced Reaction Force in Plunge Direction Due to the Applied Torque

(a) DIFFERENTIAL
PLUNGE MOTION



(b) DIFFERENTIAL
PITCH MOTION

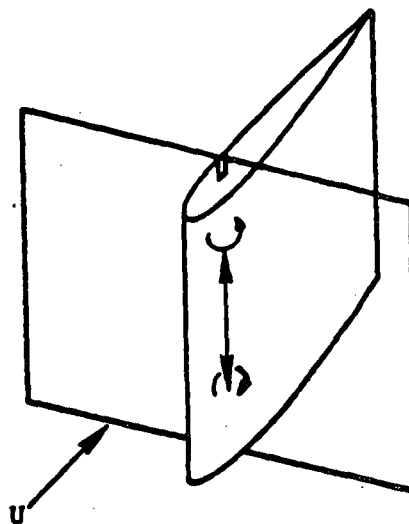


Fig. III-18 Differential Plunge and Pitch Motions

The pitch differential twisting of the wing across its span exists due to the flexibility of the wing spar and the application of torque to only one end of the wing as shown in Fig. A-2. It can also be observed in Figs. III-15 and III-16 at about 90 Hz. Since it is much faster (9:1) than the primary system dynamics, it can be ignored without too much influence upon our investigation.

Both differential modes are antisymmetric and thus do not affect the aerodynamics. Since in closed loop studies, it is theoretically possible to drive the differential modes unstable, they must be examined closely at that time [26, p. 83].

Chapter IV

EXPERIMENTAL METHODS AND RESULTS

A. INTRODUCTION

This chapter describes the experimental methods and compares the experimental results with the theoretical predictions.

B. MEASUREMENT OF SYSTEM PARAMETERS

A Nicolet 660B dual-channel FFT (fast Fourier transformation) analyzer was used for most of our system parameter identifications. It performs the hardware fast Fourier transformations on both input channels, from which a lot of functional relationships between these two channels can be obtained. For instance, the transfer function between an input and an output of a physical system can be easily obtained by simply plugging its input to channel A and its output to channel B. The definition of the functions that the FFT analyzer can analyze is given in Table IV-1.

With the help of the clamps on both of the plunge and the pitch suspension systems, the airfoil can be constrained to move in either single degree of freedom (DOF) independently. The FFT analyzer was first used to investigate the transfer functions for these single DOF motions. The problems discussed in the apparatus performance of Chapter III were noticed at this stage. The system structural parameters were found by looking at those transfer functions with a light square aluminum bar installed in place of the airfoil section.

Table IV-1 Definition of Functions for FFT Analyzer

FUNCTION	DEFINITION
instantaneous time history	$A(t)$
instantaneous FFT	$S_A = F \{ A(t) \}$ $= \lim_{T \rightarrow \infty} \int_{-T}^T A(t) e^{-j\omega t} dt$
average power spectrum	$G_{AA} = \overline{S_A \cdot S_A^*}$ $= \overline{S_A} ^2$
average cross spectrum	$G_{AB} = \overline{S_B \cdot S_A^*}$
transfer function	$H_{AB} = \frac{G_{AB}}{G_{AA}} = \frac{\overline{S_B \cdot S_A^*}}{\overline{S_A \cdot S_A^*}}$
impulse response	$IR = F^{-1} \{ H_{AB} \}$
transmissibility	$H_{AB} = \frac{G_{BB}}{G_{AA}} = \frac{\overline{S_B \cdot S_B^*}}{\overline{S_A \cdot S_A^*}}$

Table IV-1 Definition of Functions for FFT Analyzer (cont)

coherent output power	$COP = \frac{G_{AB} \cdot G_{AB}^*}{G_{AA}}$ $= \gamma_{AB}^2 G_{BB}$
coherence	$\gamma_{AB}^2 = \frac{G_{AB} \cdot G_{AB}^*}{G_{AA} \cdot G_{BB}}$ $= \frac{ G_{AB} ^2}{G_{AA} \cdot G_{BB}}$
auto-corr. function	$R_{AA}(\tau) = F^{-1} \{ G_{AA} \}$ $= \lim_{T \rightarrow \infty} \frac{1}{2T} \int_{-T}^T A(t)A(t+\tau) dt$
cross-corr. function	$R_{AB}(\tau) = F^{-1} \{ G_{AB} \}$ $= \lim_{T \rightarrow \infty} \frac{1}{2T} \int_{-T}^T A(t)B(t+\tau) dt$

Some of the parameters of the airfoil section itself were measured easily outside of the wind tunnel section, such as its mass, dimensions, etc. The available data were used to fit the second order clamped single DOF system models in order to compute those parameters not easily measured, such as the moment of inertia of the airfoil, etc. Redundant data were sometimes available for cross checkings. The system parameters measurements and identification are described in Appendix C with greater details.

After all the necessary system parameters were measured or identified, they were used in the complete two DOF system model to describe the full system behavior.

C. ACCURACY OF SYSTEM MODELING

The mathematical system model was derived in Appendix A. It incorporated the unsteady aerodynamics modeling for the 2-dimensional wind tunnel airfoil developed by Rock. In his thesis, he found that as H/b decreases, fewer poles are needed to be retained to describe accurately the Timman's **modified Theodorsen function**, i.e. $Q_T(s, \lambda)$. If $H/b \leq 2$, the residue of the first pole represents roughly 98% of this function's impulse response. Consequently, he introduced and proved that the approximation

$$G \frac{s+z}{s+p} \tag{4.1}$$

describes $Q_T(s, \lambda)$ accurately throughout the entire s -plane for $H/b \leq 2$, where p is a function of H/b .

From Fig. IV-1, the Nyquist plot of Eq. (4.1) in s/p plane, we can see it is a semicircle with center at $G+G(z/p-1)/2$ and radius $G(z/p-1)/2$ [Refs. 59-60]. The values of G and z/p determines the location and size of this semicircle.

Playing with the values, we have found a better fit of the theoretical root-locus to the experimental one than that found by Rock. Rock chose $G = 0.5$ and $z/p = 2.0$ to preserve the d-c and high frequency gains (1.0 and 0.5 respectively). Their old and new values are given in Table IV-2.

A 5th order system model was established to describe the plunge, pitch and aerodynamics behavior of the physical system. The resulting modes are named by their dominant components for ease of reference. In this model, the unbalanced force due to the applied torque mentioned in Chapter III-I was modeled into the control distribution matrix G . The damping coefficients were measured by the FFT analyzer and added to the modeling. Also the dynamical coupling between the plunge and pitch mode was actually computed through the offset of the mass center (CM) from the elastic axis (EA) rather than using a rough 2nd order experimental fit to find the value of the coupling. It is upon the center of mass of the wing instead of the center of mass of the whole plunge structure that the aerodynamics has influence anyway. These proved to be useful to increase the system modeling accuracy.

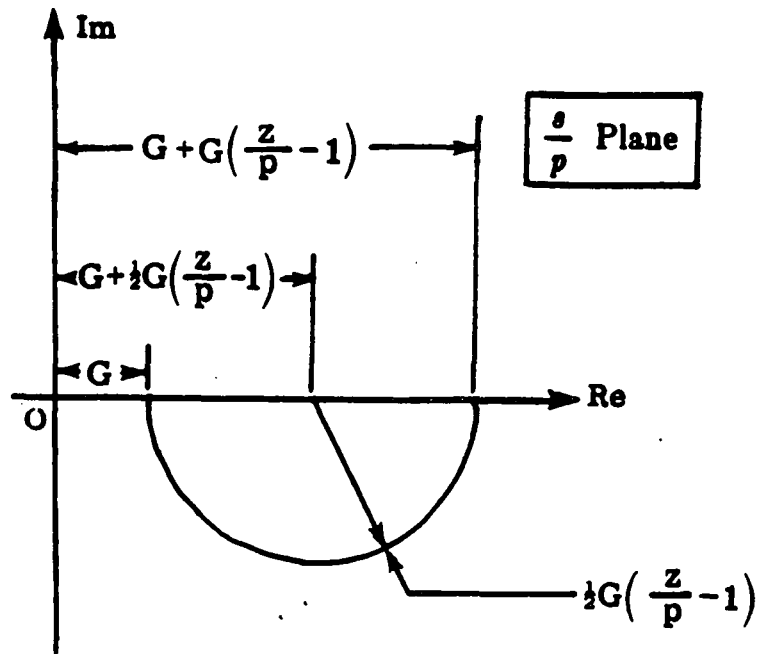


Fig. IV-1 Nyquist Plot of $G(\frac{s+z}{s+p})$ in $\frac{s}{p}$ Plane

Table IV-2 Old and New Values

	old value	new value
p	0.27 Hz	0.43 Hz
G	0.5	0.47
$\frac{z}{p}$	2.	2

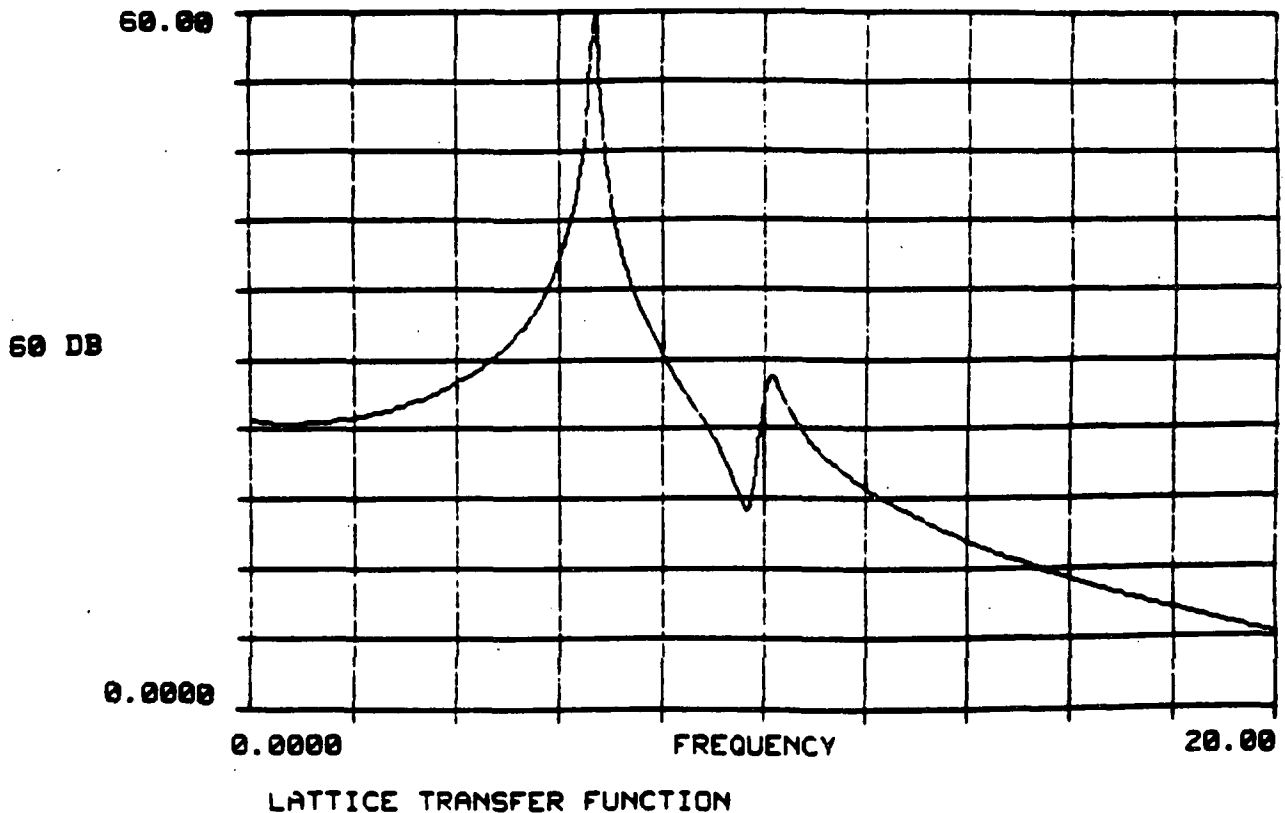
A laboratory test instrument, Genrad 2515 structural analyzer, was used to check the validity of the system modeling. It gathered a batch of data and then used a lattice filter for adaptive processing [61] to fit a specified order linear transfer function to the raw data. Figure IV-2 shows a typical output which identifies the system eigenvalues directly.

After repeating the procedure at various wind speeds, those test results could be compared with the theoretical predictions by examining the pole-zero loci of their transfer functions. Figure IV-3 shows both the experimental and the theoretical open-loop system root locus versus various wind speeds. Note that they agree within 1% in frequencies for the worst case before fluttering. This result is considered to be better than Rock's 2% error.

It was proven by Rock that a doublet input to the plunge actuator can be used to excite both the plunge and the pitch structural modes of the system. Actually, a positive voltage (2 volts) was applied to the linear motor for 10 ms followed a negative voltage of the same amplitude and duration. This same input was used to drive the mathematical model in computer simulations. The actual and computer-simulated system responses could be compared in a real time manner. Figure IV-4 shows the setup for the real time comparison.

From Fig. IV-5 to Fig. IV-8, the simulated responses from the computer's digital to analog (D/A) converters were compared with the actual system responses. The agreement can be seen excellent for lower wind speeds. However, there is a 1% difference in frequency for the worst case before fluttering shows up at a wind speed of about 27 m/sec in Fig. IV-8.

ORIGINAL PAGE IS
OF POOR QUALITY



T=2047 XL=0.9900 EST ORDER: 12
CENTER FREQ= 0.00 BANDWIDTH= 20.00

P(Z) zeroes

Q(Z) poles

real	imag	real	imag	freq. (hz)
-2.273E+00	0.000E-01	-2.130E+00	0.000E-01	0.000E+00
-1.242E+00	6.097E+01	-2.882E-01	4.187E+01	6.663E+00
-1.242E+00	-6.097E+01	-2.882E-01	-4.187E+01	-6.663E+00
-6.476E+01	6.441E+01	-5.596E+01	5.789E+01	9.214E+00
-6.476E+01	-6.441E+01	-5.596E+01	-5.789E+01	-9.214E+00
-1.474E+03	1.005E+02	-1.336E+00	6.311E+01	1.004E+01
-6.737E+00	-1.246E+02	-1.336E+00	-6.311E+01	-1.004E+01
-6.737E+00	1.246E+02	-6.797E+00	1.246E+02	1.982E+01
-2.454E+01	-1.704E+02	-6.797E+00	-1.246E+02	-1.982E+01
-2.454E+01	1.704E+02	-2.932E+01	1.729E+02	2.752E+01
-1.026E+01	2.011E+02	-2.932E+01	-1.729E+02	-2.752E+01
-1.470E+02	2.011E+02	-2.651E+01	2.011E+02	3.200E+01

Fig. IV-2 Typical Output of the Genrad 2515 Structural Analyzer

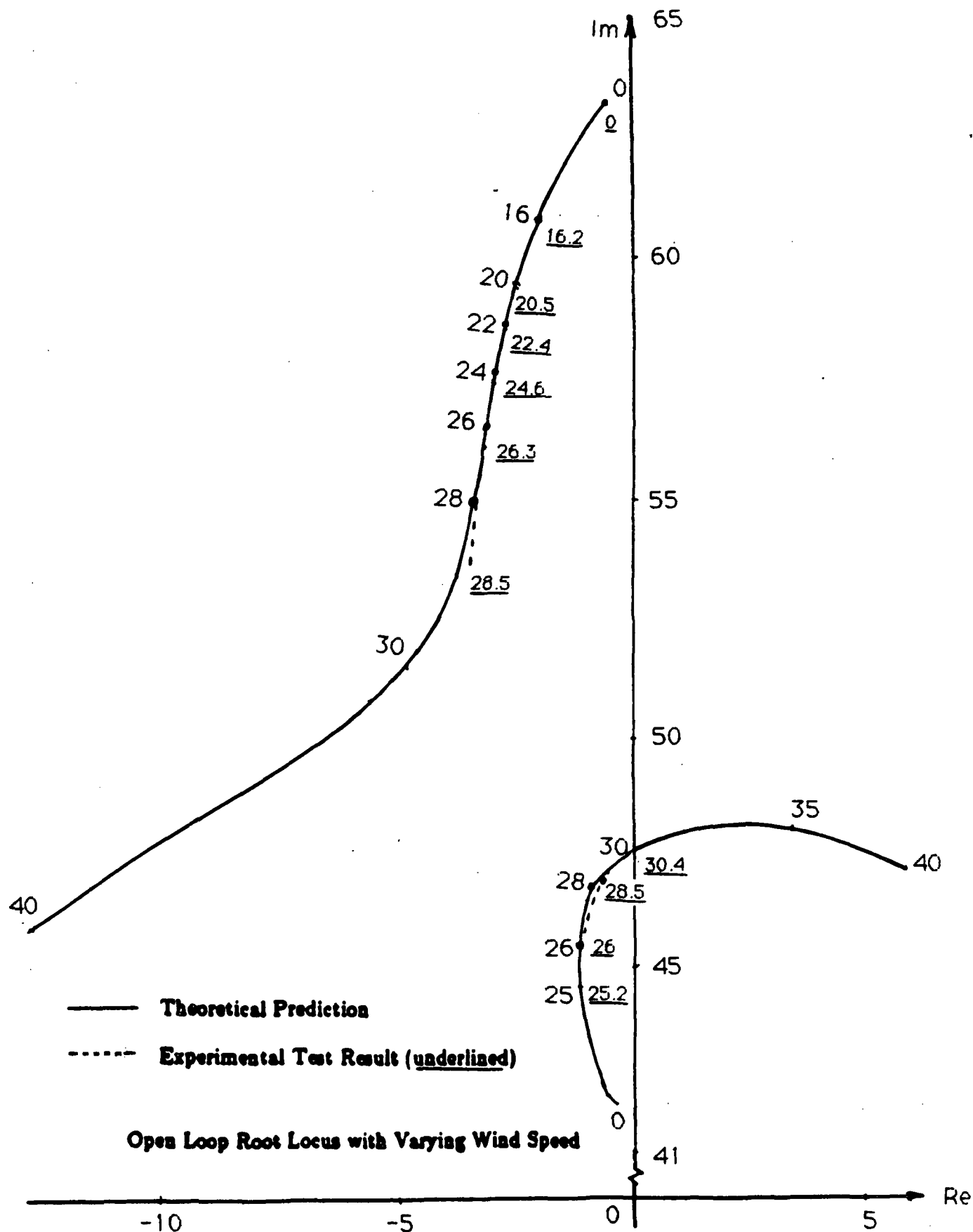


Fig. IV-3 Open Loop Root Locus with Various Wind Speeds

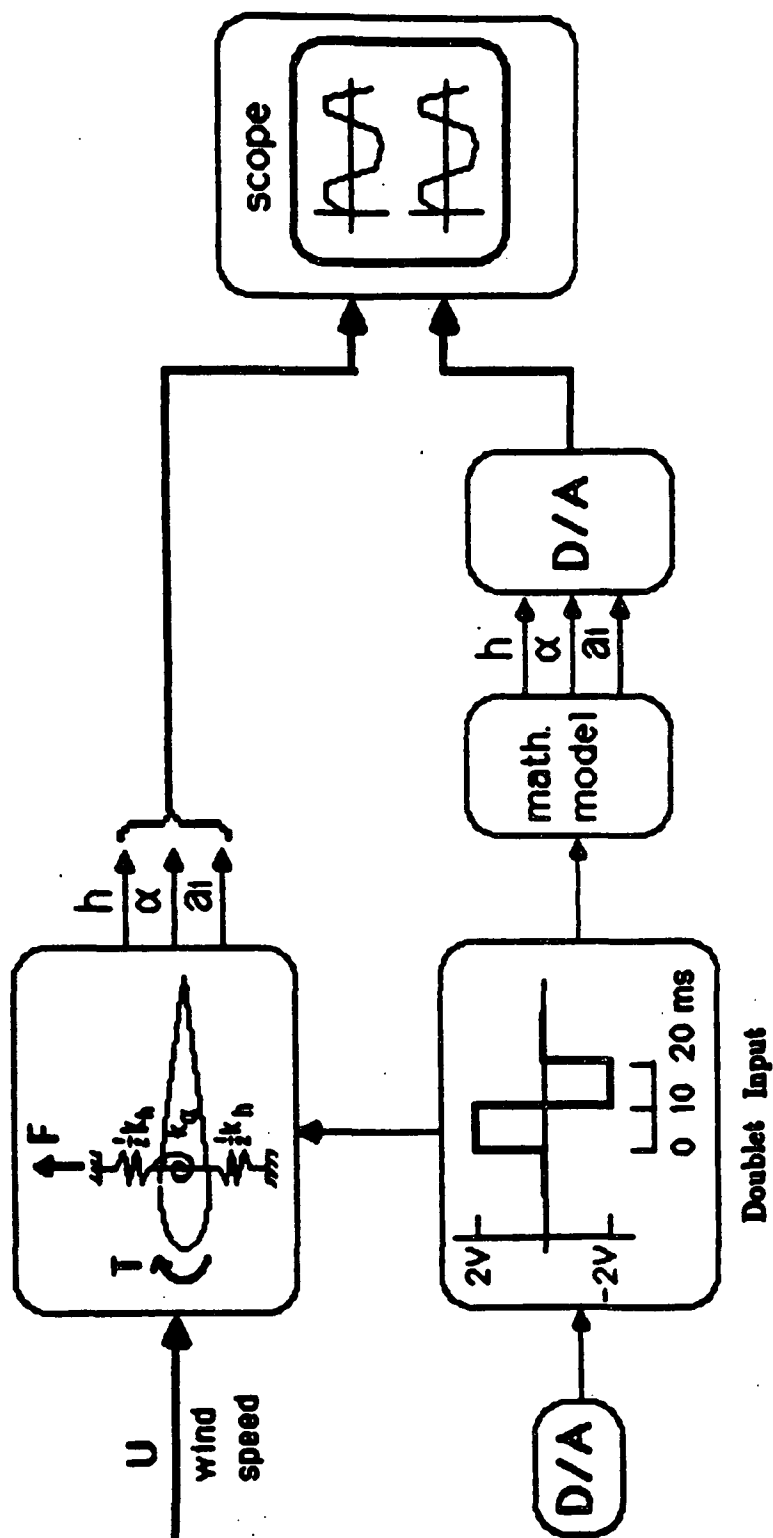
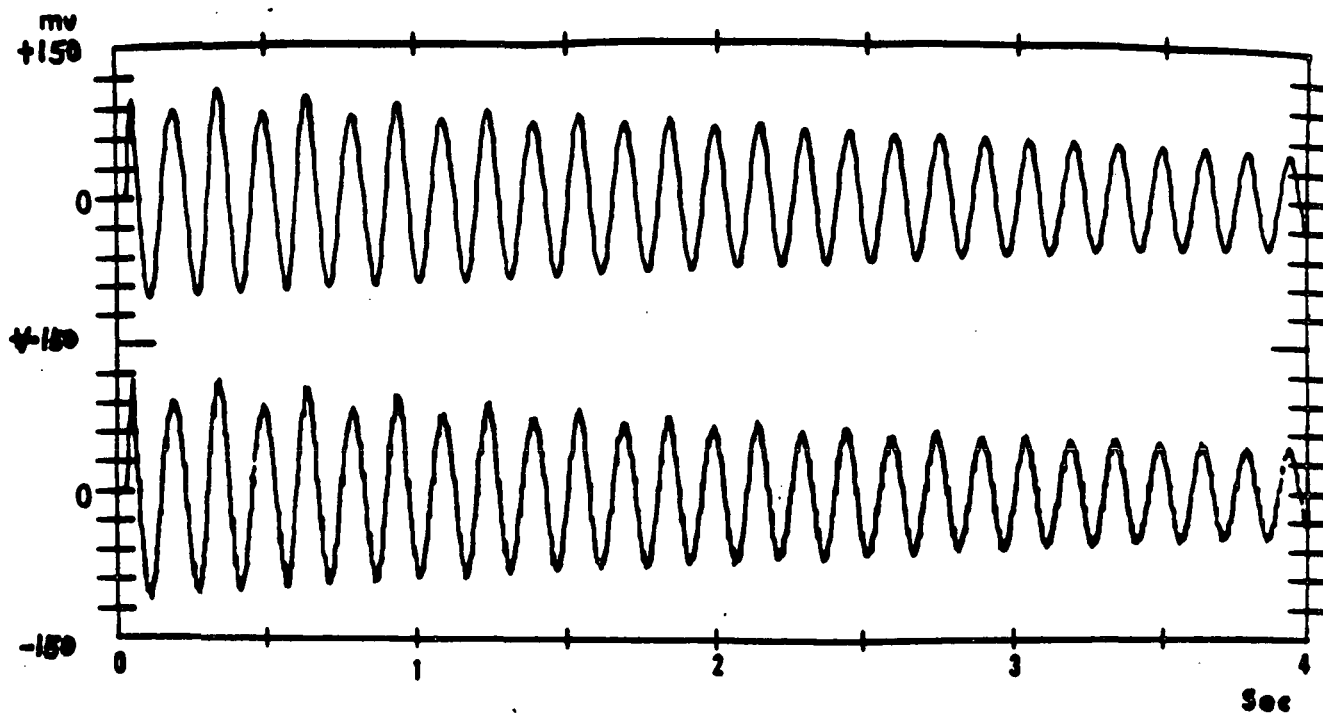


Fig. IV-4 Setup for the Real Time Comparison



**Fig. IV-5a Actual and Simulated Plunge Responses to
A Linear Doublet Input at Wind Speed $U = 0$ m/sec**

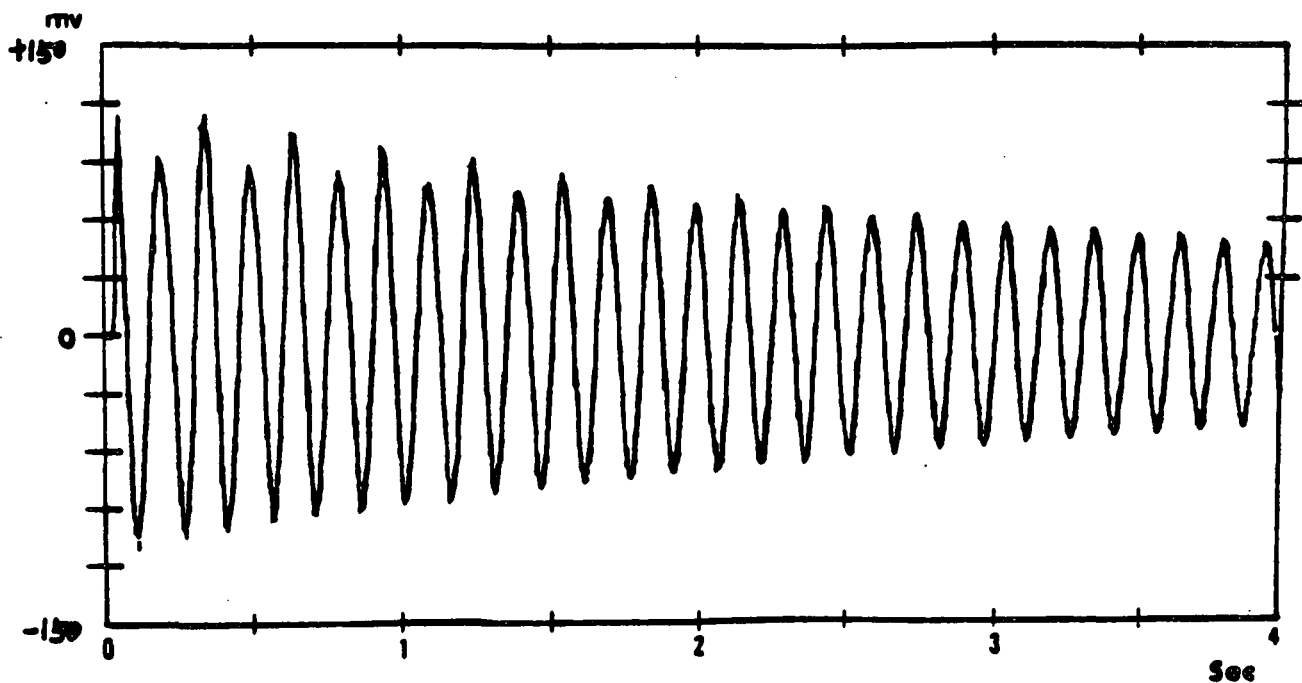
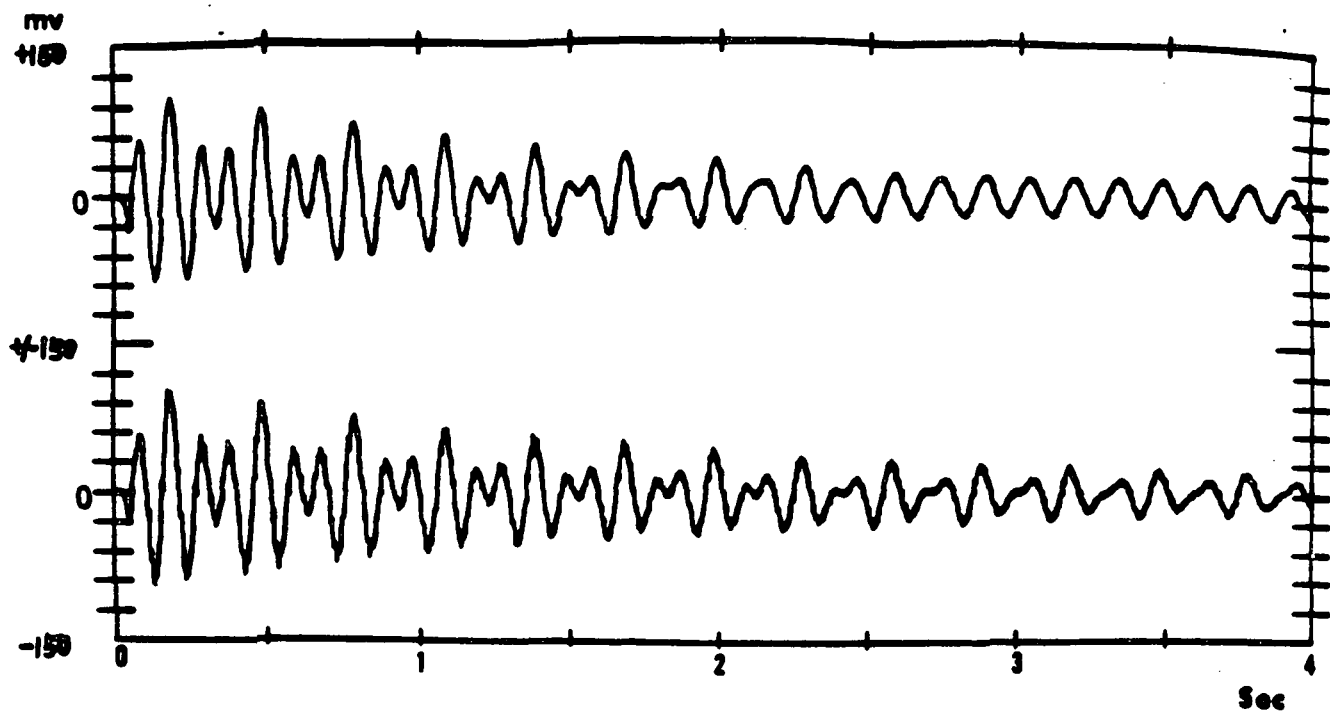


Fig. IV-5b Overlapped Plot



**Fig. IV-6a Actual and Simulated Pitch Responses to
A Linear Doublet Input at Wind Speed $U = 0$ m/sec**

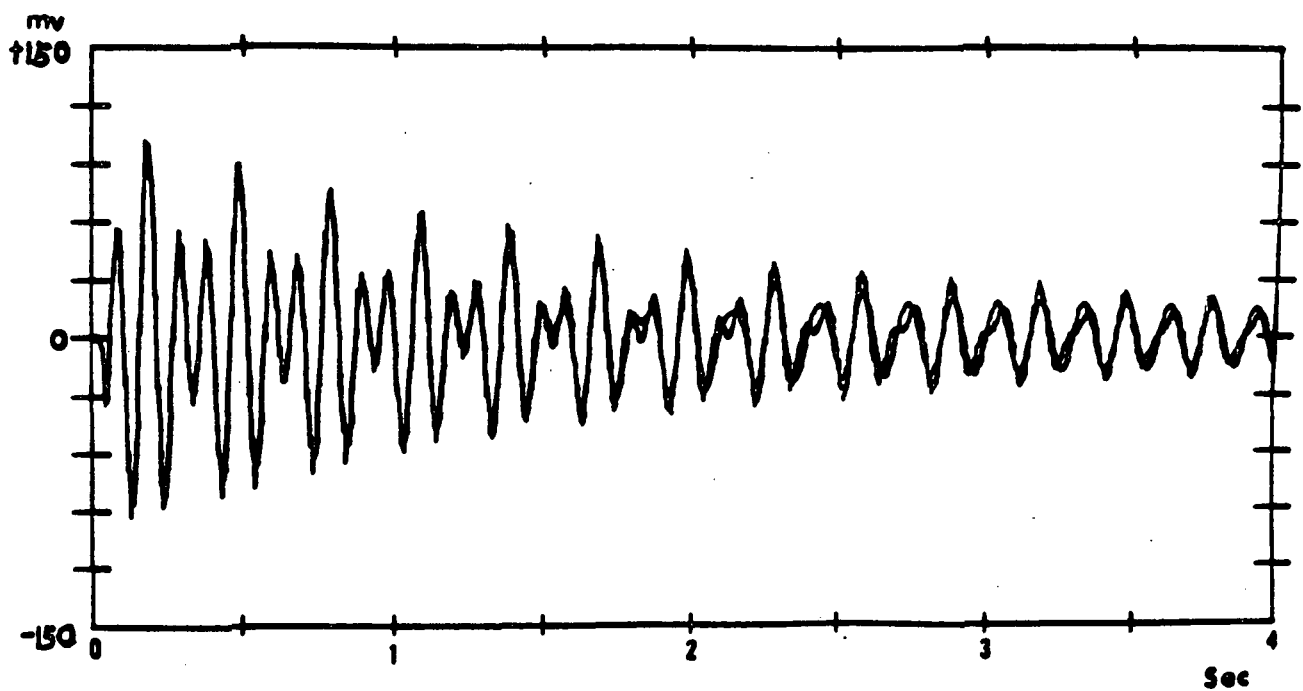
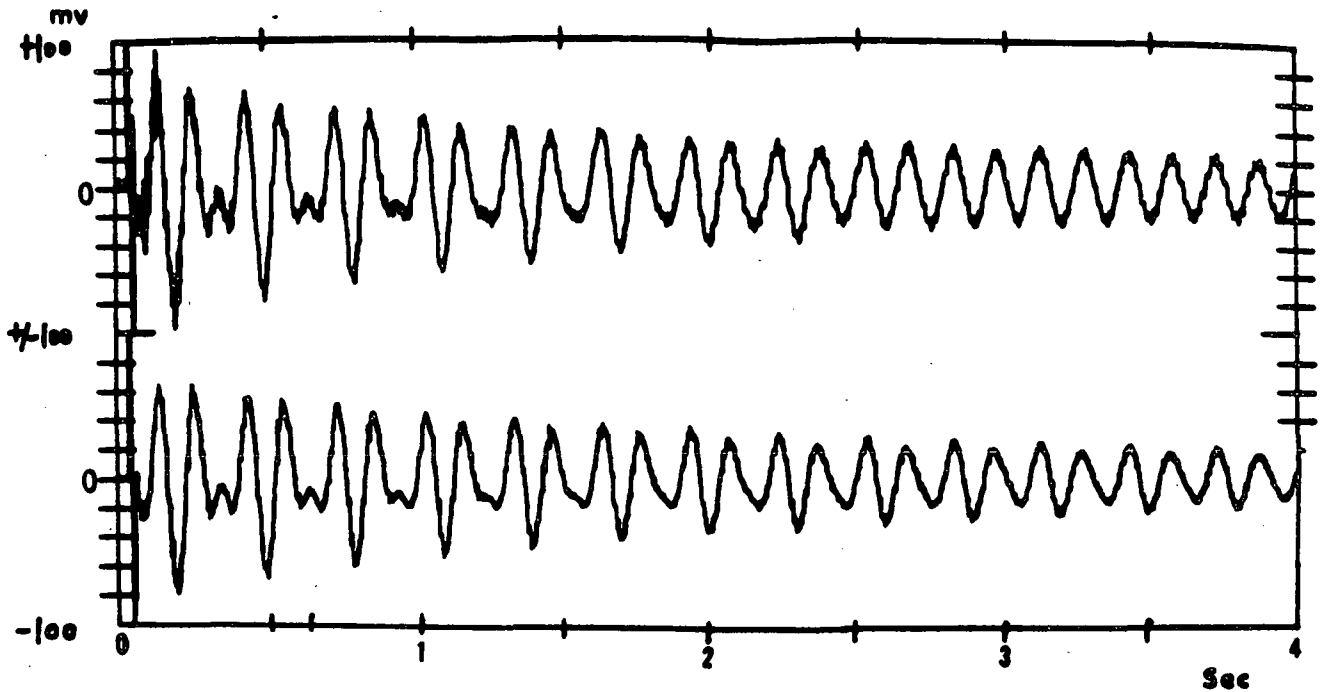


Fig. IV-6b Overlapped Plot

ORIGINAL PAGE IS
OF POOR QUALITY



**Fig. IV-7a Actual and Simulated Accelerometer #3 Responses to
A Linear Doublet Input at Wind Speed $U = 0$ m/sec**

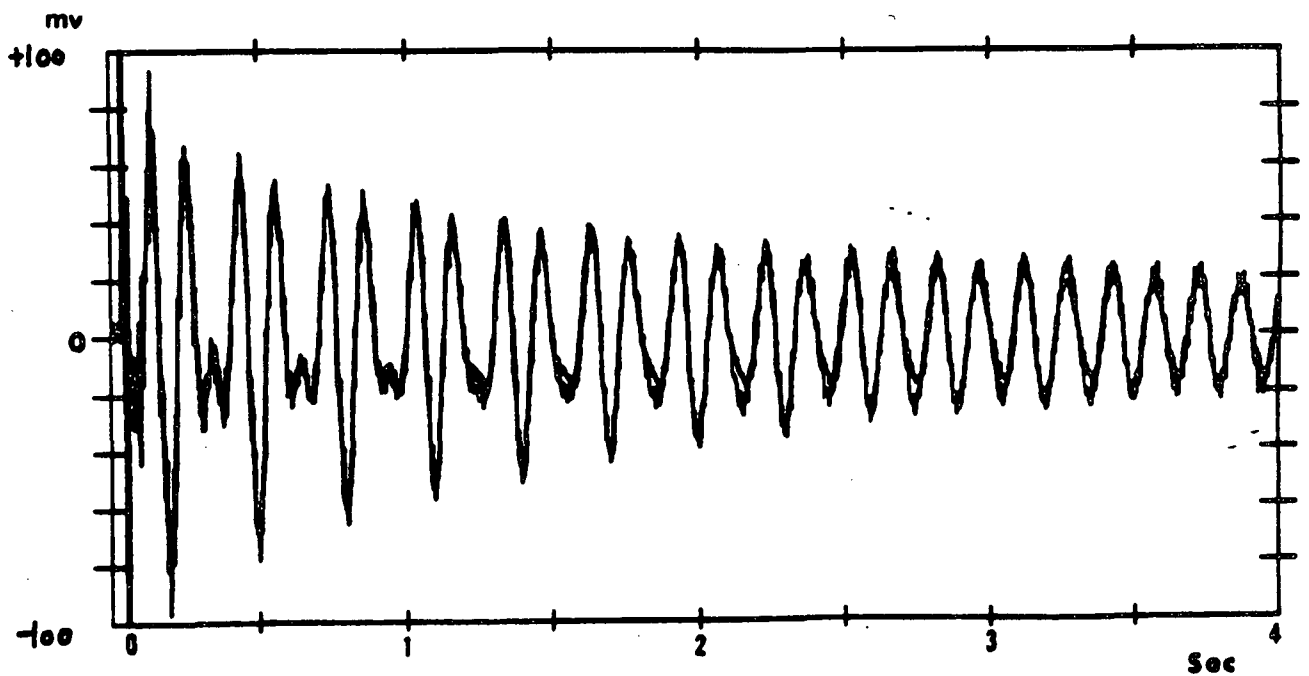
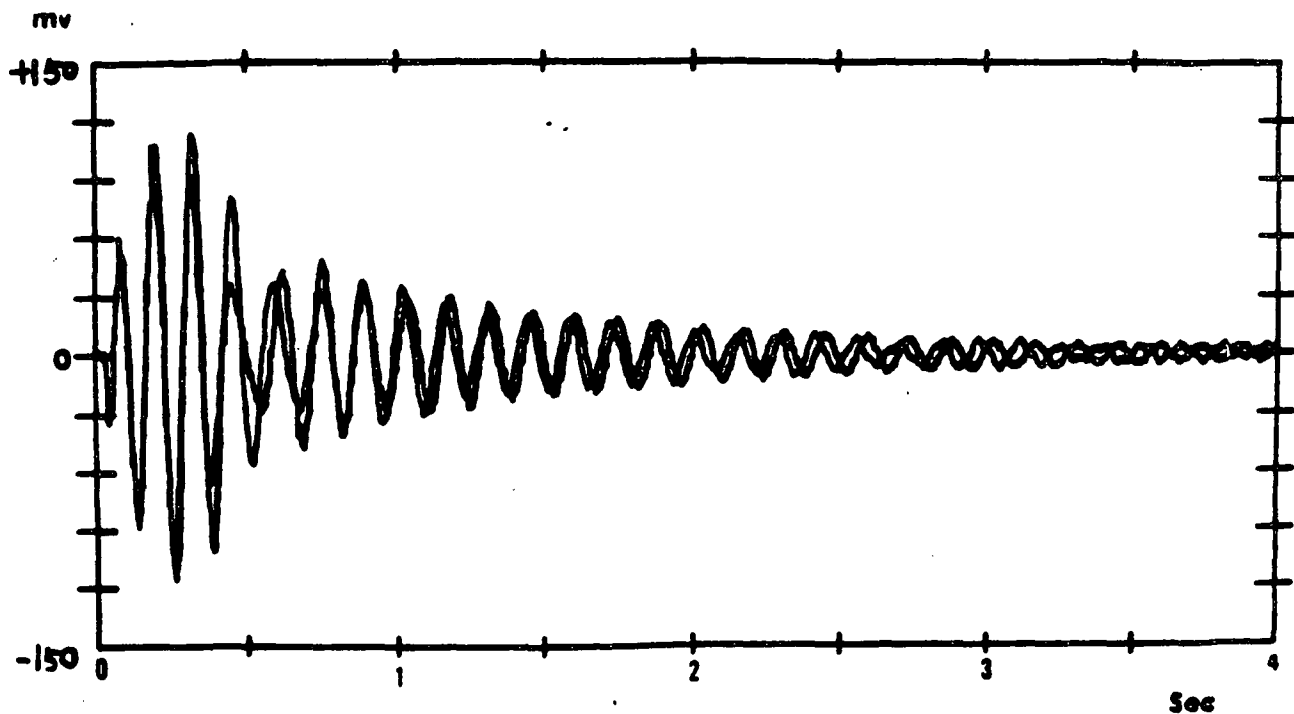


Fig. IV-7b Overlapped Plot



**Fig. IV-8a Actual and Simulated Pitch Responses to
A Linear Doublet Input at Wind Speed $U = 27.17$ m/sec**

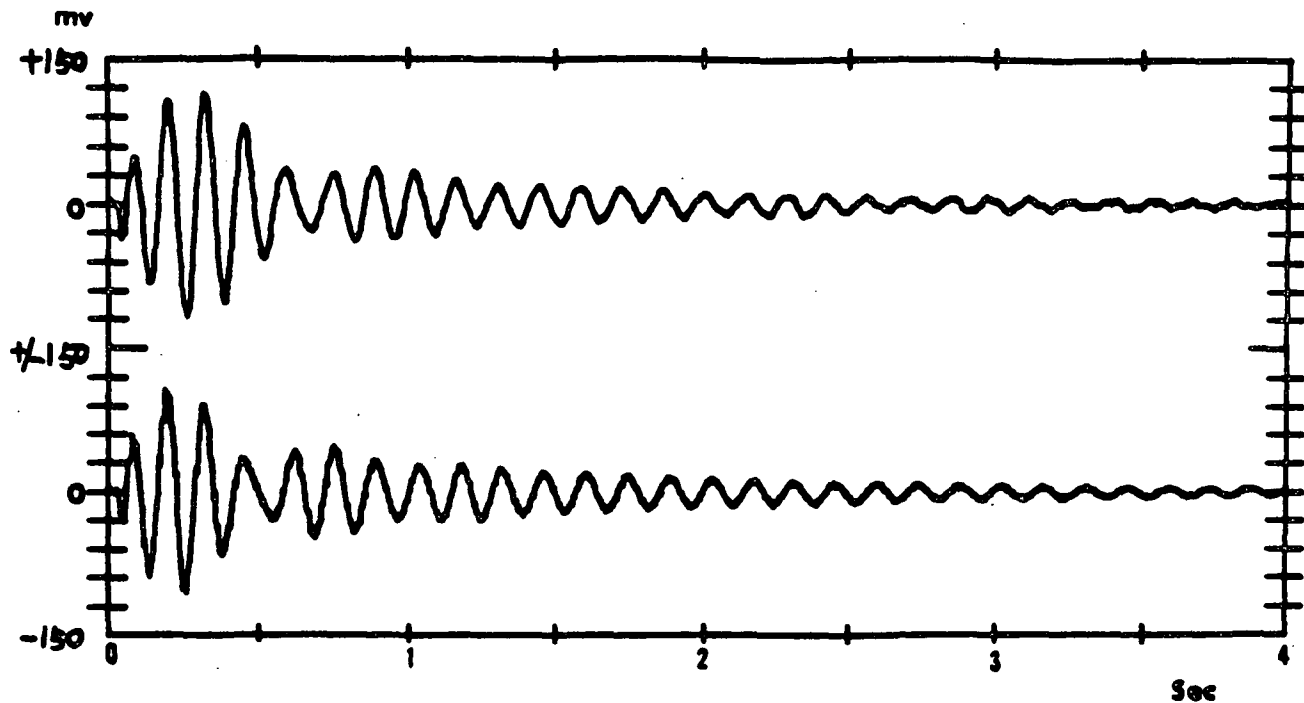


Fig. IV-8b Overlapped Plot

D. PARAMETER IDENTIFICATION

Due to the limitation of our laboratory facilities, only linear and angular positions were measured for system monitoring. However, we need all the system states to evaluate the estimation error for different sensor locations. Without adding other measuring instruments, one easy and possible approach would be to use a simple analog differentiating circuit to get their pseudo-rate measurements. However, the artificially introduced aerodynamics state was still unknown. Finally, we decided to design one more estimator using those position measurements to construct the pseudo system state for comparison with that obtained from the estimator using acceleration measurements. From the discussion in Section C about the approximation of using Eq. (4.1) to describe $Q_T(s, \lambda)$, it seems to be helpful to incorporate some system parameter identification schemes to identify those uncertain parameters in order to reduce the system modeling error effects. In our case, those key parameters, i.e. p , G , and z/p in Eq. (4.1) are good candidates to be identified. Although it was mentioned in Rock's conclusion that the doublet force input did not sufficiently excite the aerodynamic mode for it to be identifiable, an on-line parameter estimation scheme through Kalman filtering proposed by Mishne [33] was modified and tried for this purpose. The formulations and procedures are followed.

First, defining the innovation sequence

$$\nu(k) = y(k) - H\bar{x}[k, a(k-1)], \quad (4.2)$$

and the performance index

$$J = \frac{1}{2} \nu^T(k) W \nu(k), \quad (4.3)$$

where W is a positive-definite matrix and $a(k)$ is the parameter vector to be identified.

The gradient of the performance index J with respect to the parameter vector $a(k)$ is

$$D(k) = \frac{\partial J}{\partial a(k)} = \frac{\partial \nu^T(k)}{\partial a(k)} W \nu(k), \quad (4.4)$$

and the approximation to the second order derivative is

$$M(k) = \frac{\partial \nu^T(k)}{\partial a(k)} W \frac{\partial \nu(k)}{\partial a(k)}. \quad (4.5)$$

The on-line application of the Gauss-Newton iteration scheme is to make the following iteration after each measurement update:

$$a(k) = a(k-1) - M^{-1}(k) D(k). \quad (4.5)$$

After defining the following sensitivity functions

$$\bar{S}(k) = \frac{\partial \bar{x}(k)}{\partial a(k)}, \quad (4.6)$$

$$\hat{S}(k) = \frac{\partial \hat{x}(k)}{\partial a(k)}, \quad (4.7)$$

and finding the sensitivity matrices

$$F_a(a) = \frac{\partial F(a)}{\partial a(k)}, \quad (4.8)$$

$$F_{da}(a) = F_d F_a(a) T_s, \quad (4.9)$$

and

$$G_{da} = \left[\int_0^{T_s} e^{F(a)\tau} F_a(a) \tau d\tau \right] G, \quad (4.10)$$

then the identification iteration can proceed as follows:

Given initial values:

$$a(0), \quad \hat{x}(0), \quad \hat{S}(0),$$

Continuous system modeling:

$$\dot{x}(t) = F(a)x(t) + Gu(t) + \Gamma w(t)$$

Discretization and time update of the system state:

$$\bar{x}[k+1, a(k)] = F_d(a) \hat{x}[k, a(k)] + G_d(a) u(k)$$

Output predication error:

$$v(k+1) = y(k+1) - H\bar{x}[k+1, a(k)]$$

Time update of the sensitivity function:

$$\bar{S}(k+1) = F_d(a)\hat{S}(k) + F_{da}(a)\hat{x}[k, a(k)] + G_{da}(a)u(k)$$

Gradient of J :

$$D(k+1) = -\bar{S}^T(k+1)H^T W u(k+1)$$

Information matrix:

$$M(k+1) = \bar{S}^T(k+1)H^T W H \bar{S}(k+1)$$

Parameter update:

$$a(k+1) = a(k) - M^{-1}(k+1)D(k+1)$$

Parameter update of the system state:

$$\bar{x}[k+1, a(k+1)] = \bar{x}[k+1, a(k)] + \bar{S}(k+1)[a(k+1) - a(k)]$$

Measurement update:

$$\hat{x}[k+1, a(k+1)] = (I - KH)\bar{x}[k+1, a(k+1)] + Ky(k+1)$$

$$\hat{S}(k+1) = (I - KH)\bar{S}(k+1)$$

If this scheme is used to track the initial condition responses, i.e. $u(t) = 0$, then the computation can be further simplified by not considering the G , $G_d(a)$, and $G_{da}(a)$ matrices.

This scheme was checked with computer simulation. To identify the single parameter p , it converged within 100 time steps (1 sec) for 20% deviation from its nominal value. It converged quickly also for the identification of p and G , but had difficulty converging for all p , G , and z/p .

Unfortunately, the tests performed on the experimental data failed due to the existence of the process disturbance and measurement noise since the identified parameter values were equivalent to these noise levels. This subject will be left for future research.

E. ESTIMATOR DESIGN

In this section the estimator design is discussed. The sensor locations are evaluated based on the proposed sensor location index.

E-1 Choice of Q_w and R_v Matrices

Given an actual design problem, one can often assign a meaningful value to R_v which is based on the sensor accuracy. The same cannot be said for Q_w . Physically, Q_w is crudely accounting for both unknown disturbances and imperfections in the plant model. In the design process, we are usually forced to pick values of Q_w and to settle on an acceptable one after a certain amount of trial and error based on the quality of the estimation obtained using gains given by specific Q_w 's and R_v 's [53].

Although we use P as an indicator of relative estimation accuracy, it is only an absolute accuracy predicator when we choose the values of Q_w and R_v based on some knowledge of processes which are approximately white and more or less representative of the actual disturbance and noise levels. This makes the evaluation of our experiments difficult because the real disturbance and noise are not white. Whereas we may be able to find a Q_w and R_v which gives estimator

gains that minimize the estimation error, the error we calculate from this Q_w and R_w may have no relation to measured estimation error. The other difficulty we will encounter is that not only the noise levels are different between the two different types of accelerometers we used, but also they are different even among the same type of accelerometers. Fortunately, the inherent sensor noise level is low enough. One easy approach to overcome the above problems in checking theory versus experiment is to create a known external disturbance and add a known noise to our measurements.

E-2 Sensor Location Evaluation

Figure IV-9 shows the setup to evaluate the sensor locations, in which the estimator 1 using the position measurements to construct the pseudo full system state as the reference and the estimator 2 using the acceleration measurements to construct the system state estimate.

There are only three acceleration measurements available simultaneously due to the limited number (three) of the available accelerometer charge amplifiers. However, these three measurements can be used altogether to get the estimation error of the three sensors case, or separately for single or double sensors cases.

To simplify the presentation of the test results, both the theoretical and experimental values for single and double sensors cases are normalized by their corresponding three sensors values. So in the following figures, one will be the bottom line which corresponds to the use of all three sensors altogether. In these figures, the solid lines are the theoretical predictions which take into account the correlation between the process disturbance and measurement noise while the dotted lines do not. Generally speaking, the experimental results prove the trends predicted by the theory.

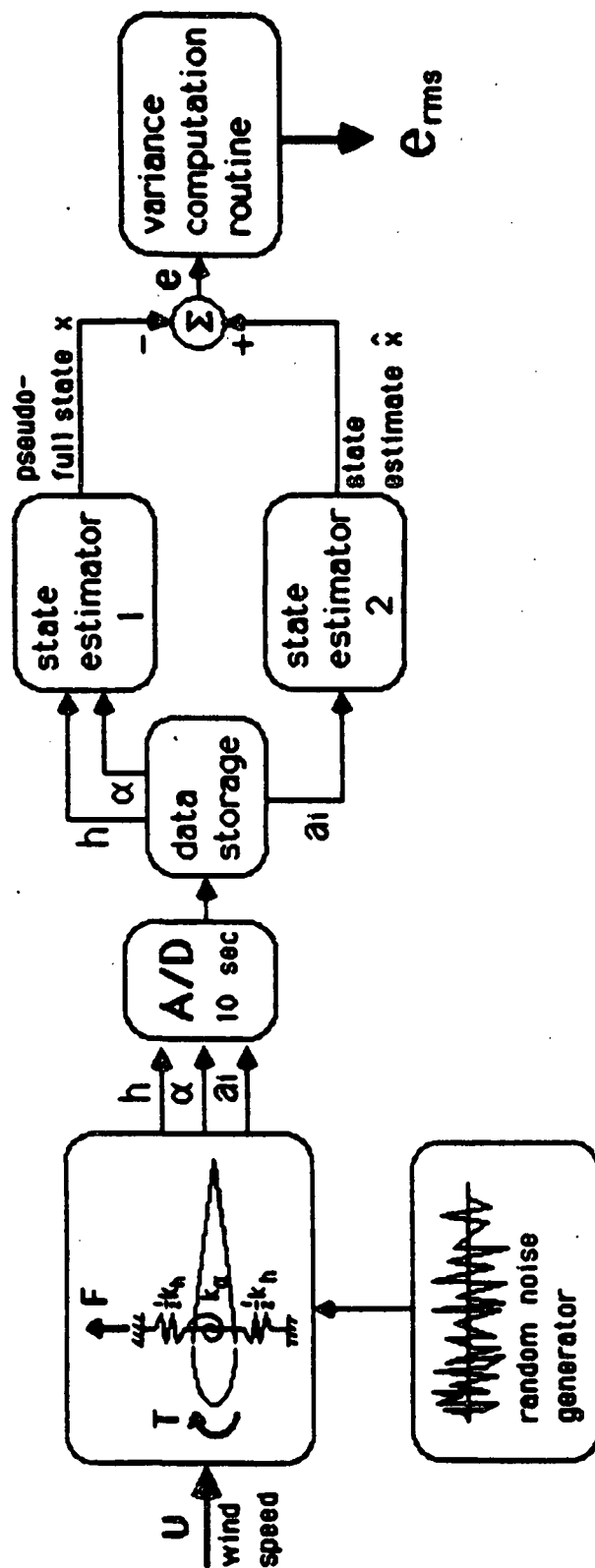


Fig. IV-9 Setup for the Sensor Location Evaluation

F. DISCUSSION OF THE RESULTS

Figure IV-10 shows that the experimental data of the first sensor are scattered about the theoretical value. This may be caused by its improper installation. Although this effect is not as significant by looking at the individual estimation error as in Fig. IV-11. It still can be seen in Fig. IV-12 for the double sensor case when one sensor is fixed at the third sensor location. At higher wind speeds the error due to this cause is more obvious, see Fig. IV-13. However, the result is still good for the other sensors.

For single disturbance input and single measurement case, the effect of changed sensor location amounts to the change of the zero locations of the transfer function from the disturbance input to the measurement output. This can be seen in Fig. IV-14 which shows the estimator pole locus for increasing $\frac{Q_w}{R_v}$ ratios. The corresponding sensors are numbered from one to six from the leading edge to the trailing edge. Also due to the limitation of those trapping transfer function zeros, the estimation gain and speed will not be able to increase at will.

WIND SPEED = 1.00 m/sec

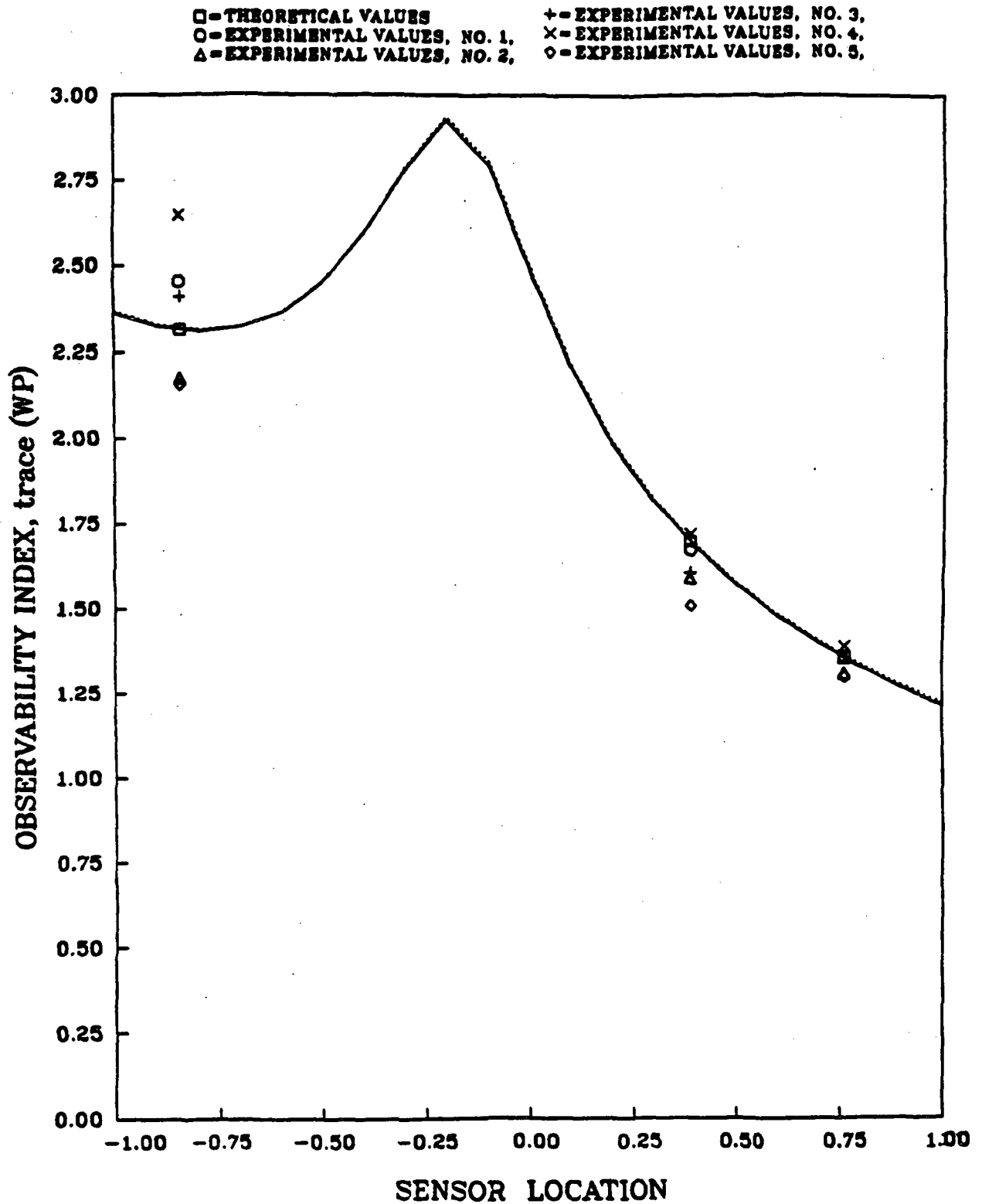


Fig. IV-10 Sensor Location Index vs Different Single Sensor Locations

EST. ERROR VS. SINGLE SENSOR LOC. ALONG THE WING CHORD WIND SPEED = 1.00 m/sec

O = THEORETICAL VALUES X = EXPERIMENTAL VALUES, NO. 3,
 Δ = EXPERIMENTAL VALUES, NO. 1. ◊ = EXPERIMENTAL VALUES, NO. 4.
 + = EXPERIMENTAL VALUES, NO. 2, ♣ = EXPERIMENTAL VALUES, NO. 5.

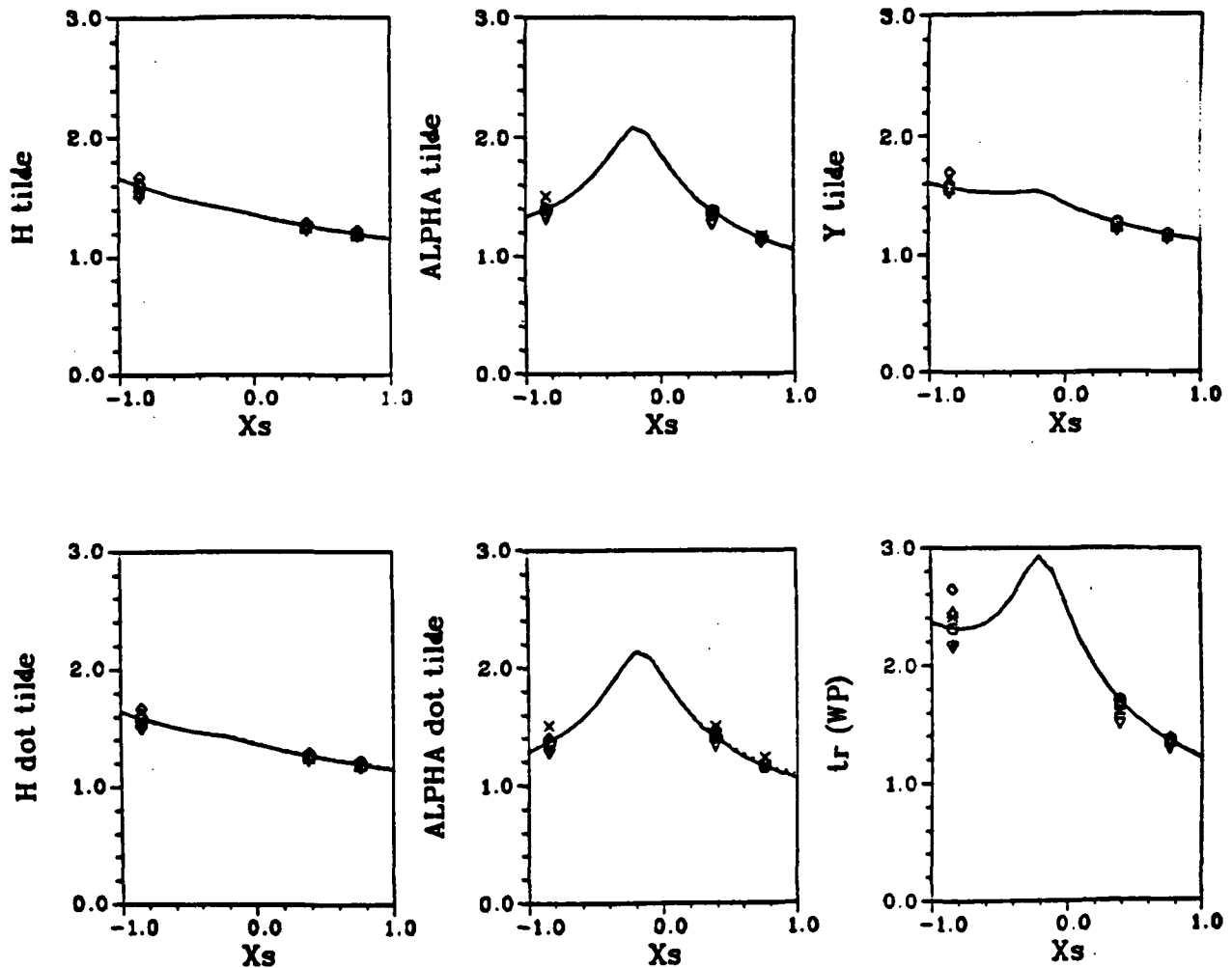


Fig. IV-11 Estimation Error vs Different Single Sensor Locations

WIND SPEED = 1.00 m/sec

□ - THEORETICAL VALUES + - EXPERIMENTAL VALUES, NO. 3,
○ - EXPERIMENTAL VALUES, NO. 1, × - EXPERIMENTAL VALUES, NO. 4,
△ - EXPERIMENTAL VALUES, NO. 2, ◊ - EXPERIMENTAL VALUES, NO. 5.

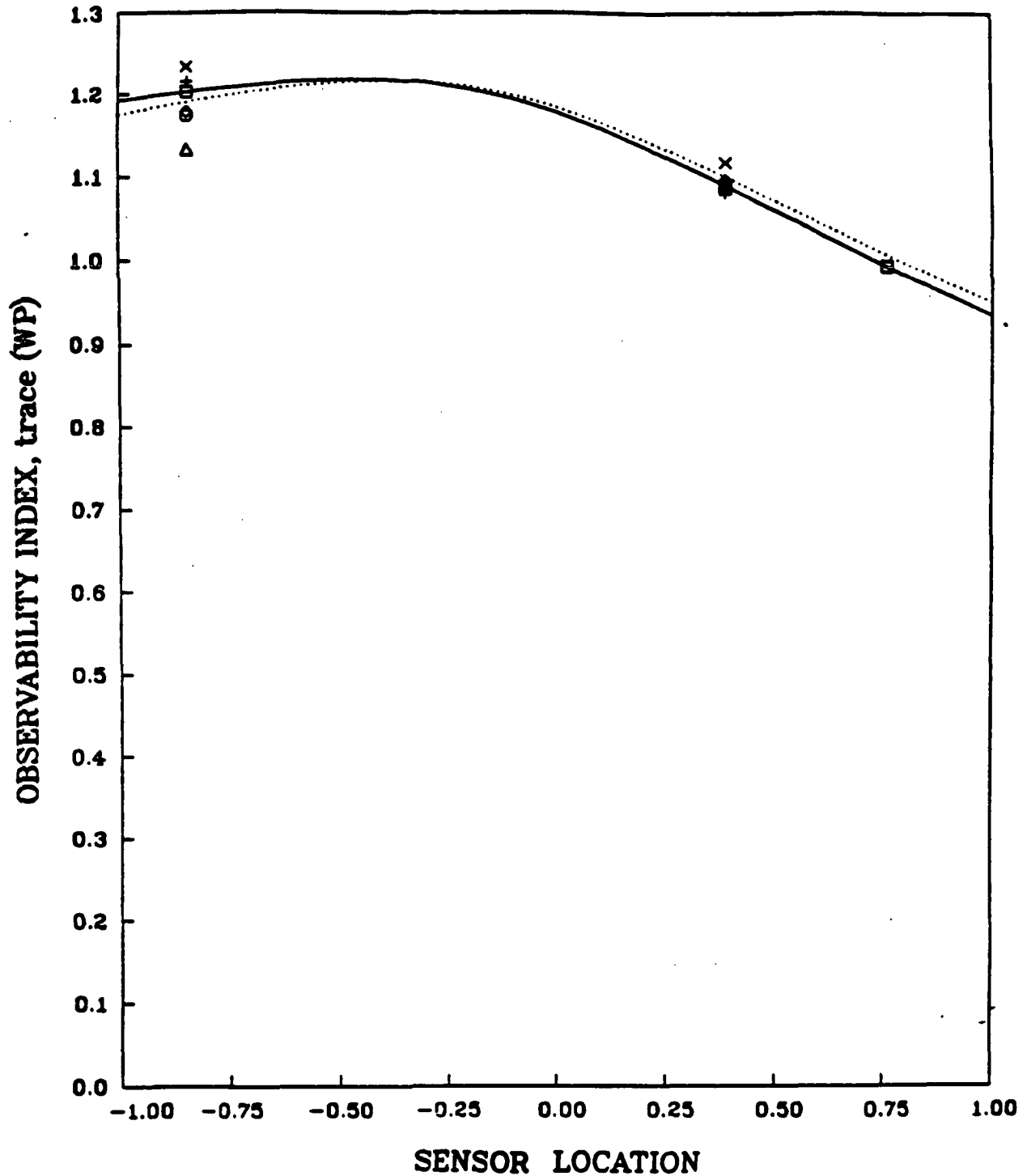


Fig. IV-12 Sensor Location Index vs Different Double Sensor Locations
WITH ONE FIXED AT 0.76

WIND SPEED = 27.19 m/sec

□ - THEORETICAL VALUES
○ - EXPERIMENTAL VALUES, NO. 1.
△ - EXPERIMENTAL VALUES, NO. 2,
+ - EXPERIMENTAL VALUES, NO. 3,
× - EXPERIMENTAL VALUES, NO. 4,
◊ - EXPERIMENTAL VALUES, NO. 5.

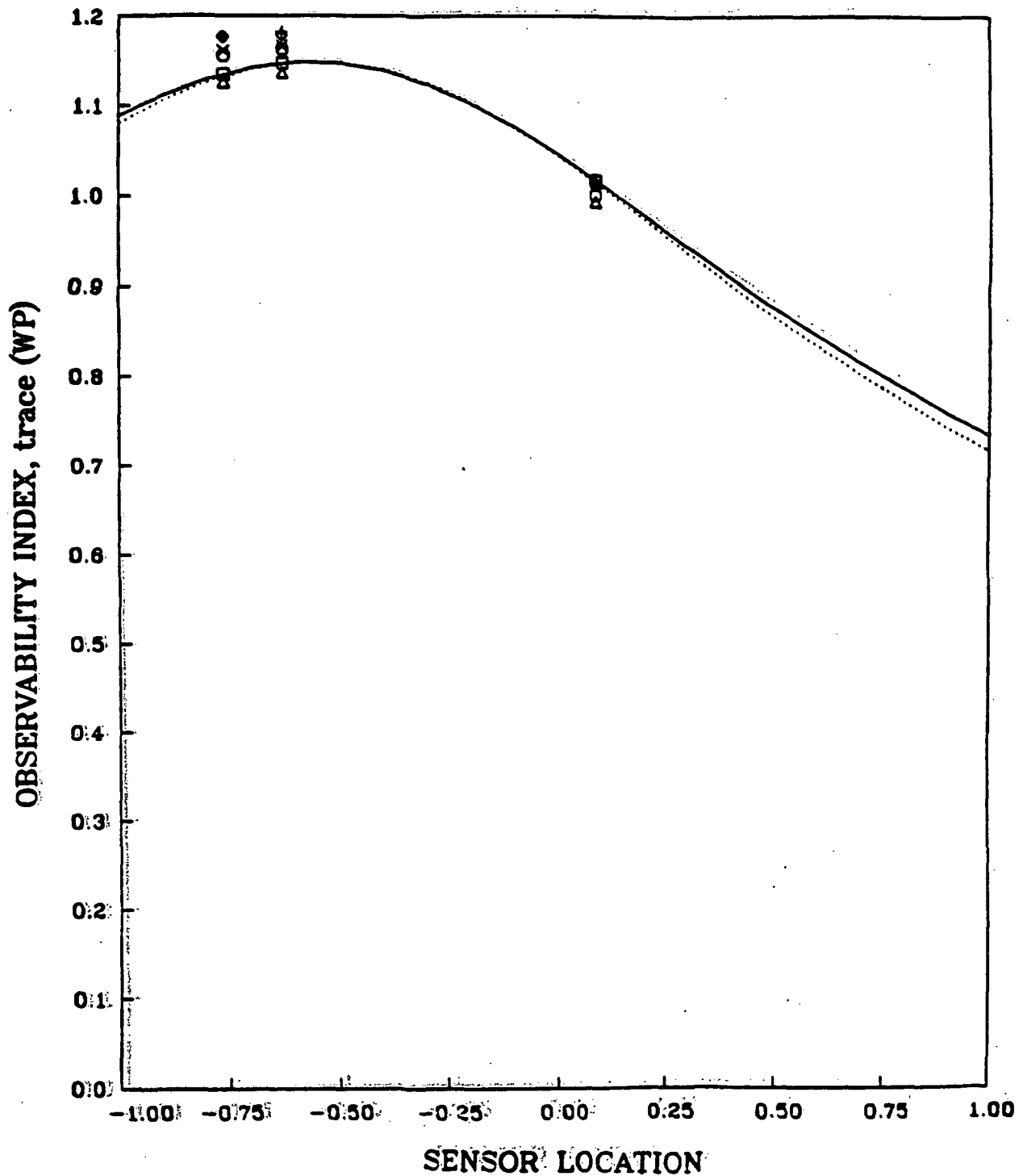


Fig. IV-13 Sensor Location Index vs Different Single Sensor Locations

ORIGINAL PAGE IS
OF POOR QUALITY

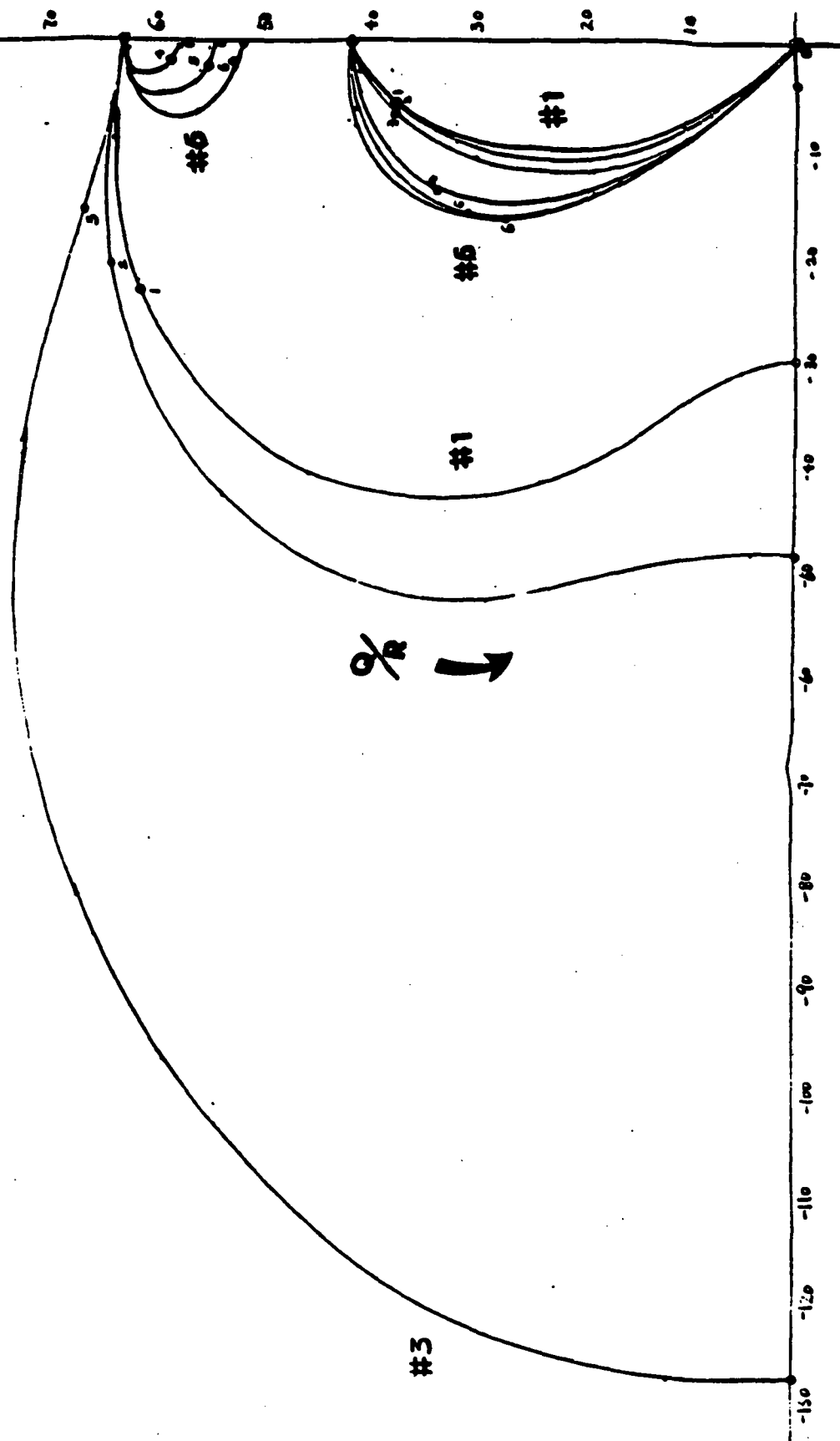


Fig. IV-14 Estimator Pole Locus vs Various $\frac{Q_e}{R_v}$ Ratios

Chapter V

SUMMARY AND RECOMMENDATIONS

A. SUMMARY

The problem of placement and number of sensors has been investigated. A sensor location index based on the weighted sum of the mean square estimation errors is proposed and has been experimentally verified. Although there have been many proposals regarding the choice of the criterion, the sensor location index features easy computation, having direct physical interpretation, and showing relative improvement for an increased number of sensors. Also this new criterion makes the gradient formulation easy to handle and compute. A computer program for the systematic optimal sensor location search is developed based on the gradient search optimization technique.

Since the use of accelerometers as measuring devices is so common in most control applications, the control design computer program OPTSYS has been modified to accept a more general input form including a rate measurement and which also takes into account the correlation between the process disturbance and measurement noise introduced by those accelerometers. Similarly, an iteration scheme doing this for the discrete case is also developed to facilitate the estimator implementation on digital computers.

An experimental study for choosing the sensor location has been conducted on an aeroelastic system. It consists of a NACA 0015 typical section wing with six accelerometers installed inside along the wing chord as the esti-

mator measuring instruments, an existing wind tunnel section, and some other accompanying experimental devices. Fabrication techniques are developed and apparatus built for experimental studies.

A sensor location for which the system is unobservable has been verified to be the center of percussion of the rigid two degree of freedom typical section wing. System modeling which includes the unsteady aerodynamics model is improved and experimentally verified. An on-line parameter identification through Kalman filtering has been formulated and applied to aerodynamic parameter identification. It is successful in simulations when no system disturbance and measurement noise exists, but fails for the actual system test due to the system noises.

Sensor location choice is evaluated experimentally based on the proposed sensor location index. It proves the trend predicted by the theory. This experimental evaluation on an aeroelastic system is significant since it is believed to be the first for feasibility studies.

After investigating the double sensor example which results in collocated sensors at the trailing edge we can see the negative side of the sensor location index. This result shows that it may be too dependent on the theoretical modeling of the system and it suggests that a more realistic index should also take into account the parameter uncertainties of the system for sensor location selection. Specifically, one would like to separate the sensors if there was no model knowledge and depend only on the kinematic information available from the two sensors for the two mechanical degrees of freedom. The results also show the need for accurate models for the process disturbance and measurement noise when making critical decisions.

B. RECOMMENDATIONS FOR FUTURE RESEARCH

- 1) Newton-Raphson technique can be applied to the sensor location search program for faster searching speed. Better schemes should be tried to detect the local minimums.
- 2) Extend the same idea to the optimal actuator location search through the duality between the estimator and controller design.
- 3) Estimation and sensor location analyses in the presence of system parameter uncertainties and modeling errors should be investigated. This should also include the exploration of a more realistic criterion which takes greater account of the kinematic information of the system as model uncertainties increase by considering a frequency-band weighted SLI.
- 4) Further investigation of system parameter identification with the current setup is suggested using optimal input design.
- 5) Adaptive estimation with combined on-line system parameter identification and state estimation should be developed.
- 6) Apply these results to the airfoil section with a trailing-edge flap (built by Stoltz) for improved estimation and feedback control of flutter.

Appendix A

MATHEMATICAL MODELING

In this Appendix, Section A is given for completeness of the derivations of equations of motion, although it is well known in many textbooks [46]. Section B includes some refinements to differentiate the mass of the airfoil and the mass of the whole plunge system. Section C and Tables A-1 - A-5 are summarized from Rock's thesis [25] for ease of reference and they are corrected for typographical errors.

A. EXTENDED HAMILTON PRINCIPLE

In general, for a system of N particles in equilibrium, the sum of the virtual works over all particles must be zero, or

$$\delta W = \sum_{n=1}^N \delta W_i = \sum_{n=1}^N \mathbf{R}_i \cdot \delta \mathbf{r}_i = 0, \quad (\text{A-1})$$

where \mathbf{R}_i is the resultant force vector acting on a particle at position \mathbf{r}_i [46].

After eliminating all the constraint forces and the internal forces among rigid bodies, we obtain

$$\sum_{n=1}^N \mathbf{F}_i \cdot \delta \mathbf{r}_i = 0, \quad (\text{A-2})$$

where \mathbf{F}_i is the resultant vector of externally applied forces at \mathbf{r}_i .

Equation (A-2) is the expression of the **virtual work principle**. It can be stated as: **If a system of forces is in equilibrium, the work done by all the externally applied forces through virtual displacements compatible with the constraints of the system is zero.**

By incorporating D'Alembert's principle, which states that the resultant force is in equilibrium with the inertia force, one can extend the principle of virtual work to cover the dynamic case following the same reasoning for Eq. (A-2), i.e.,

$$\sum_{n=1}^N (\mathbf{F}_i - \dot{\mathbf{p}}_i) \cdot \delta \mathbf{r}_i = \sum_{n=1}^N (\mathbf{F}_i - m_i \ddot{\mathbf{r}}_i) \cdot \delta \mathbf{r}_i = 0. \quad (\text{A-3})$$

Note that

$$\sum_{n=1}^N \mathbf{F}_i \cdot \delta \mathbf{r}_i = \delta W, \quad (\text{A-4})$$

$$\ddot{\mathbf{r}}_i \cdot \delta \mathbf{r}_i = \frac{d}{dt}(\dot{\mathbf{r}}_i \cdot \delta \mathbf{r}_i) - \delta \frac{1}{2} (\dot{\mathbf{r}}_i \cdot \dot{\mathbf{r}}_i), \quad (\text{A-5})$$

and

$$\begin{aligned} \sum_{n=1}^N m_i \ddot{\mathbf{r}}_i \cdot \delta \mathbf{r}_i &= \sum_{n=1}^N m_i \frac{d}{dt}(\dot{\mathbf{r}}_i \cdot \delta \mathbf{r}_i) - \delta \sum_{n=1}^N \frac{1}{2} m_i (\dot{\mathbf{r}}_i \cdot \dot{\mathbf{r}}_i) \\ &= \sum_{n=1}^N m_i \frac{d}{dt}(\dot{\mathbf{r}}_i \cdot \delta \mathbf{r}_i) - \delta T. \end{aligned} \quad (\text{A-6})$$

Introducing Eq. (A-4) and Eq. (A-6) into Eq. (A-3), one obtains

$$\delta T + \delta W = \sum_{n=1}^N m_i \frac{d}{dt}(\dot{\mathbf{r}}_i \cdot \delta \mathbf{r}_i). \quad (\text{A-7})$$

Integrating Eq. (A-7) between t_1 and t_2 , the result is

$$\begin{aligned}
\int_{t_1}^{t_2} (\delta T + \delta W) dt &= \int_{t_1}^{t_2} \sum_{n=1}^N m_i \frac{d}{dt} (\dot{\mathbf{r}}_i \cdot \delta \mathbf{r}_i) dt \\
&= \sum_{n=1}^N m_i \dot{\mathbf{r}}_i \cdot \delta \mathbf{r}_i \Big|_{t_1}^{t_2} = 0,
\end{aligned} \tag{A-8}$$

assuming

$$\delta \mathbf{r}_i = 0 \text{ at } t = t_1 \text{ and } t = t_2. \tag{A-9}$$

Equation (A-8) is referred as **extended Hamilton principle** by letting W consist of both conservative and nonconservative works. Now Eq. (A-8) becomes

$$\int_{t_1}^{t_2} (\delta T + \delta W_c + \delta W_{nc}) dt = \int_{t_1}^{t_2} (\delta T - \delta V + \delta W_{nc}) dt = 0, \tag{A-10}$$

using the fact

$$\delta W_c = -\delta V. \tag{A-11}$$

The expressions T and V can be thought of in the following forms (in our special case)

$$T = T(\dot{\mathbf{r}}), \tag{A-12}$$

$$V = V(\mathbf{r}), \tag{A-13}$$

where \mathbf{r} is a generalized coordinate vector; and noting that

$$\delta T = \frac{\partial T}{\partial \dot{\mathbf{r}}} \delta \dot{\mathbf{r}}, \tag{A-14a}$$

$$\delta V = \frac{\partial V}{\partial \mathbf{r}} \delta \mathbf{r}, \tag{A-14b}$$

$$\delta W_{nc} = \mathbf{Q}_{nc} \cdot \delta \mathbf{r}, \quad (\text{A-14c})$$

where \mathbf{Q}_{nc} is a generalized nonconservative force vector.

After substituting Eqs. (A-12)-(A-14) into Eq. (A-10), integrating by parts and using the assumption of Eq. (A-9), also noting that the resulting equation equals to zero must hold for arbitrary $\delta \mathbf{r}$, we obtain the general form of the **Lagrange's equation**

$$\frac{d}{dt} \left(\frac{\partial T}{\partial \dot{\mathbf{r}}} \right) + \frac{\partial V}{\partial \mathbf{r}} = \mathbf{Q}_{nc}. \quad (\text{A-15})$$

B. EQUATIONS OF MOTION

B-1 Two DOF (degree of freedom) Model

Figure A-1 shows the physical system and its modeling representation. In this case,

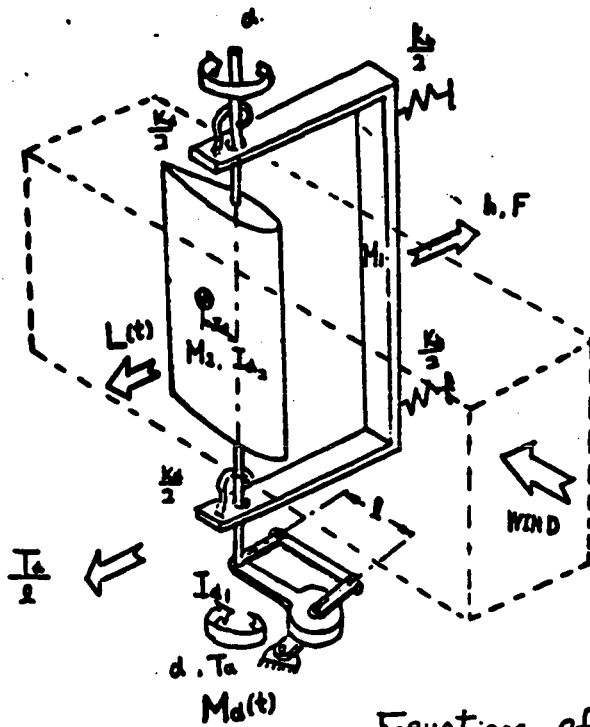
$$\mathbf{r}^T = \begin{bmatrix} h & \alpha \end{bmatrix}, \quad (\text{A-16})$$

$$T = \frac{1}{2} M_T \dot{h}^2 + \frac{1}{2} I_\alpha \dot{\alpha}^2 + S_\alpha \dot{\alpha} \dot{h}, \quad (\text{A-17})$$

$$V = \frac{1}{2} K_h h^2 + \frac{1}{2} K_\alpha \alpha^2. \quad (\text{A-18})$$

The virtual work term arises from the external energy input into the structural system by the torque T_α about the elastic axis (EA), the force F to the EA, and the unsteady pressure difference between the upper and lower wing surfaces [18, p. 39]. The unsteady pressure distribution can be defined as

$$\Delta p(x, t) = p(x, y=0^+, t) - p(x, y=0^-, t), \quad (\text{A-19})$$



2 DOF Modeling

$$g^T = [h \quad a]$$

$$T = \frac{1}{2} M_T \dot{h}^2 + \frac{1}{2} I_a \dot{\alpha}^2 + S_a \dot{\alpha} \dot{h}$$

$$V = \frac{1}{2} K_h h^2 + \frac{1}{2} K_a \alpha^2$$

$$Q_h = F - \frac{T_a}{l} - L(t)$$

$$Q_a = T_a + M_a(t)$$

$$\text{Since } \frac{d}{dt} \left(\frac{\partial T}{\partial \dot{g}} \right) + \frac{\partial V}{\partial g} = Q$$

$$M_T = M_1 + M_2$$

$$I_a = I_1 + I_2$$

$$S_a = M_2 l a$$

Equations of Motion with added Damping Terms

$$\begin{cases} M_T \ddot{h} + S_a \ddot{\alpha} + C_h \dot{h} + K_h h = F - \frac{T_a}{l} - L(t) \\ S_a \ddot{h} + I_a \ddot{\alpha} + C_a \dot{\alpha} + K_a \alpha = T_a + M_a(t) \end{cases}$$

$$\begin{bmatrix} M_T s^2 + C_h s + K_h & S_a s^2 \\ S_a s^2 & I_a s^2 + C_a s + K_a \end{bmatrix} \begin{bmatrix} H \\ \alpha \end{bmatrix} = \begin{bmatrix} 1 & -\frac{1}{l} \\ 0 & 1 \end{bmatrix} \begin{bmatrix} F \\ T_a \end{bmatrix} + \begin{bmatrix} -L(t) \\ M_a(t) \end{bmatrix}$$

$$\Delta(s) = (M_T s^2 + C_h s + K_h)(I_a s^2 + C_a s + K_a) - S_a^2 s^4$$

$$\begin{cases} \frac{H}{F} = \frac{I_a s^2 + C_a s + K_a}{\Delta(s)} \\ \frac{\alpha}{F} = \frac{-S_a s^2}{\Delta(s)} \\ \frac{H}{T_a} = -\frac{(I_a s^2 + C_a s + K_a)/l + S_a s^2}{\Delta(s)} \\ \frac{\alpha}{T_a} = \frac{(M_T s^2 + C_h s + K_h) + S_a s^2/l}{\Delta(s)} \end{cases}$$

$$\begin{cases} L(t) = - \int_{-b}^b \Delta p(x,t) dx \\ M_a(t) = \int_{-b}^b \Delta p(x,t) (x-a) dx \end{cases}$$

Fig. A-1 Two Degree of Freedom Modeling: Plunge and Pitch

where

$p(x, y=0^+, t)$ = static pressure at airfoil upper surface,

$p(x, y=0^-, t)$ = static pressure at airfoil lower surface.

So the first variation of the nonconservative virtual work can be expressed as

$$\delta W_{nc} = - \int_{-b}^b \Delta p(x, t) \delta y dx + (F - \frac{T_\alpha}{l}) \delta h + T_\alpha \delta \alpha, \quad (A-20)$$

where

$$y = - [h + (x-a)\alpha], \quad (A-21)$$

and

$$\delta y = \frac{\partial y}{\partial h} \delta h + \frac{\partial y}{\partial \alpha} \delta \alpha = - [\delta h + (x-a) \delta \alpha]. \quad (A-22)$$

Substituting Eqs. (A-16)-(A-18) and (A-20) into Eq. (A-15), and adding the structural damping terms, the complete aeroelastic equations of motion become

$$M_T \ddot{h} + S_\alpha \ddot{\alpha} + C_h \dot{h} + K_h h = F - \frac{T_\alpha}{l} - L(t), \quad (A-23)$$

$$S_\alpha \ddot{h} + I_\alpha \ddot{\alpha} + C_\alpha \dot{\alpha} + K_\alpha \alpha = T_\alpha + M_\alpha(t), \quad (A-24)$$

where

$$S_\alpha = M_2 x_\alpha, \quad (A-25)$$

$$L(t) = - \int_{-b}^b \Delta p(x, t) dx, \quad (A-26)$$

$$M_\alpha(t) = \int_{-b}^b \Delta p(x, t)(x-a) dx. \quad (A-27)$$

B-2 Three DOF Model

Figure A-2 shows the same physical system but one more DOF is added to it's modeling representation. In this case,

$$\mathbf{r}^T = \begin{bmatrix} h & \alpha_2 & \alpha_1 \end{bmatrix}, \quad (\text{A-28})$$

$$T = \frac{1}{2}M_T\dot{h}^2 + \frac{1}{2}I_{\alpha_1}\dot{\alpha}_1^2 + \frac{1}{2}I_{\alpha_2}\dot{\alpha}_2^2 + S_\alpha\dot{\alpha}_2\dot{h}, \quad (\text{A-29})$$

$$V = \frac{1}{2}K_h h^2 + \frac{1}{2}\frac{K_\alpha}{2}\alpha_2^2 + \frac{1}{2}K_c(\alpha_2 - \alpha_1)^2 + \frac{1}{2}\frac{K_\alpha}{2}\alpha_1^2. \quad (\text{A-30})$$

And similarly,

$$\delta W_{nc} = - \int_{-b}^b \Delta p(x,t) \delta y dx + (F - \frac{T_\alpha}{l}) \delta h + T_\alpha \delta \alpha_1, \quad (\text{A-31})$$

where

$$y = - [h + (x-a)\alpha_2], \quad (\text{A-32})$$

and

$$\delta y = \frac{\partial y}{\partial h} \delta h + \frac{\partial y}{\partial \alpha_2} \delta \alpha_2 = - [\delta h + (x-a) \delta \alpha_2]. \quad (\text{A-33})$$

After substituting Eqs. (A-28)-(A-31) into Eq. (A-15) and adding the structural damping terms, we obtain the complete aeroelastic equations of motion

$$M_T \ddot{h} + S_\alpha \ddot{\alpha}_2 + C_h \dot{h} + K_h h = F - \frac{T_\alpha}{l} - L(t), \quad (\text{A-34})$$

C. UNSTEADY AERODYNAMICS MODELING

If an experimental airfoil with finite thickness is placed in a flow field bounded by tunnel walls, we must consider the blockage and lift interference effects.

C-1 Blockage Corrections

Blockage corrections account for the reduction in available cross-sectional area when a body of finite thickness is placed in a bounded flow field [62, p. 300]. These corrections may be divided into solid blockage term and wake blockage term for a finite thickness airfoil and its wake, respectively, see Fig. A-3. They amount to a correction on the airspeed, i.e.

$$U = (1 + \epsilon_{sb} + \epsilon_{wb}) U_{uc}, \quad (\text{A-37})$$

where U_{uc} is the uncorrected free stream flow velocity. The results for our NACA 0015 airfoil with a b/H ratio of 0.5278 is a 1.9% increase in the airspeed.

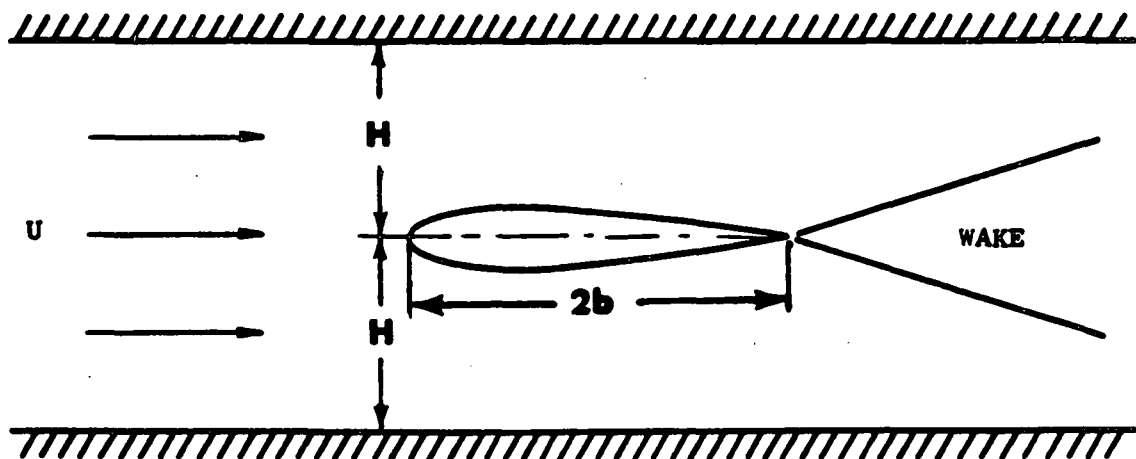


Fig. A-3 Blockage Effects

C-2 Lift Interference Effect

This effect is caused by the wind tunnel walls surrounding the airfoil. Assume an infinitely thin airfoil performing oscillations with an infinitely small amplitude. Its magnitude is prescribed in every point of the wing chord instead of the airfoil contour for simplification. The wind tunnel is considered to be infinitely long with constant cross section so that it does not influence the undisturbed flow. The airfoil spans the height of the tunnel section equidistant from and parallel to the side walls. The flow field can be considered as two dimensional and incompressible by assuming invicid, low speed air flow. Under these conditions, Timman solves the problem with an exact solution [20] using the velocity potential functions and conformal transformations in a manner analogous to Theodorsen's treatment of an airfoil in free (unconstrained) flight [19].

Using the coordinate systems in Fig. A-4 and the two transformations

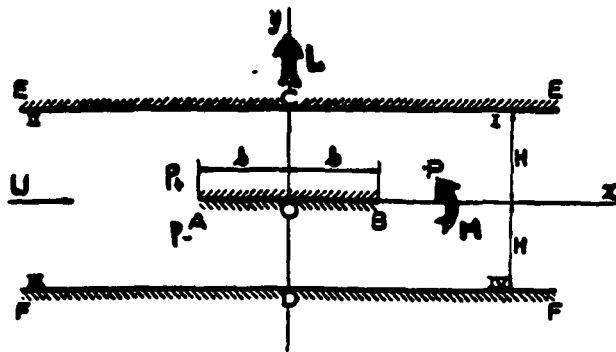
$$Z = X + i Y = \frac{\sinh \pi z / 2H}{\sinh \pi b / 2H}, \quad (\text{A-38})$$

$$Z = \text{cn}(\zeta, k^*), \quad (\text{A-39})$$

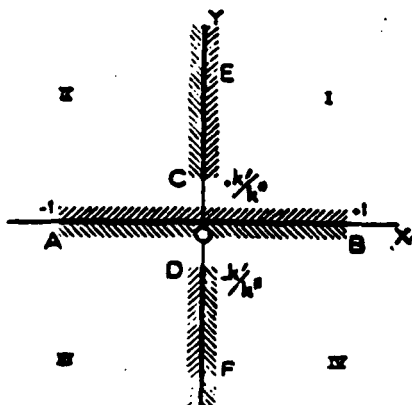
where

$$\begin{aligned} z &= x + i y, \\ \zeta &= \xi + i \eta, \\ k^* &= \tanh \pi b / 2H, \end{aligned}$$

and cn is a Jacobian elliptic cosine function, Timman maps the region in the z -plane bounded by the airfoil and the wind tunnel walls first into a cut Z -plane and then into a rectangle in the ζ -plane. These two successive transformations reduce the problem to the one which he can solve for the disturbance velocity potential $\Phi = \Phi_1 + \Phi_2$.



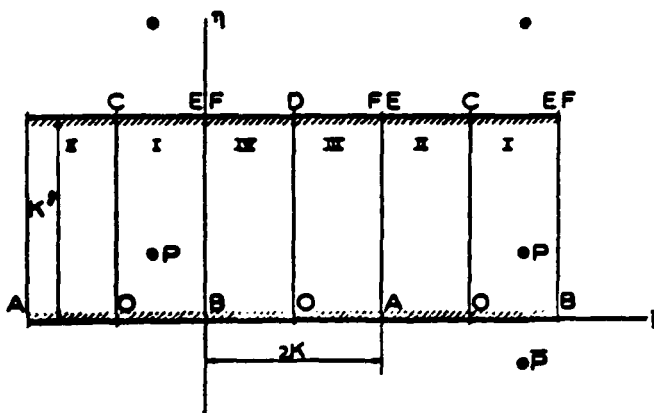
a). $z = x + iy$



TABLE

	$z = x + iy$	$Z = X + iY$	$\zeta = \xi + i\eta$
O	0, 0	0, 0	K, 0
A	-b, 0	-b, 0	2K, 0
B	+b, 0	+b, 0	0, 0
C	0, H	0, $\frac{H}{k}$	JK, K'
D	0, -H	0, $-\frac{H}{k}$	K, K'
E	$\pm \infty, +H$	$\pm \infty, +\infty$	0 or 2K, K'
F	$\pm \infty, -H$	$\pm \infty, -\infty$	0 or 2K, K'
P	x_P, y_P	X_P, Y_P	ξ_P, η_P
\bar{P}	—	—	$\xi_P, -\eta_P$

b). $Z = X + iY = \frac{\sinh \frac{\pi z}{2H}}{\sinh \frac{\pi b}{2H}}$



c). $\zeta = \xi + i\eta; Z = cn(\zeta, k')$

Fig. A-4 Timman's Coordinate Systems

Φ_1 is the velocity potential for the noncirculatory flow field and satisfies the boundary conditions in the z -plane

$$\frac{\partial \Phi_1}{\partial n} = u(x)e^{i\omega t} : y = 0, -b \leq x \leq b;$$

and

$$\frac{\partial \Phi_1}{\partial n} = 0 : y = \pm H, \quad (\text{A-40})$$

where n is in the normal direction to the wing chord or tunnel walls. The term $u(x)$ is a known function which describes the motion and shape of the airfoil. Φ_2 is the velocity potential for the circulatory flow field resulting from the vortices along the wake, and subjects to the boundary conditions in the z -plane

$$\frac{\partial \Phi_2}{\partial n} = 0 : y = 0, -b \leq x \leq b; \text{ and } y = \pm H. \quad (\text{A-41})$$

After applying the **Helmholtz condition of persistence of vorticity** and the **Kutta condition of finite velocity at the trailing edge**, Φ can be solved analytically. The pressure distribution over the airfoil can thus be found from the unsteady **Bernoulli's equation** in the linearized form [63, p. 226]

$$\Delta p(x,t) = -\rho \left[\frac{\partial}{\partial t} (\Phi_+ - \Phi_-) + U(u_+ - u_-) \right], \quad (\text{A-42})$$

where $+$ and $-$ represent the upper and lower surface of the airfoil, respectively. Finally, the lift and moment about EA can be obtained by integrating the pressure distribution over the airfoil using Eqs. (A-26)-(A-27).

Rock proved that the expressions of the Fourier transform of the lift and moment about EA of Timman's results could be written as [25, p. 27]

$$L(\omega) = a_1 \pi \rho b^2 [(i\omega)^2 h + U(i\omega)\alpha - ba(i\omega)^2 \alpha] \\ + a_2 2\pi \rho U b Q_T(k, \lambda) [(i\omega)h + U\alpha + b(a_3 - a)(i\omega)\alpha], \quad (\text{A-43a})$$

and

$$M_\alpha(\omega) = a_1 \pi \rho b^2 [ba(i\omega)^2 h - b^2(a_4 + a^2)(i\omega)^2 \alpha - Ub(a_5 - a)(i\omega)\alpha] \\ + a_2 2\pi \rho U b^2(a + a_5) Q_T(k, \lambda) [(i\omega)h + U\alpha + b(a_3 - a)(i\omega)\alpha], \quad (\text{A-43b})$$

where $Q_T(k, \lambda)$ is the **modified Theodorsen function**.

The technique of simply replacing ik with Laplace variable s is used to extend the **modified Theodorsen function** to include the general motions of an airfoil.

Definitions of Q_T and coefficients a_i are repeated here in Table A-1 for easy reference. It is also accompanied with free flight values, which are the limiting values as wall separation approaches infinity, i.e. $H/b \rightarrow \infty$. Values of coefficients a_i for different H/b ratios are computed by Rock as in Tables A-2 - A-3.

Rock also shows the approximation

$$Q_T(s, \lambda) \sim G \frac{(s+z)}{(s+p)} = G + \frac{G(z-p)}{(s+p)}, \quad (\text{A-44})$$

describes $Q_T(s, \lambda)$ accurately throughout the entire s -plane for $H/b \leq 2$. After incorporating this approximation into Eq. (A-43) and knowing that

$$a_3(s, \lambda) Q_T(s, \lambda) = a_7 - a_8 [1 - T(s, \lambda)], \quad (\text{A-45})$$

combining coefficients and using new defined coefficients in Table A-4, the expressions of lift and moment about EA may now be written as

$$\begin{aligned}
L(s) = & a_1 \pi \rho b^3 [s^2 \bar{h} + \bar{U} s \alpha - a s^2 \alpha] \\
& + a_2 2 \pi \rho \bar{U} b^3 \left\{ [a_{11} s \bar{h} + a_{11} \bar{U} \alpha + a_{12} s \alpha] \right. \\
& \left. + \bar{C}(s, \lambda) [a_{10} s \bar{h} + a_{10} \bar{U} \alpha + a_{13} s \alpha] \right\}, \tag{A-46a}
\end{aligned}$$

and

$$\begin{aligned}
M_\alpha(s) = & a_1 \pi \rho b^4 [a s^2 \bar{h} - \bar{U}(a_5 - a) s \alpha - (a_4 + a^2) s^2 \alpha] \\
& + a_2 2 \pi \rho \bar{U} b^4 (a + a_5) \left\{ [a_{11} s \bar{h} + a_{11} \bar{U} \alpha + a_{12} s \alpha] \right. \\
& \left. + \bar{C}(s, \lambda) [a_{10} s \bar{h} + a_{10} \bar{U} \alpha + a_{13} s \alpha] \right\}, \tag{A-46b}
\end{aligned}$$

where

$$\bar{C}(s, \lambda) \equiv \frac{T(s, \lambda) + 1}{2} = G' \frac{(s + z')}{(s + p)}. \tag{A-47}$$

Introducing an augmented aerodynamic state \bar{y} as

$$\bar{y} = \frac{1}{(s + p)} [a_{10} s \bar{h} + a_{10} \bar{U} \alpha + a_{13} s \alpha], \tag{A-48}$$

and combining Eqs. (A-23)-(A-24) and (A-46)-(A-48) yields

$$d_1 s^2 \bar{h} + d_8 s \bar{h} + d_3 \bar{h} + d_4 s^2 \alpha + d_9 s \alpha + d_{10} \alpha = \frac{F}{M_T b} - \frac{T_\alpha}{M_T b l} - d_{11} \bar{y}, \tag{A-49a}$$

$$f_1 s^2 \alpha + f_8 s \alpha + f_9 \alpha + f_4 s^2 \bar{h} + f_{10} s \bar{h} = \frac{T_\alpha}{I_\alpha} + f_{11} \bar{y}, \tag{A-49b}$$

where coefficients d_i and f_i are defined in Table A-4. After solving Eq. (A-49) for $s^2 \bar{h}$ and $s^2 \alpha$, and replacing the Laplace operator s by the time derivative, we get Eq. (A-50) with coefficients g_i defined in Table A-5.

$$\begin{bmatrix} \dot{h} \\ \dot{h} \\ \dot{\alpha} \\ \dot{\alpha} \\ \dot{y} \end{bmatrix} = \begin{bmatrix} 0 & 1 & 0 & 0 & 0 \\ -s_1 & -s_2 & -s_3 & -s_4 & -s_5 \\ 0 & 0 & 0 & 1 & 0 \\ -s_6 & -s_7 & -s_8 & -s_9 & -s_{10} \\ 0 & -s_{11} & -s_{12} & -s_{13} & -s_{14} \end{bmatrix} \begin{bmatrix} \bar{h} \\ \dot{\bar{h}} \\ \alpha \\ \dot{\alpha} \\ \bar{y} \end{bmatrix} + \begin{bmatrix} 0 & 0 \\ +s_{19} & +s_{20} \\ 0 & 0 \\ +s_{21} & +s_{22} \\ 0 & 0 \end{bmatrix} \begin{bmatrix} F_v \\ T_v \end{bmatrix}$$

(A-50)

Table A-1 Definition of Coefficients

Definition of Coefficients, a_i	
Term	Constrained Flight (by Timman)
a_1	$\frac{64H^2qs_2}{\pi^2b^2}$
a_2	$\frac{8Hq^{\frac{1}{2}}s_1}{\pi b}$
$a_3(s^*,\lambda)$	$\frac{2\xi\bar{C} + (\gamma - 2\xi)}{(2 - \beta)\bar{C} + (\beta - 1)}$
a_4	$\frac{8H^2s_6}{\pi^2b^2qs_2}$
a_5	$\frac{4Hs_3}{\pi bq^{\frac{1}{2}}s_1}$
a_6	not used
$a_7 = \gamma$	$\frac{4Hq^{\frac{1}{2}}s_2}{\pi bs_1}$
$a_8 = \xi$	$\frac{\pi^2s_3H}{K^3bk^*}$
$a_9 = \beta$	$\frac{\pi^2q^{\frac{1}{2}}s_1}{K^2k^*}$

Table A-1 Definition of Coefficients (cont)

a_{10}	$2 - a_9$
a_{11}	$a_9 - 1$
a_{12}	$-a_{11}a - 2a_8 + a_7$
a_{13}	$-a_{10}a + 2a_8$
λ	$\pi b/2H$
k^*	$\tanh \lambda$
k'	$\sqrt{1 - k^2}$
K	complete elliptic integral of the first kind of k^*
K'	complete elliptic integral of the first kind of k
q	$e^{-\pi K'/K}$
\bar{U}	U/b
k	$\omega b/U = \omega/\bar{U}$
β^*	$e^{2\lambda}$
s^*	$sH/\pi U$

Table A-1 Definition of Coefficients (cont)

s_1	$\sum_{n=0}^{\infty} q^n \frac{1 + q^{2n+1}}{(1 - q^{2n+1})^2}$
s_2	$\sum_{n=0}^{\infty} \frac{q^{2n}}{2n+1} \frac{1 + q^{2n+1}}{(1 - q^{2n+1})^3}$
s_3	$\sum_{n=1}^{\infty} \gamma_n q^n \frac{1 + q^{2n}}{1 - q^{2n}}$
s_6	$\sum_{n=1}^{\infty} \frac{\gamma_n^2 q^{2n}}{n} \frac{1 + q^{2n}}{1 - q^{2n}}$
γ_n	$n \sum_{m=0}^{n-1} \frac{1}{(2m+1)(2n-2m-1)(1 - q^{2m+1})(1 - q^{2n-2m-1})}$ $+ n \sum_{m=0}^{\infty} \frac{q^{2m+1}}{(2m+1)(2n+2m+1)(1 - q^{2m+1})(1 - q^{2n+2m+1})}$
$F(a, b, c; z)$	$\frac{\Gamma(c)}{\Gamma(b)\Gamma(c-b)} \int_0^1 t^{b-1}(1-t)^{c-b-1}(1-tz)^{-a} dt$
F_1	$F\left(\frac{1}{2}, s^* + \frac{1}{2}, s^* + 1; \frac{1}{\beta^{s^*}}\right)$
F_2	$F\left(\frac{1}{2}, s^* + \frac{3}{2}, s^* + 2; \frac{1}{\beta^{s^*}}\right)$
F_3	$F\left(\frac{1}{2}, s^* - \frac{1}{2}, s^*; \frac{1}{\beta^{s^*}}\right)$

Table A-1 Definition of Coefficients (cont)

$T(s^*, \lambda)$	$\frac{s^* F_3 - \frac{1}{\beta^{s^*}} \frac{(s^* + \frac{1}{2})^2}{(s^* + 1)} F_2 + \frac{1}{\beta^s} \left[\frac{2E}{Kk'^2} - 1 - s^* \frac{4k^*}{k'^2} \right] F_1}{s^* F_3 - \frac{1}{\beta^{s^*}} \frac{(s^* + \frac{1}{2})^2}{(s^* + 1)} F_2 + \frac{1}{\beta^s} \left[\frac{2E}{Kk'^2} - 1 + s^* \frac{4k^*}{k'^2} \right] F_1}$
$\bar{Q}(s^*, \lambda)$	$\frac{T(s^*, \lambda) + 1}{2}$
$Q_T(s^*, \lambda)$	$(2 - \beta)\bar{C} + (\beta - 1)$
G	0.5
p	$0.269 \bar{U}$
z	$0.538 \bar{U}$
G'	$\frac{(G - a_{11})}{a_{10}}$
z'	$z + a_{11} \frac{(z - p)}{(G - a_{11})}$

Table A-2 a_i at Various H/b

a_i at Various H/b						
H/b	∞	10	2	1.745	1	0.5
a_1	1.0000	1.0021	1.0488	1.0631	1.1725	1.5191
a_2	1.0000	1.0041	1.0952	1.1224	1.3209	1.8971
$a_3(0)$	0.5000	0.4990	0.4788	—*	0.4438	0.4004
a_4	0.1250	0.1246	0.1168	0.1148	0.1023	0.0827
a_5	0.5000	0.4987	0.4735	0.4670	0.4299	0.3751
$a_7 = \gamma$	0.5000	0.4990	0.4788	0.4736	0.4438	0.4004
$a_8 = \xi$	0.2500	0.2478	0.2067	0.1966	0.1429	0.0767
$a_9 = \beta$	1.0000	1.0000	1.0000	1.0000	1.0000	1.0000

* See Table A-3.

Table A-3 Dependence of Timman's $a_3(k, \lambda)$ on k and H/b

Dependence of Timman's $a_3(k, \lambda)^*$ on k and H/b				
$k \quad H/b$	10	2	1	0.5
$k = 0$	0.4990 + 0i	0.4788 + 0i	0.4438 + 0i	0.4004 + 0i
$k = 0.1$	0.4994 + 0.0008i	0.4810 + 0.0116i	0.4470 + 0.0229i	0.4040 + 0.0297i
$k = 0.2$	0.4999 + 0.0012i	0.4867 + 0.0210i	0.4559 + 0.0420i	0.4143 + 0.0569i
$k = 0.3$	0.5003 + 0.0013i	0.4941 + 0.0273i	0.4687 + 0.0575i	0.4296 + 0.0798i
$k = 0.4$	0.5006 + 0.0013i	0.5017 + 0.0307i	0.4832 + 0.0683i	0.4479 + 0.0974i
$k = 0.5$	0.5009 + 0.0013i	0.5085 + 0.0319i	0.4978 + 0.0749i	0.4674 + 0.1098i
$k = 0.6$	0.5011 + 0.0013i	0.5143 + 0.0318i	0.5114 + 0.0781i	0.4866 + 0.1177i
$k = 0.8$	0.5014 + 0.0012i	0.5228 + 0.0298i	0.5339 + 0.0782i	0.5209 + 0.1235i
$k = 1.0$	0.5016 + 0.0011i	0.5283 + 0.0271i	0.5503 + 0.0739i	0.5482 + 0.1211i

* This parameter value is not used, it is for reference only.

Table A-4 Definition of Coefficients

Definition of Coefficients, d_i and f_i			
d_1	$1 + a_1/\mu$	d_7	$2a_2\bar{U}/\mu$
d_2	$2a_2a_{11}\bar{U}/\mu + 2\zeta_h\omega_h$	d_8	$d_2 + d_7 G' a_{10}$
d_3	ω_h^2	d_9	$d_5 + d_7 G' a_{13}$
d_4	$K_2x_\alpha - a_1a/\mu$	d_{10}	$d_8 + d_7 G' a_{10}\bar{U}$
d_5	$a_1\bar{U}/\mu + 2a_2a_{12}\bar{U}/\mu$	d_{11}	$d_7 G' (z' - p)$
d_6	$2a_2a_{11}\bar{U}^2/\mu$		
f_1	$1 + \frac{a_1(a_4 + a^2)}{K_2\mu r_\alpha^2}$		
f_2	$\frac{a_1(a_5 - a)\bar{U}}{K_2\mu r_\alpha^2} - \frac{2a_2(a + a_5)a_{12}\bar{U}}{K_2\mu r_\alpha^2} + 2\zeta_\alpha\omega_\alpha$		
f_3	$\omega_\alpha^2 - \frac{2a_2(a + a_5)a_{11}\bar{U}^2}{K_2\mu r_\alpha^2}$		
f_4	$x_\alpha/r_\alpha^2 - a_1a/K_2\mu r_\alpha^2$	f_8	$f_2 - f_7 G' a_{13}$
f_5	$-2a_2(a + a_5)a_{11}\bar{U}/K_2\mu r_\alpha^2$	f_9	$f_3 - f_7 G' a_{10}\bar{U}$
f_6	not used	f_{10}	$f_5 - f_7 G' a_{10}$
f_7	$2a_2(a + a_5)\bar{U}/K_2\mu r_\alpha^2$	f_{11}	$f_7 G' (z' - p)$

Table A-5 Definition of Coefficients

Definition of Coefficients, g_i	
$q_1 = d_8/d_1 - f_{10}/f_4$	$g_1 = q_9/q_7$
$q_2 = d_3/d_1$	$g_2 = q_8/q_7$
$q_3 = d_4/d_1 - f_1/f_4$	$g_3 = q_{11}/q_7$
$q_4 = d_9/d_1 - f_8/f_4$	$g_4 = q_{10}/q_7$
$q_5 = d_{10}/d_1 - f_9/f_4$	$g_5 = -q_{12}/q_7$
$q_6 = -d_{11}/d_1 - f_{11}/f_4$	$g_6 = q_2/q_3$
$q_7 = d_1/d_4 - f_4/f_1$	$g_7 = q_1/q_3$
$q_8 = d_8/d_4 - f_{10}/f_1$	$g_8 = q_5/q_3$
$q_9 = d_3/d_4$	$g_9 = q_4/q_3$
$q_{10} = d_9/d_4 - f_8/f_1$	$g_{10} = -q_6/q_3$
$q_{11} = d_{10}/d_4 - f_9/f_1$	$g_{11} = -a_{10}$
$q_{12} = -d_{11}/d_4 - f_{11}/f_1$	$g_{12} = -a_{10}\bar{U}$
	$g_{13} = -a_{13}$
	$g_{14} = p$
	$g_{15} = 1/d_4 q_7$
	$g_{16} = 1/f_1 q_7$
	$g_{17} = 1/d_1 q_3$
	$g_{18} = 1/f_4 q_3$

Table A-6 Derivative of Parameters

Derivative of parameters d_i and f_i w.r.t. G , p , and z			
$\frac{\partial d_8}{\partial G}$	d_7	$\frac{\partial d_{11}}{\partial G}$	$\frac{d_7(z-p)}{a_{10}}$
$\frac{\partial d_9}{\partial G}$	$\frac{d_7 a_{13}}{a_{10}}$	$\frac{\partial d_{11}}{\partial p}$	$-\frac{d_7 G}{a_{10}}$
$\frac{\partial d_{10}}{\partial G}$	$d_7 \bar{U}$	$\frac{\partial d_{11}}{\partial z}$	$\frac{d_7 G}{a_{10}}$
$\frac{\partial f_8}{\partial G}$	$-\frac{f_7 a_{13}}{a_{10}}$	$\frac{\partial f_{11}}{\partial G}$	$\frac{f_7(z-p)}{a_{10}}$
$\frac{\partial d_9}{\partial G}$	$-f_7 \bar{U}$	$\frac{\partial f_{11}}{\partial p}$	$-\frac{f_7 G}{a_{10}}$
$\frac{\partial f_{10}}{\partial G}$	$-f_7$	$\frac{\partial f_{11}}{\partial z}$	$\frac{f_7 G}{a_{10}}$

Table A-6 Derivative of Parameters (cont)

Derivative of parameters q_i and g_i w.r.t. G , p , and z			
$\frac{\partial q_1}{\partial G}$	$\left(\frac{d_7}{d_1} + \frac{f_7}{f_4} \right)$	$\frac{\partial g_7}{\partial G}$	$\left(\frac{d_7}{d_1} + \frac{f_7}{f_4} \right) \frac{1}{q_3}$
$\frac{\partial q_4}{\partial G}$	$\left(\frac{d_7}{d_1} + \frac{f_7}{f_4} \right) \frac{a_{13}}{a_{10}}$	$\frac{\partial g_9}{\partial G}$	$\left(\frac{d_7}{d_1} + \frac{f_7}{f_4} \right) \frac{a_{13}}{a_{10}} \frac{1}{q_3}$
$\frac{\partial q_5}{\partial G}$	$\left(\frac{d_7}{d_1} + \frac{f_7}{f_4} \right) \bar{U}$	$\frac{\partial g_8}{\partial G}$	$\left(\frac{d_7}{d_1} + \frac{f_7}{f_4} \right) \frac{\bar{U}}{q_3}$
$\frac{\partial q_6}{\partial G}$	$-\left(\frac{d_7}{d_1} + \frac{f_7}{f_4} \right) \frac{z-p}{a_{10}}$	$\frac{\partial g_{10}}{\partial G}$	$\left(\frac{d_7}{d_1} + \frac{f_7}{f_4} \right) \frac{z-p}{a_{10}} \frac{1}{q_3}$
$\frac{\partial q_8}{\partial G}$	$\left(\frac{d_7}{d_4} + \frac{f_7}{f_1} \right)$	$\frac{\partial g_2}{\partial G}$	$\left(\frac{d_7}{d_4} + \frac{f_7}{f_1} \right) \frac{1}{q_7}$
$\frac{\partial q_{10}}{\partial G}$	$\left(\frac{d_7}{d_4} + \frac{f_7}{f_1} \right) \frac{a_{13}}{a_{10}}$	$\frac{\partial g_4}{\partial G}$	$\left(\frac{d_7}{d_4} + \frac{f_7}{f_1} \right) \frac{a_{13}}{a_{10}} \frac{1}{q_7}$
$\frac{\partial q_{11}}{\partial G}$	$\left(\frac{d_7}{d_4} + \frac{f_7}{f_1} \right) \bar{U}$	$\frac{\partial g_3}{\partial G}$	$\left(\frac{d_7}{d_4} + \frac{f_7}{f_1} \right) \frac{\bar{U}}{q_7}$
$\frac{\partial q_{12}}{\partial G}$	$-\left(\frac{d_7}{d_4} + \frac{f_7}{f_1} \right) \frac{z-p}{a_{10}}$	$\frac{\partial g_5}{\partial G}$	$\left(\frac{d_7}{d_4} + \frac{f_7}{f_1} \right) \frac{z-p}{a_{10}} \frac{1}{q_7}$
$\frac{\partial q_6}{\partial p}$	$\left(\frac{d_7}{d_1} + \frac{f_7}{f_4} \right) \frac{G}{a_{10}}$	$\frac{\partial q_{12}}{\partial p}$	$\left(\frac{d_7}{d_4} + \frac{f_7}{f_1} \right) \frac{G}{a_{10}}$
$\frac{\partial g_5}{\partial p}$	$-\left(\frac{d_7}{d_4} + \frac{f_7}{f_1} \right) \left(\frac{z}{p} - 1 \right) \frac{G}{a_{10}} \frac{\bar{U}}{q_7}$	$\frac{\partial g_5}{\partial z}$	$\left(\frac{d_7}{d_4} + \frac{f_7}{f_1} \right) \left(\frac{z}{p} - 1 \right) \frac{G}{a_{10}} \frac{\bar{U}}{q_7}$
$\frac{\partial g_{10}}{\partial p}$	$-\left(\frac{d_7}{d_1} + \frac{f_7}{f_4} \right) \left(\frac{z}{p} - 1 \right) \frac{G}{a_{10}} \frac{\bar{U}}{q_3}$	$\frac{\partial g_{10}}{\partial z}$	$\left(\frac{d_7}{d_1} + \frac{f_7}{f_4} \right) \left(\frac{z}{p} - 1 \right) \frac{G}{a_{10}} \frac{\bar{U}}{q_3}$
$\frac{\partial g_{14}}{\partial p}$	$\left(\frac{z}{p} - 1 \right) \bar{U}$		

Appendix B

ACTUATOR AND SENSOR CALIBRATIONS

Characteristics of sensors and actuators enter into the determination of system parameters (see Appendix C) and are important in predicting system dynamic behavior. Accurate calibration is therefore necessary.

Since the same test section built by Rock was used for our experiments with a new airfoil, most of the calibration procedures were similar to those used by him, however, with some different approaches. While every effort was made to reproduce or cross check with Rock's results, the calibrations were carried out independently with different tools and equipment.

A. ACTUATORS

A-1 Static Response

The static calibration procedures of the plunge and pitch actuators are outlined in Fig. B-1. A PDP-11 computer system was used to implement the digital controller with the actuator as the controlled element. Known disturbance loads (weights hung in the gravity field) were balanced by the action of this controller. A 60 Hz dither signal was added to eliminate the effects of stiction.

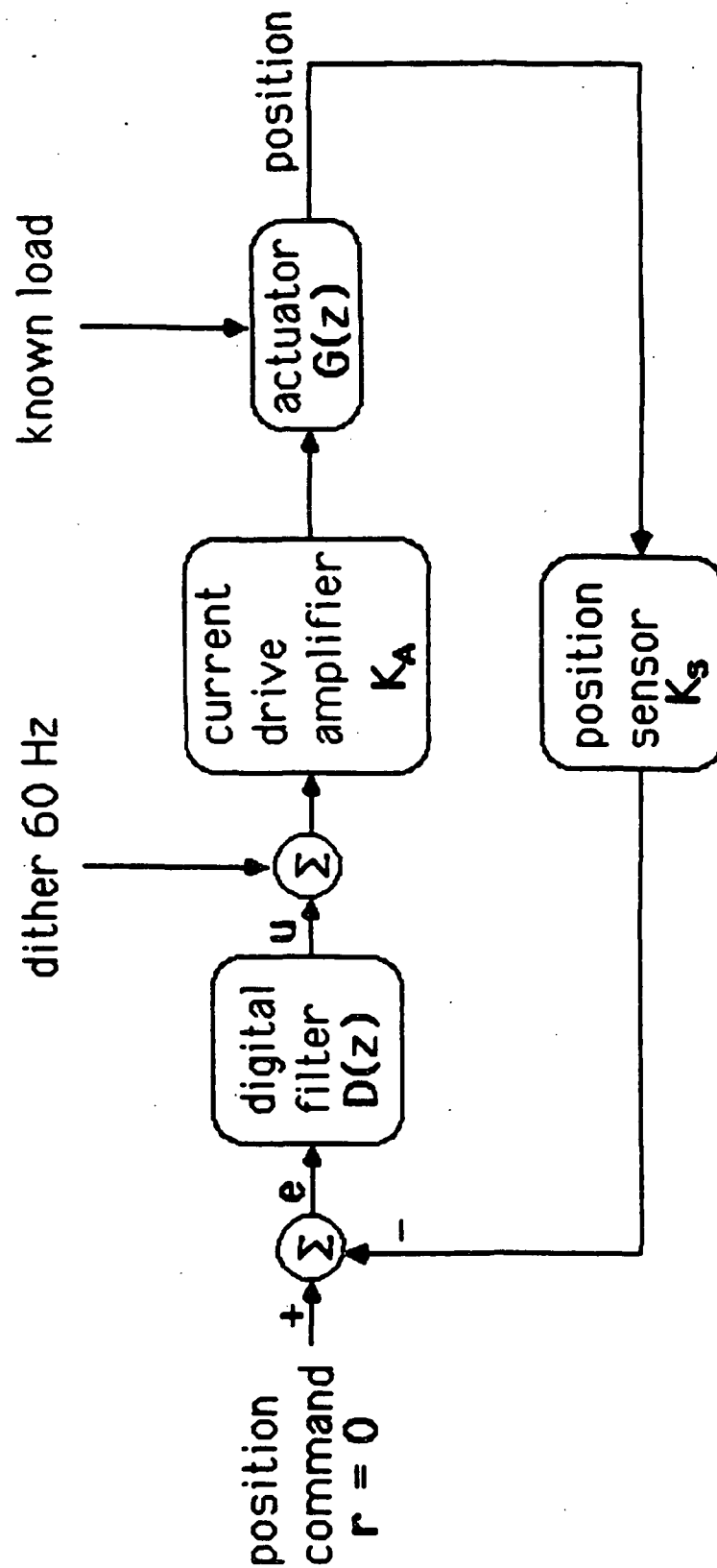


Fig. B-1 Experimental Configuration for Static Calibration of Actuators

A-2 Dynamic Response

A Nicolet 660B dual-channel FFT analyzer was used with a Tektronix P6042 current probe to find the frequency responses of the actuators and the current-drive amplifier.

A Hewlett-Packard 3722A noise generator was used to generate an infinite sequence, 150 Hz bandwidth (system dynamics was about 10 Hz) noise signal to drive the amplifier. First the transfer functions between the current outputs from the amplifier and the voltage inputs to the amplifier were obtained using a pure resistive load. It verified that the amplifier worked as a constant gain amplifier ($K_{A,plunge} = 0.590 \text{ A/V}$, $K_{A,pitch} = 0.270 \text{ A/V}$) with zero phase shift within 0-100 Hz. Similar transfer functions with actuators connected to the amplifier were obtained, which showed a small change in amplifier gains ($K_{A,plunge} = 0.630 \text{ A/V}$, $K_{A,pitch} = 0.273 \text{ A/V}$) because of the back electromagnetic force (EMF) from the actuators.

Then the transfer functions between the position sensor voltage outputs and the actual actuator current inputs were obtained. These transfer functions showed the responses of the system also (see Fig. B-2 and B-3). Above 10 Hz, the actuators should behave as forces (torques) acting on pure masses (moment of inertias) with minus 40 dB/decade magnitude slope and 180 degree phase lag. However, there were significant phase shift and change in magnitude slope. Specifically, a big magnitude drop and phase shift at 63.5 Hz in the plunge motor's response and 45 degree phase shift at 60 Hz in the pitch motor's response. They were caused partly by the associated system dynamics and those high frequency resonances of the actuators, as well as their bandwidth limitations.

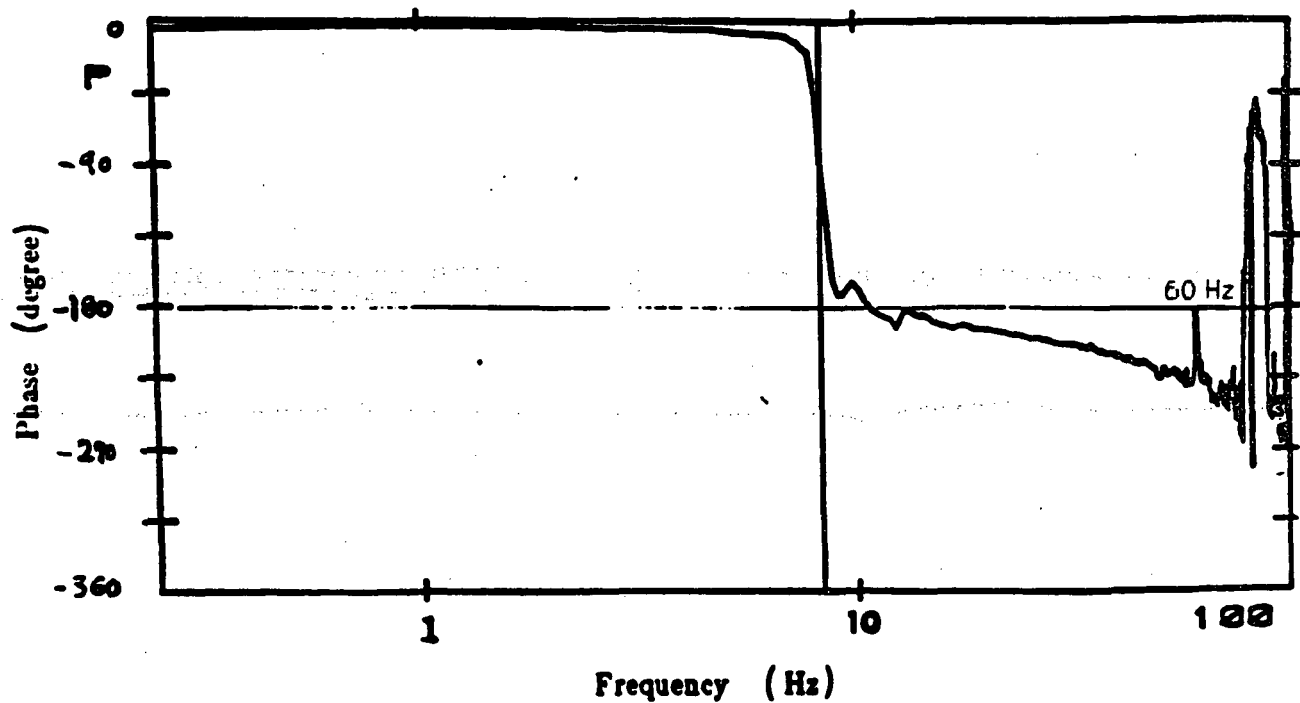
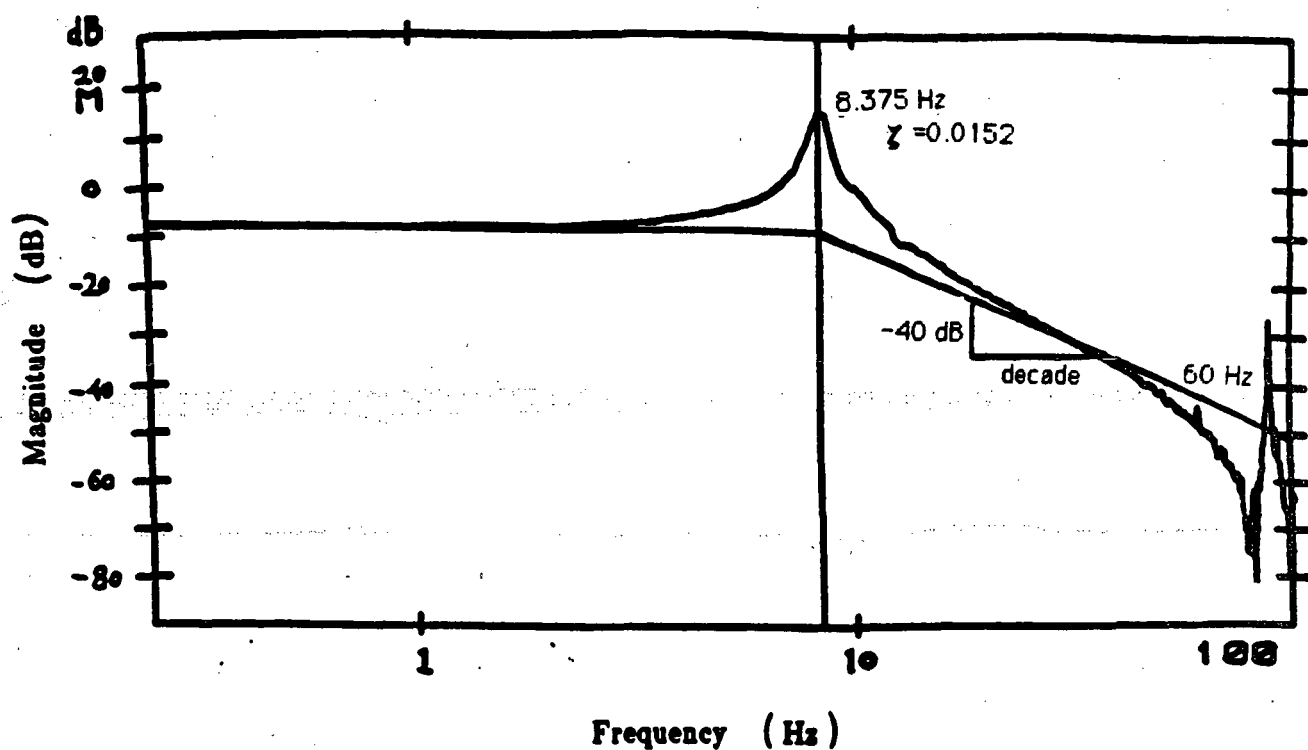


Fig. B-2 Frequency Response of h/F

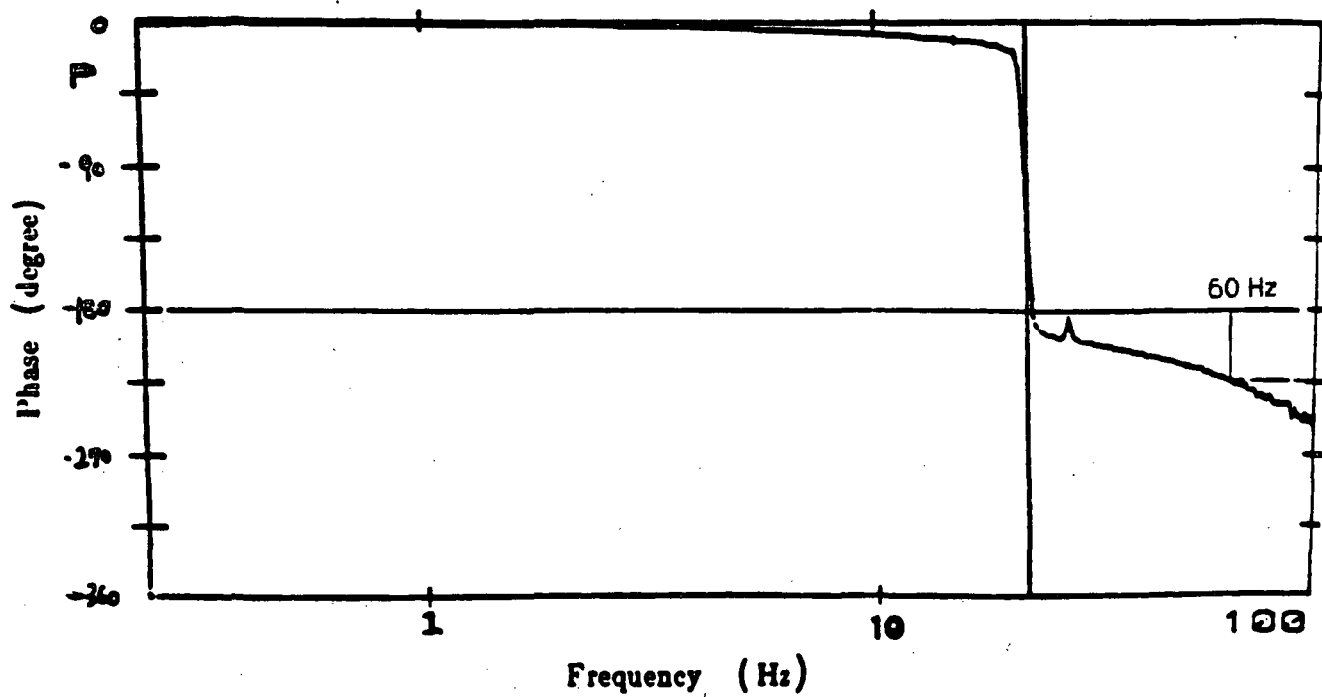
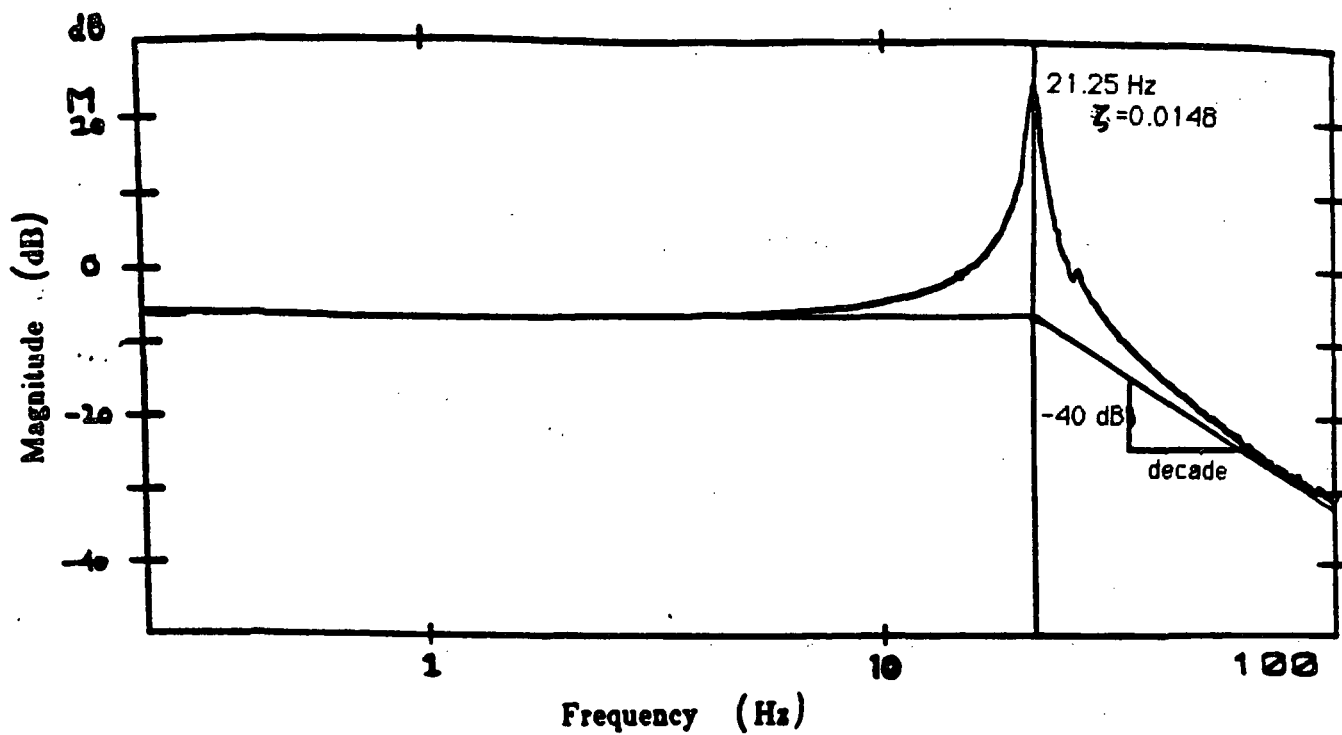


Fig. B-3 Frequency Response of α/T

B. SENSORS

B-1 Static Response

The plunge displacement sensor, LVDT, was calibrated by clamping its core in the chuck of a milling machine (Societe Genevoise, SIP, Switzerland) and fixing its case to the movable table. Table motion could be read to 2.54×10^{-3} mm (10^{-4} in.). Figure B-4 shows the voltage output of the LVDT versus the known table displacement using linear least square fit to the raw data. Its gain constant is 15.931 V/in. (627.2 V/m) which is accurate to 1% over the ± 10 mm limit on plunge displacement.

The pitch displacement sensor, resolver, was calibrated with a dividing head on a mechanical lathe (Leitz, Wetzlar, West Germany). It could be rotated accurately down to 1 arc second (2.78×10^{-4} degree). The case of the resolver was fixed while its shaft rotated with the dividing head. Figure B-5 shows the resolver voltage output versus known dividing head rotation using linear least square fit to the raw data. Its gain constant is 52.13 V/rad which is accurate to 1% over the range ± 5 degrees.

B-2 Dynamic Response

No tests for either sensor due to the difficulty to perform with available equipments. However, we anticipate no effects would occur below the 400 Hz excitation frequency.

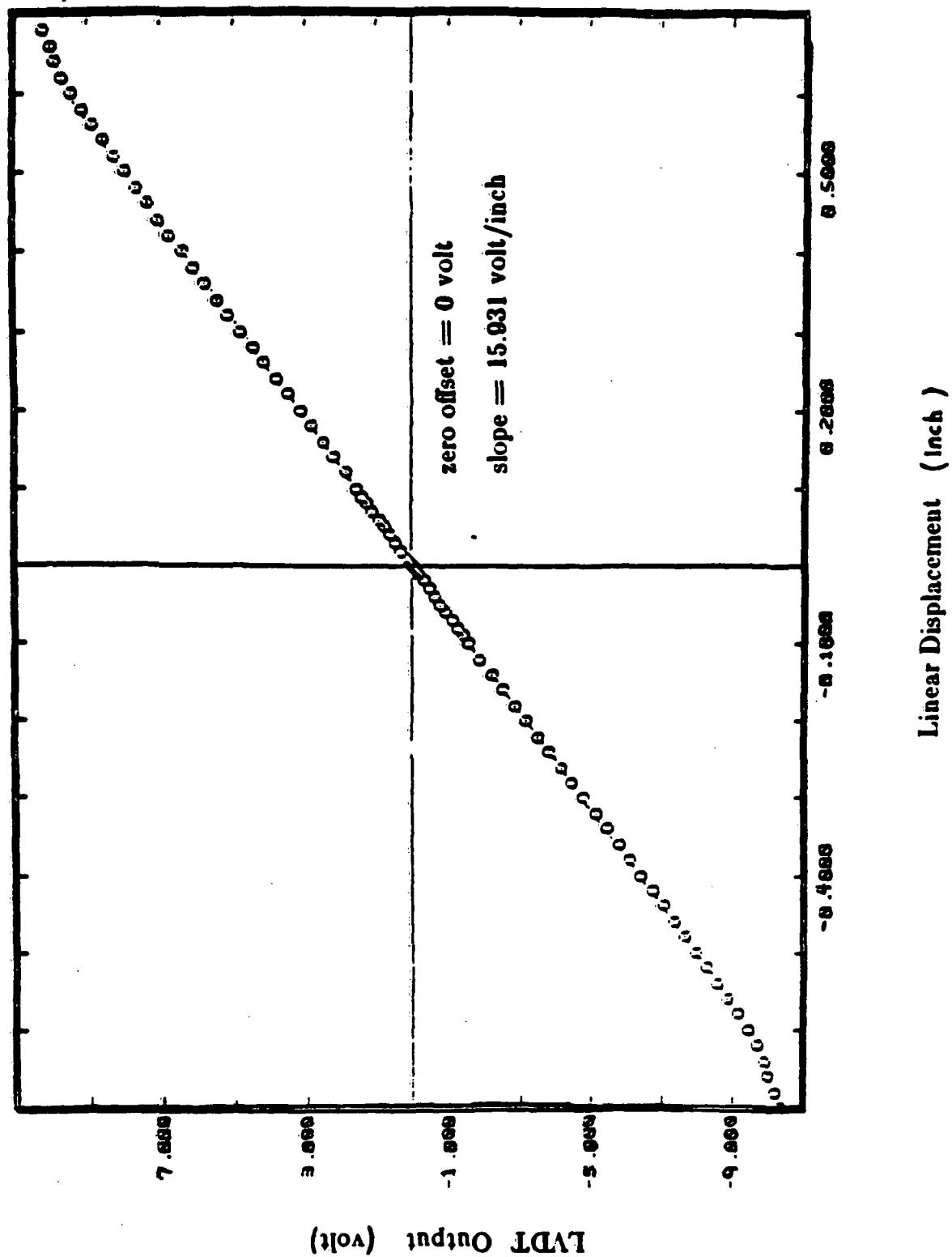


Fig. B-4 LVDT Calibration Curve

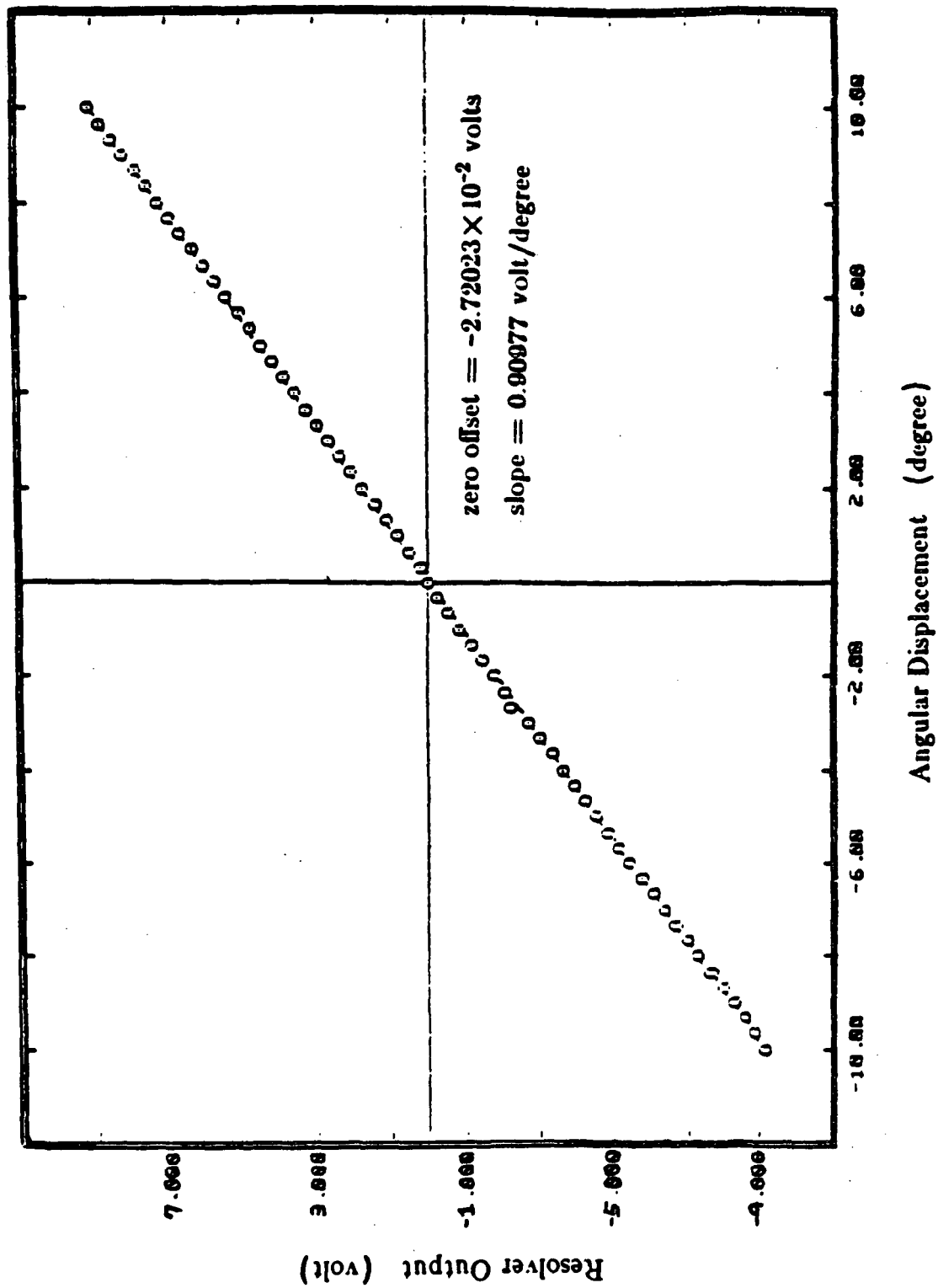


Fig. B-5 Resolver Calibration Curve

Appendix C

MEASUREMENT OF SYSTEM PARAMETERS

Brief discussions of the procedures used in determining system parameter values are presented with estimates of accuracy (worst case).

Figure C-1 shows the dimensional parameter definitions with exaggerating variations for clarity.

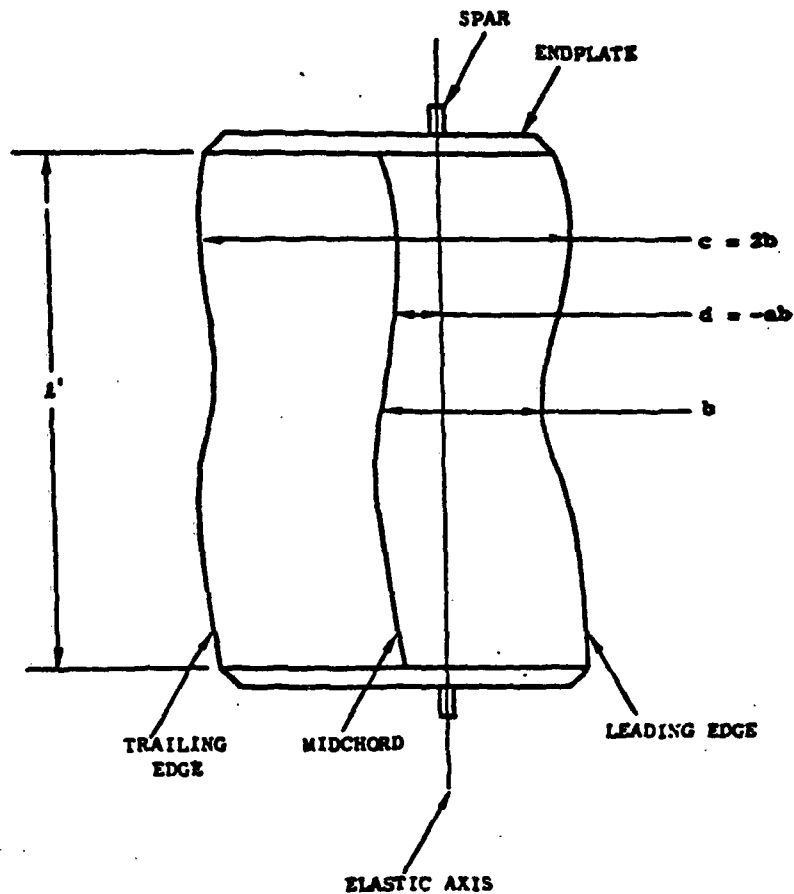


Fig. C-1 Plane View of Wing Exaggerating Dimensional Imperfections

$l = 0.4191$ m: wing span.

Directly measured with an accuracy of 2 mm (0.5%).

$c = 0.2413$ m ($b = 0.12065$ m): wing chord (semichord).

Template was numerically machined with an accuracy of 0.0254 mm (10^{-3} in.) (0.01%). Form section cut with hot wire has imperfections in the leading and trailing edge may result in chord variations of 2 mm (0.8%) along the span.

$a = -0.3$: distance in semichords the elastic axis (EA) lies after the mid-chord (MC).

Variations in a are of the same order as variations in c (0.8%).

$M_{Al} = 0.3546$ kg, 0.8461 kg/unit span (m): Al spar mass.

Directly measured using a digital scale with an accuracy of 10^{-5} kg (0.003%).

$M_2 = 2.1$ kg, 5.011 kg/unit span (m): total mass of the wing section.

Directly measured as M_{Al} . It included the mass of plexiglass endplates (0.5473 kg, 26.1% of M_2), fixing screws, accelerometer connecting wires, etc. The way the connecting wires being handled may result in 0.2 kg (9.5%) variations in M_2 .

$\omega_{h,Al} = 8.375$ Hz, 52.62 rad/sec; $\zeta_{h,Al} = 0.0152$: uncoupled plunge natural frequency and damping ratio with wing section replaced by Al spar only.

A Nicolet 660B dual-channel FFT analyzer was used to find this plunge mode frequency response with pitch mode clamped. Resonant peak can be determined accurately within its resolution range (0.125 Hz, 1.5%). Damping ratio was computed by the analyzer using the relationship $\zeta = 1 / 2Q$, where Q was the amplification factor $Q = f_0 / (f_2 - f_1)$.

$\omega_{\alpha, Al} = 21.25$ Hz, 133.5 rad/sec; $\zeta_{\alpha, Al} = 0.0148$: uncoupled pitch natural frequency and damping ratio with wing section replaced by Al spar only.

Same method as above, which is accurate to 0.125 Hz (0.6%), except the plunge mode was clamped.

$\omega_{h, wing} = 6.75$ Hz, 42.41 rad/sec; $\zeta_{h, wing} = 0.00111$: uncoupled plunge natural frequency and damping ratio with wing section installed.

Same method as above, which is accurate to 0.05 Hz (0.7%).

$\omega_{\alpha, wing} = 9.70$ Hz, 60.95 rad/sec; $\zeta_{\alpha, wing} = 0.00981$: uncoupled pitch natural frequency and damping ratio with wing section installed.

Same method as above, which is accurate to 0.05 Hz (0.7%).

$\omega_h = 6.65$ Hz, 41.78 rad/sec; $\zeta_h = 0.00448$: coupled plunge modal frequency and damping ratio with wing section installed.

Same method as above, which is accurate to 0.05 Hz (0.7%).

$\omega_{\alpha} = 10.05$ Hz, 63.15 rad/sec; $\zeta_{\alpha} = 0.00932$: coupled pitch modal frequency and damping ratio with wing section installed.

Same method as above, which is accurate to 0.05 Hz (0.7%).

$K_h = 10.38 \text{ kN/m}, 24.78 \text{ (kN/m)/unit span (m)}$: plunge spring rate.

Measuring the displacement of the plunge motion due to a known applied load (weight) yielded a direct measure of the plunge spring characteristics (Fig. C-2). Accuracy depends on the calibration of the plunge displacement sensor (1%) and the weight (0.01%), totally equals 1%.

$K_\alpha = 43.04 \text{ N-m/rad}, 102.7 \text{ (N-m/rad)/unit span (m)}$: pitch spring rate.

Measuring the angular displacement of the pitch motion due to a known applied torque (weight hung on one end of the four-bar linkage) yielded a direct measure of the pitch spring characteristics (Fig. C-3). The angle measured by the resolver was actually the twisted wing angle, however, this fact was ignored in this measurement. Accuracy depends on the pitch displacement sensor (1%).

$M_{T,Al} = 3.750 \text{ kg}, 8.947 \text{ kg/unit span (m)}$: total apparent mass with *Al* spar installed only.

The apparent mass was found from $\omega_{h,Al}$ and K_h as

$$M_{T,Al} = \frac{K_h}{\omega_{h,Al}^2}. \quad (C-1)$$

It included the mass of the *Al* spar and the suspension systems. Its accuracy depends on K_h (1%) and $\omega_{h,Al}$ (1.5%), and is about $1 + 1.5 * 2 = 4\%$.

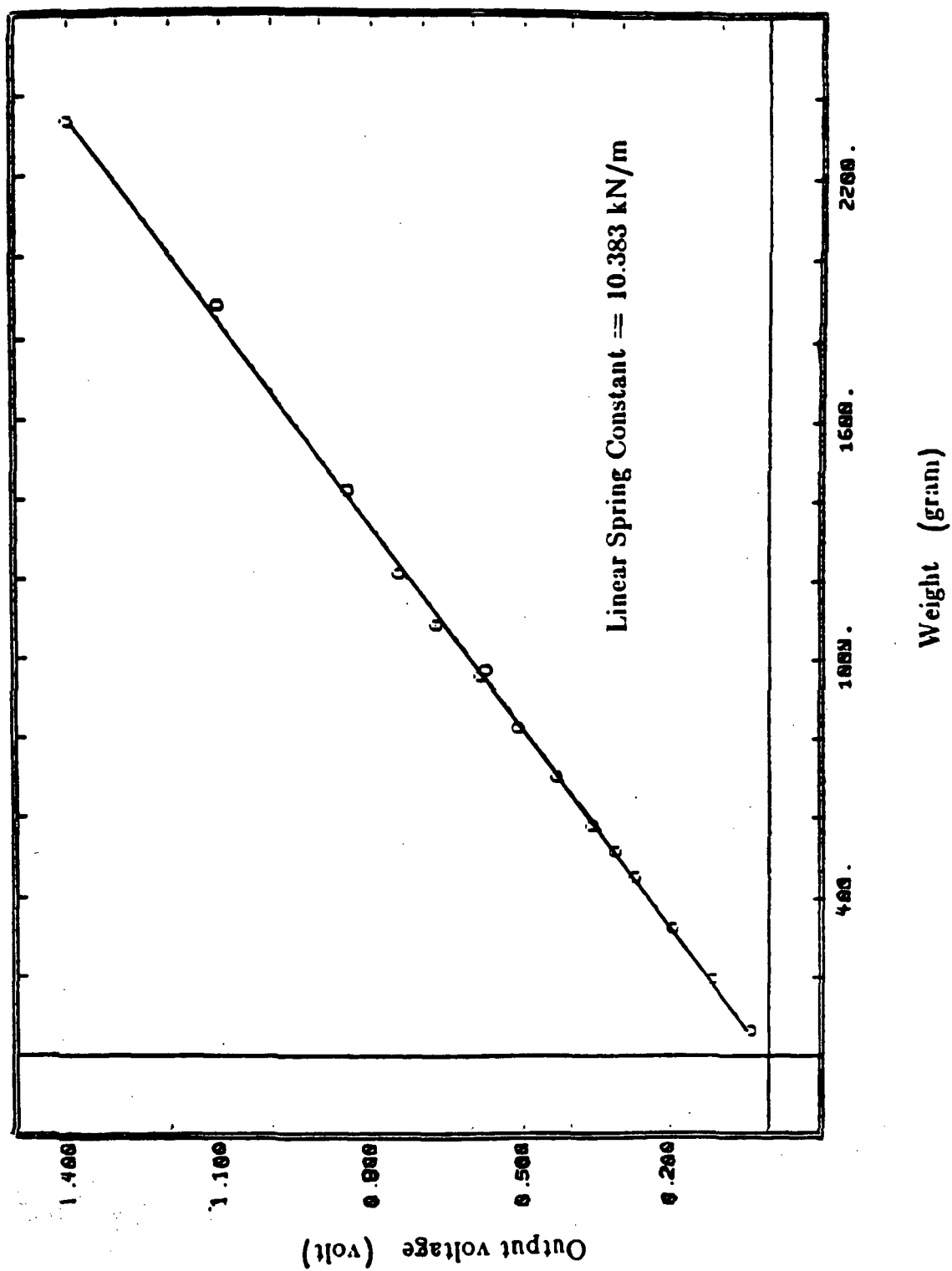


Fig. C-2 Linear Spring Constant Calibration Curve

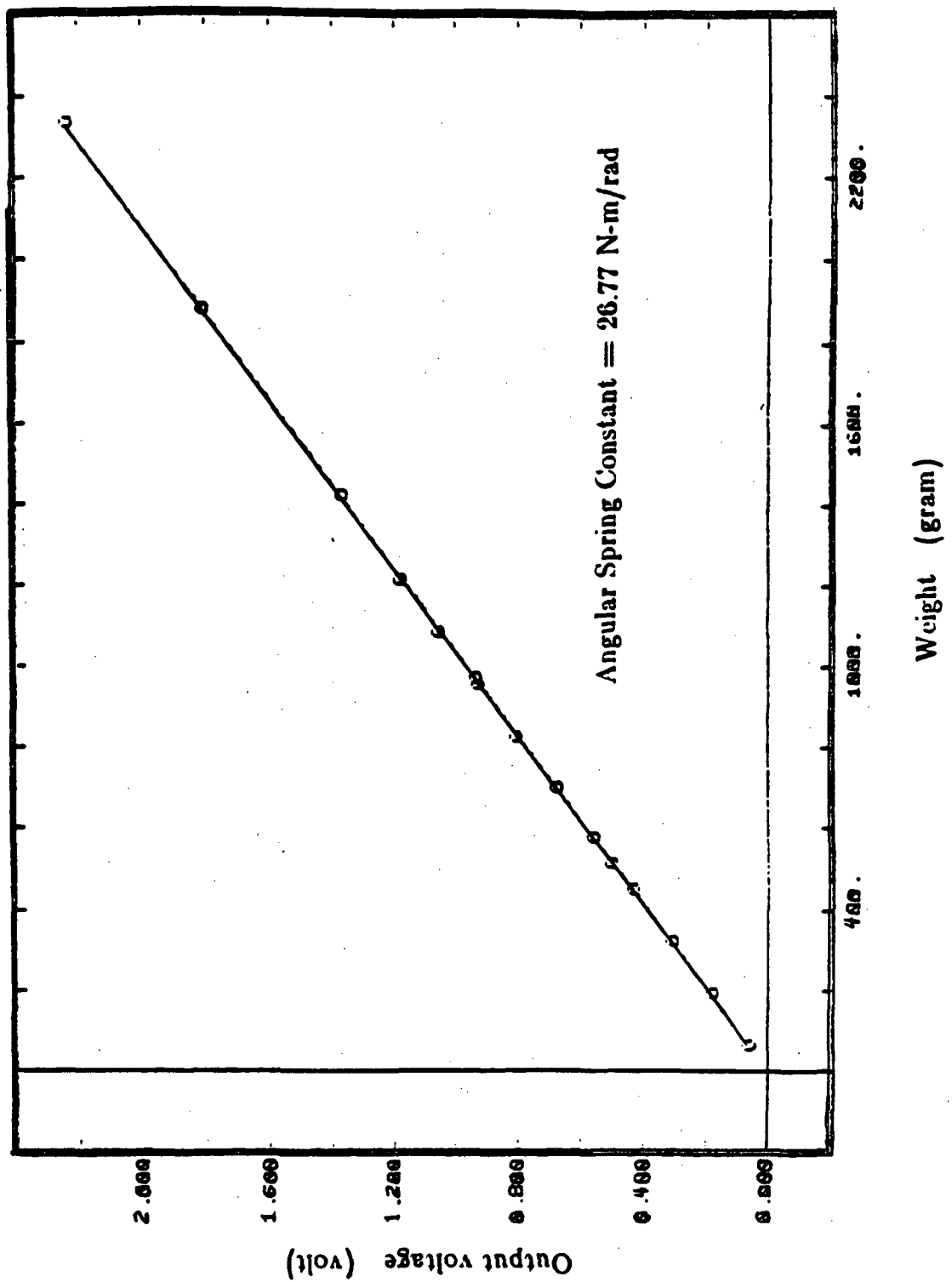


Fig. C-3 Angular Spring Constant Calibration Curve

$M_1 = 3.395 \text{ kg}, 8.100 \text{ kg/unit span (m)}$: total apparent mass of the suspension systems.

$$M_1 = M_{T,Al} - M_{Al}, \quad (C-2)$$

which is accurate to 4%.

$I_{\alpha_1} = 1.502 \cdot 10^{-3} \text{ kg-m}^2, 3.584 \cdot 10^{-3} \text{ kg-m}^2/\text{unit span (m)}$: apparent moment of inertia of the pitch suspension system about the EA.

This apparent moment of inertia about the EA was found from K_α and $\omega_{\alpha,Al}$ as

$$I_{\alpha_1} = \frac{K_\alpha}{\omega_{\alpha,Al}^2}. \quad (C-3)$$

Since the calculated moment of inertia of the Al spar was only 1% of I_{α_1} , it could be ignored. I_{α_1} is accurate to $1 + 0.6 \cdot 2 = 2.2\%$.

$I_\alpha = I_{\alpha_T} = 1.151 \cdot 10^{-2} \text{ kg-m}^2, 2.746 \cdot 10^{-2} \text{ kg-m}^2/\text{unit span (m)}$: total apparent moment of inertia with wing section installed about the EA.

$$I_{\alpha_T} = \frac{K_\alpha}{\omega_{\alpha,wing}^2}, \quad (C-4)$$

which is accurate to $1 + 0.7 \cdot 2 = 2.4\%$.

$I_{\alpha_2} = 1.001 \cdot 10^{-2} \text{ kg-m}^2, 2.388 \cdot 10^{-2} \text{ kg-m}^2/\text{unit span (m)}$: total apparent moment of inertia of the wing section and endplates about the EA.

$$I_{\alpha_2} = I_{\alpha_T} - I_{\alpha_1}, \quad (C-5)$$

which is accurate to 2.4%.

$M_T = 5.7$ kg, 13.60 kg/unit span (m): total apparent mass of the wing section and the suspension systems.

$$M_T = M_1 + M_2, \quad (C-6)$$

which is accurate to 7.2%.

$\bar{r}_\alpha^2 = 0.3767$: squared radius of gyration in semichords squared about the EA.

$$\bar{r}_\alpha^2 = \frac{I_{\alpha_T}}{M_2 b^2}, \quad (C-7)$$

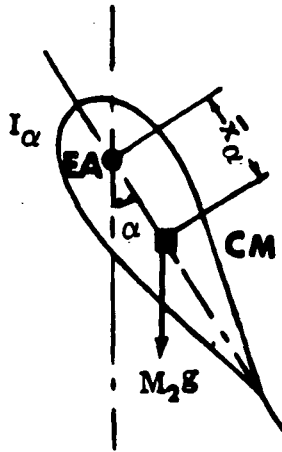
which is accurate to $2.4 + 7.2 + 0.8 * 2 = 11.2\%$.

$\bar{x}_\alpha = 0.19$: distance in semichords the center of mass (CM) lies after the EA.

The measurement of \bar{x}_α is based on its physical definition shown in Fig. C-4. Oscillation frequency was measured with a stop watch accurate to 0.1 sec (0.3%) for 30 cycles (27.5 sec).

$$\bar{x}_\alpha = \frac{I_\alpha \omega^2}{M_2 g b}, \quad (C-8)$$

which is accurate to $2.4 + 0.3 * 2 + 7.2 + 0.8 = 11\%$.



$$\begin{aligned}
 I_{\alpha} \ddot{\alpha} + M_2 g \bar{x}_{\alpha} \cdot \alpha &= 0, \\
 \omega^2 I_{\alpha} &= M_2 g \bar{x}_{\alpha}, \\
 \bar{x}_{\alpha} &= \frac{\omega^2 I_{\alpha}}{M_2 g}.
 \end{aligned}$$

Fig. C-4 Calibration of \bar{x}_{α}

$\bar{l} = 1.684$: length of the four-bar linkage in semichords.

Directly measured with an accuracy of 2 mm ($1 + 0.8 = 1.8\%$).

$K_2 = 0.3684$: mass ratio.

$$K_2 = \frac{M_2}{M_T}. \quad (\text{C-9})$$

$K = 0.9847$: moment of inertia ratio.

$$K = \frac{\bar{r}_c^2}{\bar{r}_{\alpha}^2} = 1 - \frac{K_2 \bar{x}_{\alpha}^2}{\bar{r}_{\alpha}^2}. \quad (\text{C-10})$$

$K_c = 421.1 \text{ N-m/rad}$: spar coupling spring rate.

Computed value for 3 DOF (degree of freedom) modeling.

$K_F = 5.295 \text{ N/V}$: linear motor force constant.

$K_T = 0.2232 \text{ N-m/V}$: torque motor moment constant.

$\omega_{\alpha_1} = 91.50 \text{ Hz}$, 574.9 rad/sec ; $\zeta_{\alpha_1} = 0.0443$: differential pitch modal frequency and damping ratio.

Directly measured by FFT analyzer which is accurate to 0.25 Hz (0.3%).

$\omega_{c_{21}} = 6710 \text{ Hz}$, $42,166 \text{ rad/sec}$: coupling frequency from wing to four-bar linkage.

$$\omega_{c_{21}} = \sqrt{\frac{K_c}{I_{\alpha}}}. \quad (\text{C-11})$$

$\omega_{c_{12}} = 44,629 \text{ Hz}$, $280,414 \text{ rad/sec}$: coupling frequency from four-bar linkage to wing.

$$\omega_{c_{12}} = \sqrt{\frac{K_c}{I_{\alpha_1}}}. \quad (\text{C-12})$$

$\mu = 246.0$: mass ratio.

$$\mu = \frac{M_T/l}{\pi \rho b^2}. \quad (\text{C-13})$$

The density of air in the tunnel ρ is nominally 1.219 kg/m^3 , which is known within 1%. μ is thus accurate to $7.2 + 0.5 + 1 + 0.8 \times 2 = 10.3\%$.

$S_\alpha = 0.04814 \text{ kg-m}$, $0.1149 \text{ kg-m/unit span (m)}$: dynamic coupling coefficient.

$$S_\alpha = M_2 x_\alpha = M_2 \bar{x}_\alpha b, \quad (\text{C-14})$$

which is accurate to $3 + 0.5 = 3.5\%$.

Appendix D

TABLE OF GRADIENTS

$$1. \quad \frac{\partial}{\partial \underline{X}} \text{tr}(\underline{X}) = \underline{1}$$

$$2. \quad \frac{\partial}{\partial \underline{X}} \text{tr}(\underline{A} \underline{X}) = \underline{A}'$$

$$3. \quad \frac{\partial}{\partial \underline{X}} \text{tr}(\underline{A} \underline{X}') = \underline{A}$$

$$4. \quad \frac{\partial}{\partial \underline{X}} \text{tr}(\underline{A} \underline{X} \underline{B}) = \underline{A}' \underline{B}'$$

$$5. \quad \frac{\partial}{\partial \underline{X}} \text{tr}(\underline{A} \underline{X}' \underline{B}) = \underline{B} \underline{A}$$

$$6. \quad \frac{\partial}{\partial \underline{X}'} \text{tr}(\underline{A} \underline{X}) = \underline{A}$$

$$7. \quad \frac{\partial}{\partial \underline{X}'} \text{tr}(\underline{A} \underline{X}') = \underline{A}'$$

$$8. \quad \frac{\partial}{\partial \underline{X}'} \text{tr}(\underline{A} \underline{X} \underline{B}) = \underline{B} \underline{A}$$

$$9. \quad \frac{\partial}{\partial \underline{X}'} \text{tr}(\underline{A} \underline{X}' \underline{B}) = \underline{A}' \underline{B}'$$

$$10. \quad \frac{\partial}{\partial \underline{X}} \text{tr}(\underline{X} \underline{X}) = 2 \underline{X}'$$

$$11. \quad \frac{\partial}{\partial \underline{X}} \text{tr}(\underline{X} \underline{X}') = 2 \underline{X}$$

TABLE OF GRADIENTS (cont)

$$12. \quad \frac{\partial}{\partial \underline{X}} \text{tr}[\underline{X}^n] = n(\underline{X}^{n-1})'$$

$$13. \quad \frac{\partial}{\partial \underline{X}} \text{tr}[\underline{A} \underline{X}^n] = \left(\sum_{i=0}^{n-1} \underline{X}^i \underline{A} \underline{X}^{n-1-i} \right)'$$

$$14. \quad \frac{\partial}{\partial \underline{X}} \text{tr}[\underline{A} \underline{X} \underline{B} \underline{X}] = \underline{A}' \underline{X}' \underline{B}' + \underline{B}' \underline{X}' \underline{A}'$$

$$15. \quad \frac{\partial}{\partial \underline{X}} \text{tr}[\underline{A} \underline{X} \underline{B} \underline{X}'] = \underline{A}' \underline{X}' \underline{B}' + \underline{A} \underline{X} \underline{B}$$

$$16. \quad \frac{\partial}{\partial \underline{X}} \text{tr}[e^{\underline{X}}] = e^{\underline{X}}$$

$$17. \quad \frac{\partial}{\partial \underline{X}} \text{tr}[\underline{X}^{-1}] = -(\underline{X}^{-1} \underline{X}^{-1})' = -(\underline{X}^{-2})'$$

$$18. \quad \frac{\partial}{\partial \underline{X}} \text{tr}[\underline{A} \underline{X}^{-1} \underline{B}] = -(\underline{X}^{-1} \underline{B} \underline{A} \underline{X}^{-1})'$$

$$19. \quad \frac{\partial}{\partial \underline{X}} \det[\underline{X}] = (\det[\underline{X}]) (\underline{X}^{-1})'$$

$$20. \quad \frac{\partial}{\partial \underline{X}} \log \det[\underline{X}] = (\underline{X}^{-1})'$$

$$21. \quad \frac{\partial}{\partial \underline{X}} \det[\underline{A} \underline{X} \underline{B}] = (\det[\underline{A} \underline{X} \underline{B}]) (\underline{X}^{-1})'$$

$$22. \quad \frac{\partial}{\partial \underline{X}} \det[\underline{X}'] = \frac{\partial}{\partial \underline{X}} \det[\underline{X}] = (\det[\underline{X}]) (\underline{X}^{-1})'$$

$$23. \quad \frac{\partial}{\partial \underline{X}} \det[\underline{X}^n] = n(\det[\underline{X}])^n (\underline{X}^{-1})'$$

References

- [1] Wie, B., "On the Modeling and Control of Flexible Space Structures," Ph.D. Dissertation, Dept. of Aeronautics and Astronautics, Stanford University, Stanford, CA 94305, SUDAAR 525, Jun. 1981.
- [2] Martin, G.D., "On the Control of Flexible Mechanical Systems," Dept. of Aeronautics and Astronautics, Stanford University, Stanford, CA 94305, SUDAAR 511, May. 1978.
- [3] Mahesh, J.K., C.R. Stone, W.L. Garrard, and H.J. Dunn, "Control Law Synthesis for Flutter Suppression Using Linear Quadratic Gaussian Theory," Journal of Guidance, Control, and Dynamics, Vol. 4, No. 4, Jun.-Aug. 1981, pp. 415-422.
- [4] Walker, R., and N. Gupta, "Real-Time Flutter Analysis," NASA Contractor Report 170412, Mar. 1984.
- [5] Karpel, M., "Design for Active and Passive Flutter Suppression and Gust Alleviation," Aug. 1980.
- [6] Hwang, C.S., and D.F. Kesler, "Aircraft Active Controls - New Era in Design," AIAA Journal, Vol. 21, Jun. 1983, pp. 70-85.
- [7] Kailath, T., Linear Systems, Prentice-Hall, Inc., Englewood Cliffs, New York, 1980.
- [8] Juang, J.N., and G. Rodriguez, "Formulations and Applications of Large Structure Actuator and Sensor Placements," Proceedings of the 2nd VPI & SU/AIAA Symposium, Blacksburg, VA, Jun. 1979, pp. 247-262.

- [9] Viswanathan, C.N., R.W. Longman, and P.W. Likins, "A Definition of the Degree of Controllability - A Criterion for Actuator Placement," Proceedings of the 2nd VPI & SU/AIAA Symposium, Blacksburg, VA, Jun. 1979, pp. 369-384.
- [10] Hughes, P.C., and R.E. Skelton, "Controllability and Observability for Flexible Spacecraft," Proceedings of the 2nd VPI & SU/AIAA Symposium, Blacksburg, VA, Jun. 1979, pp. 385-408.
- [11] Kammer, D.C., and J.R. Sesak "Actuator Number versus Parameter Sensitivity in Flexible Spacecraft Control," Proceedings of the 2nd VPI & SU/AIAA Symposium, Blacksburg, VA, Jun. 1979, pp. 421-441.
- [12] Vander Velde, W.E., and C.R. Carignan, "A Dynamic Measure of Controllability and Observability for the Placement of Actuators and Sensors on Large Space Structures," MIT Space Systems Lab, MIT, Cambridge, Mass., Rept. 2-82, Jan. 1982.
- [13] Vander Velde, W.E., and C.R. Carignan, "Number and Placement of Control System Components Considering Possible Failures," Journal of Guidance, Control, and Dynamics, Vol. 7, No. 6, Nov.-Dec. 1984, pp. 703-709.
- [14] Carignan, C.R., and W.E. Vander Velde, "Number and Placement of Control System Components Considering Possible Failures," MIT Space Systems Lab, MIT, Cambridge, Mass., Rept. 5-82, Mar. 1982.
- [15] Kwakernaak, H., and R. Sivan, Linear Optimal Control Systems, Wiley-Interscience, John Wiley & Sons, Inc., New York, 1972.
- [16] Bryson, A.E., Jr., and Y.C. Ho, Applied Optimal Control, John Wiley & Sons, New York, 1975.
- [17] Fung, Y.C., An Introduction to the Theory of Aeroelasticity, Dover Publications, Inc., New York, 1969.

- [18] Bisplinghoff, R.L., and H. Ashley, Principle of Aeroelasticity, Dover Publications, Inc., New York, 1962.
- [19] Theodorsen, T., "General Theory of Aerodynamic Instability and the Mechanism of Flutter," NACA Report 496, 1935.
- [20] Timman, R., "The Aerodynamic Forces on an Oscillating Aerofoil Between Two Parallel Walls," Applied Science Research, Vol. A3, No. 1, 1951, pp. 31-57.
- [21] Edwards, J.W., "Unsteady Aerodynamic Modeling and Active Aeroelastic Control," Ph.D. Dissertation, Dept. of Aeronautics and Astronautics, Stanford University, Stanford, CA 94305, SUDAAR 504, Feb. 1977.
- [22] Edwards, J.W., J.V. Breakwell, and A.E. Bryson, Jr., "Active Flutter Control Using Generalized Unsteady Aerodynamic Theory," Journal of Guidance, Control, and Dynamics, Vol. 1, No. 1, Jan.-Feb. 1978, pp. 32-40.
- [23] Von Kármán, and W.R. Sears, "Airfoil Theory for Non-Uniform Motion," Journal of Aerospace Science, Aug. 1938, pp. 379-390. pp. 32-40.
- [24] Sears, W.R., "Operational Methods in the Theory of Airfoils in Non-Uniform Motion," Journal of the Franklin Institute, Vol. 230, No. 1, Jul. 1940, pp. 95-111.
- [25] Rock, S.M., "Transient Motion of an Airfoil: An Experimental Investigation in a Small, Subsonic Wind Tunnel," Ph.D. Dissertation, Dept. of Aeronautics and Astronautics, Stanford University, Stanford, CA 94305, SUDAAR 513, May 1978.
- [26] Stoltz, P.M., "Unsteady Aeroelastic Modeling and Trailing-Edge Flap Control of an Experimental Wing in a Two-Dimensional Wind Tunnel," Ph.D. Dissertation, Dept. of Aeronautics and Astronautics, Stanford University, Stanford, CA 94305, SUDAAR 527, Jun. 1981.

- [27] Hall, W.E., and A.E. Bryson, Jr., "Optimal Control and Filter Synthesis by Eigenvector Decomposition," Ph.D. Dissertation, Dept. of Aeronautics and Astronautics, Stanford University, Stanford, CA 94305, SUDAAR 436, Nov. 1971.
- [28] Katz, P., and J.D. Powell, "Selection of Sampling Rate for Digital Control of Aircrafts," Ph.D. Dissertation, Dept. of Aeronautics and Astronautics, Stanford University, Stanford, CA 94305, SUDAAR 486, Sep. 1974.
- [29] Greenwood, D.T., Principles of Dynamics, Prentice-Hall, Inc., Englewood Cliffs, New Jersey, 1965.
- [30] Chiang, W.W., "Rapid, Precise End-Point Control of a Wrist Carried by a Very Flexible Manipulator,"
- [31] Sliwa, S.M., "An On-Line Equivalent System Identification Scheme for Adaptive Control," NASA Technical Memorandum 85737, Jan. 1984.
- [32] Stepner, D.E., and R.K. Mehra, "Maximum Likelihood Identification and Optimal Input Design for Identifying Aircraft Stability and Control Derivatives," NASA Contractor Report 2200, Mar. 1973.
- [33] Mishne, D., and A.E. Bryson, Jr., "On-Line Parameter Estimation Using a High Sensitivity Estimator," Dept. of Aeronautics and Astronautics, Stanford University, Stanford, CA 94305, SUDAAR 507, Nov. 1977.
- [34] Thomson, W.T., Vibration Theory and Applications, Prentice-Hall, Inc., Englewood Cliffs, New Jersey, 1965.
- [35] Cannon, R.H., Jr., Dynamics of Physical Systems, McGraw-Hill Book Company, New York, 1967.
- [36] Kalman, R.E., "A New Approach to Linear Filtering and Prediction Problems," Journal of Basic Engineering, Mar. 1960, pp. 35-46.

- [37] Schmidt, S.F., "The Kalman Filter: Its Recognition and Development for Aerospace Applications," *Journal of Guidance, Control, and Dynamics*, Vol. 4, No. 1, Jan.-Feb. 1981, pp. 4-7.
- [38] Gelb, A. (editor), et al., Applied Optimal Estimation, The M.I.T. Press, MIT, Cambridge, Mass., 1974.
- [39] Fitzgerald, R.J., "Divergence of the Kalman Filter," *IEEE Transactions on Automatic Control*, Vol. AC-16, No. 6, Dec. 1971, pp. 736-747.
- [40] Nishimura, T., "Modeling Errors in Kalman Filters," Ch. 4, of Theory and Applications on Automatic Control, AGARDograph 139, 1970.
- [41] Bryson, A.E., Jr., "Kalman Filter Divergence and Aircraft Motion Estimators," Vol. 1, No. 1, Jan.-Feb. 1978, pp. 71-79.
- [42] Bossi, J.A., and A.E. Bryson, Jr., "Estimation of Wind Shear and Thrust Loss during STOL Aircraft Landing Approach," Ph.D. Dissertation, Dept. of Aeronautics and Astronautics, Stanford University, Stanford, CA 94305, SUDAAR 519, Jan. 1980.
- [43] Kaminski, P.G., A.E. Bryson, Jr., and S.F. Schmidt, "Discrete Square Root Filtering: A Survey of Current Techniques," *IEEE Transactions on Automatic Control*, Vol. AC-16, No. 6, Dec. 1971, pp. 727-736.
- [44] Bellantoni, J.F., and K.W. Dodge, "A Square Root Formulation of the Kalman-Schmidt Filter," *AIAA Journal*, Vol. 5, Jul. 1967, pp. 1309-1314.
- [45] DeBra, D.B., Final Report on "The Applicability of Integrated Circuit Technology to General Aviation Orientation Estimation," Dept. of Aeronautics and Astronautics, Stanford University, Stanford, CA 94305, Sep. 1976, pp. 6-7.
- [46] Meirovitch, L., Analytical Methods in Vibrations, the MacMillan Company, London, 1967.

- [47] Rosenthal, D.E., "Experiments in Control of Flexible Structures with Uncertain Parameters," Ph.D. Dissertation, Dept. of Aeronautics and Astronautics, Stanford University, Stanford, CA 94305, SUDAAR 542, Mar. 1984.
- [48] Papoulis, A., Probability, Random Variable, and Stochastic Processes, McGraw-Hill Book Company, New York, 1965.
- [49] Athans, M., "Gradient Matrices and Matrix Calculations," Lincoln Laboratory, MIT, Lexington, Mass., Nov. 1965.
- [50] DeBra, D.B., and A.E. Bryson, Jr., "Minimum Cost Autopilots for Light Aircraft," VI IFAC Symposium on Automatic Control in Space, Aug. 1974, Tsakhkadzor, Armenian SSR, USSR.
- [51] Sanz Fernandez de Cordova, S., "Orientation and Three-Dimensional Mass Center Estimation in a Rotating Drag-Free Satellite," Ph.D. Dissertation, Dept. of Aeronautics and Astronautics, Stanford University, Stanford, CA 94305, SUDAAR 496, Aug. 1975.
- [52] DeBra, D.B., "Estimation in Satellite Control," Proceedings of the 9th International Symposium on Space Technology and Science, Tokyo, 1971.
- [53] Franklin, G.F., and J.D. Powell, Digital Control of Dynamic Systems, Addison-Wesley Publishing Company, Reading, Mass., Jun. 1981.
- [54] Cadzow, J.A., H.R. Martens, Discrete-Time and Computer Control Systems, Prentice-Hall, Inc., Englewood Cliffs, New Jersey, 1970.
- [55] Ogata, K., State Space Analysis of Control Systems, Prentice-Hall, Inc., Englewood Cliffs, New York, 1967.
- [56] Digumarthi, R.V., S.P. Koutsoyannis, and K. Karamcheti, "Some Observations of Surface Pressures and the Near Wake of a Blunt Trailing Edge Airfoil," Joint Institute for Aeronautics and Acoustics TR-39, Stanford University, Jun. 1981.

- [57] Abbott, I.H., and A.E. Von Doenhoff, Theory of Wing Sections, Dover Publications, Inc., New York, 1949.
- [58] Timoshenko, S., and D.H. Young, Elements of Strength of Materials, 4th edition, D. Van Nostrand Company, Inc., Princeton, New Jersey, 1962.
- [59] Chen, C.T., Introduction to Linear System Theory, Holt, Rinehart and Winston, Inc., New York, 1984.
- [60] Ogata, K., Modern Control Engineering, Prentice-Hall, Inc., Englewood Cliffs, New York, 1970.
- [61] Friedlander, B., "Lattice Filters for Adaptive Processing," Proceedings of the IEEE, Vol. 70, No. 8, Aug. 1982, pp. 829-863.
- [62] Pope, A., and J.J. Harper, Low-Speed Wind Tunnel Testing, John Wiley & Sons, Inc., New York, 1966.
- [63] Karamcheti, K., Principles of Ideal-Fluid Aerodynamics, John Wiley & Sons, Inc., New York, 1966.
- [64] Walker, R., "Computing the Jordan Form for Control of Dynamic Systems," Ph.D. Dissertation, Dept. of Aeronautics and Astronautics, Stanford University, Stanford, CA 94305, SUDAAR 528, Mar. 1981.
- [65] Stapleford, R.L., D.T. McRuer, L.G. Hofmann, and G.L. Teper, "A Practical Optimization Design Procedure for Stability Augmentation Systems," Air Force Flight Dynamics Lab. Technical Report 70-11, Oct. 1970.